

Energy Research and Development Division  
**FINAL PROJECT REPORT**

# **Aerosol Impacts on the Hydrology and Hydropower Generation in California**

**California Energy Commission**

Gavin Newsom, Governor

March 2019 | CEC-500-2019-024



**PREPARED BY:**

**Primary Author(s):**

Nanpeng Yu  
Farzana Kabir  
Longtao Wu  
Yu Gu  
Jonathan H. Jiang  
Hui Su  
Weixin Yao  
Balakrishna Sastry

**Contract Number:** EPC-14-064

**PREPARED FOR:**

California Energy Commission

Guido Franco  
**Project Manager**

Rizaldo Aldas  
**Office Manager**  
**ENERGY GENERATION RESEARCH OFFICE**

Laurie ten Hope  
**Deputy Director**  
**ENERGY RESEARCH AND DEVELOPMENTS DIVISION**

Drew Bohan  
**Executive Director**

**DISCLAIMER**

This report was prepared as the result of work sponsored by the California Energy Commission. It does not necessarily represent the views of the Energy Commission, its employees, or the State of California. The Energy Commission, the State of California, its employees, contractors, and subcontractors make no warrant, express or implied, and assume no legal liability for the information in this report; nor does any party represent that the uses of this information will not infringe upon privately owned rights. This report has not been approved or disapproved by the California Energy Commission nor has the California Energy Commission passed upon the accuracy or adequacy of the information in this report.

## PREFACE

The California Energy Commission's Energy Research and Development Division supports energy research and development programs to spur innovation in energy efficiency, renewable energy and advanced clean generation, energy-related environmental protection, energy transmission and distribution and transportation.

In 2012, the Electric Program Investment Charge (EPIC) was established by the California Public Utilities Commission to fund public investments in research to create and advance new energy solutions, foster regional innovation and bring ideas from the lab to the marketplace. The California Energy Commission and the state's three largest investor-owned utilities—Pacific Gas and Electric Company, San Diego Gas & Electric Company and Southern California Edison Company—were selected to administer the EPIC funds and advance novel technologies, tools, and strategies that provide benefits to their electric ratepayers.

The Energy Commission is committed to ensuring public participation in its research and development programs that promote greater reliability, lower costs, and increase safety for the California electric ratepayer and include:

- Providing societal benefits.
- Reducing greenhouse gas emission in the electricity sector at the lowest possible cost.
- Supporting California's loading order to meet energy needs first with energy efficiency and demand response, next with renewable energy (distributed generation and utility scale), and finally with clean, conventional electricity supply.
- Supporting low-emission vehicles and transportation.
- Providing economic development.
- Using ratepayer funds efficiently.

*Aerosol Impacts on the Hydrology and Hydropower Generation in California* is the [final](#) report for Contract Number EPC-14-064 conducted by the University of California, Riverside. The information from this project contributes to the Energy Research and Development Division's EPIC Program.

For more information about the Energy Research and Development Division, please visit the Energy Commission's website at [www.energy.ca.gov/research/](http://www.energy.ca.gov/research/) or contact the Energy Commission at 916-327-1551.

## ABSTRACT

Recent studies have shown that aerosols can substantially influence temperature, precipitation, and snowpack in California through their direct, indirect, and deposition effects. The impact of aerosols on these meteorological variables can influence hydropower reservoir inflow, which can in turn impact hydroelectricity generation in California. This project developed a fully coupled aerosol-meteorology-snowpack forecasting model by integrating a weather research and forecasting model, a statistical inflow forecast model using dynamic regression method, and a hydroelectric power plant optimization model (Vista) to quantify the impact of aerosols on hydropower generation in California.

Aerosols warm the California mountaintops through aerosol-snow interaction by local dust, cool the lower elevation areas through aerosol-radiation interaction, and reduce precipitation and snowpack in California. The researchers developed a comprehensive framework to quantify the impact of aerosols on inflow into the Big Creek Hydroelectric System. The developed framework seamlessly integrates the Weather Research and Forecasting Model with chemistry (WRF-Chem) and a statistical inflow forecast model. The simulation results show that the presence of aerosols results in a significant reduction of annual reservoir inflow (flow of water) by 4-14 percent.

The research team calculated the impact of aerosols on hydropower generation and revenue by feeding the inflow forecasts of the lakes to the Big Creek Hydroelectric System both with and without considering the impact of aerosols into the Vista Decision Support System. From the simulation results, researchers found that aerosols reduce inflows into the reservoirs of Big Creek hydroelectric system by 1-10 percent. The presence of aerosols causes \$2.8 million loss in revenue in a water year for Southern California Edison, providing more justification for stricter environmental regulations to reduce anthropogenic aerosol emissions.

**Keywords:** WRF-Chem, Aerosol, Hydropower, Water-Energy Nexus, Inflow simulation

Please use the following citation for this report:

Yu, Nanpeng, Farzana Kabir, Longtao Wu, Yu Gu, Jonathan H. Jiang, Hui Su, Weixin Yao, Balakrishna Sastry. University of California, Riverside, 2019. *Aerosol Impacts on the Hydrology and Hydropower Generation in California*. California Energy Commission. Publication Number: CEC-500-2019-024.

# TABLE OF CONTENTS

	Page
<b>PREFACE</b> .....	<b>i</b>
<b>ABSTRACT</b> .....	<b>ii</b>
<b>TABLE OF CONTENTS</b> .....	<b>iii</b>
<b>LIST OF FIGURES</b> .....	<b>v</b>
<b>LIST OF TABLES</b> .....	<b>vii</b>
<b>EXECUTIVE SUMMARY</b> .....	<b>1</b>
Introduction.....	1
Project Purpose .....	1
Project Approach.....	1
Project Results.....	1
Knowledge Transfer.....	2
Benefits for California.....	2
<b>CHAPTER 1: Aerosol Seasonal Variability and Impacts on Seasonal Precipitation and Snowpack</b> 4	
1.1 Introduction.....	4
1.2 Literature Review .....	6
1.3 Technical Methods.....	7
1.3.1 Observations.....	7
1.3.2 Model Description.....	9
1.3.3 Experiment Design.....	11
1.4 Model Evaluation.....	13
1.4.1 Sensitivity to Horizontal Resolution.....	14
1.4.2 Sensitivity to Dust Scheme .....	22
1.4.3 The Role of Meteorology .....	26
1.5 Impacts of Aerosols on Precipitation and Snowpack in California.....	30
1.5.1 Validation of Model Results .....	30
1.5.2 Aerosol Effects on Precipitation and Snowpack.....	33
1.5.3 Seasonal Variations of Aerosol Effects .....	43
1.6 Seasonal Forecast for California.....	47
1.7 Summary and Conclusion .....	49

<b>CHAPTER 2: Impact of Aerosols on Reservoir Inflow: A Case Study for Big Creek Hydroelectric System in California .....</b>	<b>51</b>
2.1 Introduction .....	51
2.2 Literature Review .....	54
2.2.1 Statistical Inflow Forecasting Models .....	54
2.2.2 Impact of Aerosols on Reservoir Inflow .....	55
2.3 Study Area: San Joaquin Region and Big Creek Hydroelectric Project .....	55
2.4 Framework .....	56
2.5 Technical Methods .....	57
2.5.1 Dynamic Regression Model .....	57
2.5.2 WRF-Chem Model .....	60
2.6 Building Inflow Forecasting Model .....	61
2.6.1 Data Description .....	61
2.6.2 Predictor/Variable Selection .....	64
2.6.3 Model Development .....	65
2.7 Quantifying the Impact of Aerosols on Reservoir Inflow .....	76
2.7.1 Evaluation of the WRF-Chem Simulation .....	76
2.7.2 Quantification of the Impact of Aerosols on Reservoir Inflow .....	78
2.8 Summary and Conclusion .....	84
<b>CHAPTER 3: Impact of Aerosol on Hydropower Generation .....</b>	<b>85</b>
3.1 Introduction .....	85
3.2 Hydropower Plant .....	86
3.3 Big Creek hydroelectric Project .....	87
3.4 Hydro Vista Decision Support System .....	90
3.4.1 Vista Modules .....	91
3.5 System Representation .....	93
3.5.1 Physical System Representation .....	93
3.5.2 Load and Transaction opportunities .....	100
3.5.3 Constraints .....	102
3.5.4 Long-term Vista Optimization of Hydropower Generation .....	104
3.6 Method .....	105
3.7 Result and Analysis .....	106
3.7.1 Impact of Aerosols on Big Creek Reservoir Inflows .....	106
3.7.2 Impact of Aerosols on Hydropower and Revenue Generation .....	107
3.8 Conclusion .....	109
<b>REFERENCES .....</b>	<b>110</b>

## LIST OF FIGURES

	Page
Figure 1: Daily Mean Anthropogenic PM2.5 Emission Rate.....	14
Figure 2: Monthly Precipitation (mm/day) from CPC .....	15
Figure 3: Spatial Distribution of Seasonal Mean 550 nm AOD.....	16
Figure 4: Monthly Mean 550 nm AOD and 400-600 nm .....	17
Figure 5: Aerosol Mass ( $\mu\text{g m}^{-3}$ ) for Different Species From OBS .....	18
Figure 6: NO2 and SO2 From EPA (OBS) and the 20km Run at Fresno, California .....	21
Figure 7: PM2.5_Dust, PM2.5, and PM10 From IMPROVE .....	23
Figure 8: Mean Dust Emission Rate ( $\mu\text{g m}^{-2} \text{ s}^{-1}$ ) From the 4km and 4km_D2 Runs.....	23
Figure 9: Relative Contribution (%) of Aerosol Species from IMPROVE and the WRF-Chem (4km and 4km_D2) .....	24
Figure 10: Spatial Distribution of Seasonal Mean 550 nm AOD from the 4km_D2 Run in WY2013.....	25
Figure 11: Vertical Distribution of Seasonal Mean 532 nm Aerosol Extinction Coefficient ( $\text{km}^{-1}$ ).....	25
Figure 12: Vertical Distribution of Season Mean Equivalent Potential Temperature ( $\theta_e$ ; K).....	27
Figure 13: Aerosol Mass ( $\mu\text{g m}^{-3}$ ) for Different Species from OBS, the 4km_D2, 20km_D2 and 20km_P7 Simulations .....	28
Figure 14: Vertical Distribution of Seasonal Mean 532 nm Aerosol Extinction Coefficient ( $\text{km}^{-1}$ ).....	29
Figure 15: Model Simulated (a) LWP ( $\text{g m}^{-2}$ ), (b) IWP ( $\text{g m}^{-2}$ ), (c) Precipitation (mm day-1), (d) SWE (mm), and (e) Temperature at 2 Meters, T2 (K) From the CTRL Simulation, and (f) PRISM Observed Precipitation (mm day-1), Averaged Over October 2012 to June 2013 .....	31
Figure 16: Monthly Mean Precipitation, T2, and SWE .....	31
Figure 17: Spatial Distribution of Aerosol Optical Depth (AOD) Averaged Over October 2012 to June 2013 .....	33
Figure 18: Total Aerosol Effects (CTRL – CLEAN) on Spatial Distribution of Precipitation (mm day-1), SWE (mm), and T2 (K) .....	34

Figure 19: ARI effects (CTRL – NARI) on Spatial Distribution of Precipitation (mm day-1), SWE (mm), and T2 (K).....	35
Figure 20: ASI Effects (CTRL – NASI) on Spatial Distribution of Precipitation (mm day-1), SWE (mm), T2 (K), and Surface Albedo.....	36
Figure 21: Differences in LWP (g m-2), IWP (g m-2), (CTRL – CLEAN), LWP (g m-2), IWP (g m-2), and (NARS – CLEAN).....	37
Figure 22: Differences in ACI Effects .....	37
Figure 23: Effect of Local Anthropogenic Aerosols on Spatial Distribution .....	39
Figure 24: Effect of Local Anthropogenic Aerosols on Dust Aerosols .....	40
Figure 25: Effect of Local Anthropogenic Aerosols on Transported Aerosols.....	41
Figure 26: Monthly Mean AOD Simulated from CTRL for Total Aerosols, Local Anthropocentric Aerosols, Local Dust, and Transported Aerosols .....	43
Figure 27: Monthly Mean Differences in Precipitation (mm day-1).....	44
Figure 28: Monthly Mean Differences in SWE (mm) .....	45
Figure 29: Monthly Mean Differences in T2 (K).....	46
Figure 30: Monthly Mean Differences in Surface Runoff (mm day-1) .....	47
Figure 31: Monthly Mean Precipitation During November 2016 to April 2017.....	48
Figure 32: Precipitation Observations for January 2017 .....	49
Figure 33: The Overall Framework for Quantifying the Impact of Aerosols on Reservoir Inflow .....	57
Figure 34: Study Area With Grid Box and Weather Stations Identified.....	62
Figure 35: Response Variables and the Explanatory Variables for Water Year 2010-2014.....	63
Figure 36: Impulse Response Weights of Input Variable $X_4 D_3$ .....	66
Figure 37: ACF and PACF of Noise Series $N_t$ .....	67
Figure 38: Comparison of Actual Inflow and Inflow Forecast with Observed Meteorological Variables in Water Year 2014 .....	72
Figure 39: Probability Distribution Function (%) of the RMSE of Forecasted Inflow with Perturbed Inputs in Water Year 2014.....	74
Figure 40: Comparison of Actual Inflow, Simulated Inflow, and Simulated Inflow from the Selected Perturbed Input Model with Median RMSE in Water Year 2014.....	75

<b>Figure 41: Comparison of Observed and WRF-Chem CTRL and CLEAN Simulated Meteorological Variables .....</b>	<b>77</b>
<b>Figure 42: Comparison of Actual Inflow, Simulated Inflow from Observed Meteorological .....</b>	<b>79</b>
<b>Figure 43: The Impact of Aerosols on Reservoir Inflow InflowCTRL-InflowCLEANVariables .....</b>	<b>80</b>
<b>Figure 44: The Impact of Aerosols on Reservoir Inflow (InflowCTRL-InflowCLEAN) for the Selected Perturbed Input Model with Median RMSE .....</b>	<b>83</b>
<b>Figure 45: Hydropower Plant Representation.....</b>	<b>87</b>
<b>Figure 46: Big Creek Hydroelectric Project Schematics .....</b>	<b>89</b>
<b>Figure 47: Vista Data Relationships.....</b>	<b>91</b>
<b>Figure 48: Vista DSS Data Input.....</b>	<b>92</b>
<b>Figure 49: System Representation of Hydro Vista DSS .....</b>	<b>94</b>
<b>Figure 50: Schematic of a Single River Single Reservoir .....</b>	<b>95</b>
<b>Figure 51: Products for Transaction in the Electricity Market .....</b>	<b>101</b>
<b>Figure 52: Reserve Categories.....</b>	<b>102</b>

## LIST OF TABLES

	Page
<b>Table 1: Experiment Description for Model Evaluation .....</b>	<b>9</b>
<b>Table 2: Experiment Design for Impacts of Various Aerosol Sources. ....</b>	<b>12</b>
<b>Table 3: Experiment Design for Various Aerosol Pathways .....</b>	<b>13</b>
<b>Table 4: Correlation With Observations for Different Species at Fresno, CA.....</b>	<b>18</b>
<b>Table 5: Surface Aerosol Mass (<math>\mu\text{g m}^{-3}</math>) for Different Species at Fresno, CA .....</b>	<b>19</b>
<b>Table 6: Changes in Surface Temperature (K) and Precipitation, SWE, and Surface Runoff in Percentage Averaged Over October 2012 to June 2013 .....</b>	<b>42</b>
<b>Table 7: Response Variables and the Explanatory Variables for Water from 2010-2014.....</b>	<b>64</b>
<b>Table 8: List of Variables Used in the Dynamic Regression Model.....</b>	<b>65</b>
<b>Table 9: Impulse Response Weights of Input Variable <math>X_4 D_3</math> .....</b>	<b>66</b>
<b>Table 10: Parameter Estimates for Inflow Forecast Model of Florence Lake .....</b>	<b>69</b>

<b>Table 11: Parameter Estimates for Inflow Forecast Model of Lake Edison Results and Analysis.....</b>	<b>70</b>
<b>Table 12: Forecast Error Statistics (cu ft/s) for Water Year 2014.....</b>	<b>71</b>
<b>Table 13: Annual Reservoir Inflow for the Selected Perturbed Input Model with Median RMSE and Reference Model in Water Year 2014 .....</b>	<b>75</b>
<b>Table 14: RMSE of WRF-Chem Simulated Meteorological Variables with Respect to Observed Variables.....</b>	<b>78</b>
<b>Table 15: Annual Reservoir Inflow Under Different Aerosol Conditions.....</b>	<b>81</b>
<b>Table 16: Impact of Aerosols (%) on Annual and Seasonal Reservoir Inflow.....</b>	<b>81</b>
<b>Table 17: Comparison of Impact of Aerosols on Annual and Seasonal Reservoir Inflow for the Reference and Selected Perturbed Input Model with Median RMSE... </b>	<b>83</b>
<b>Table 18: Annual Reservoir Inflow under Different Aerosol Conditions.....</b>	<b>107</b>
<b>Table 19: Impact of Aerosols (%) on Annual and Seasonal Reservoir Inflow.....</b>	<b>107</b>
<b>Table 20: Impact of Aerosols on Total Hydropower Generation and Revenue in Water Year 2015.....</b>	<b>108</b>
<b>Table 21: Impact of Aerosols on Hydropower Generation Revenue Based on Revenue Type in Water Year 2015.....</b>	<b>108</b>

# EXECUTIVE SUMMARY

## Introduction

Recent studies have shown that aerosols, which are small solids or liquid particles suspended in ambient air, can substantially influence temperature, precipitation, and snowpack in California through their interactions with clouds. These interactions warm or cool the atmosphere, potentially changing how fast snow in the Sierra Nevada melts. The speed at which snow melts influences the flow of water to hydropower reservoirs, which, in turn, affects hydroelectricity generation. Hydropower is a clean source of electricity in California, and its generation during the summer is important to provide electricity during peak demand days, driven by the increased use of air conditioning units. The scientific community, however, had not quantified the effects of aerosols on hydropower generation before the execution of this project.

## Project Purpose

This project developed an innovative and comprehensive framework for evaluating the effect of aerosols on hydropower generation in California. The framework seamlessly integrated the numerical weather forecasting model WRF-Chem (the Weather Research and Forecasting model coupled with Chemistry), a statistical inflow forecast model, and a hydroelectric power plant optimization model (Vista). Vista is a model used by Southern California Edison (SCE) to operate their Big Creek Hydroelectric System. The main outcome was determining the operational and economic impacts of aerosols on operating the Big Creek system.

## Project Approach

The research team enhanced and used a version of the WRF-Chem model that included fully coupled aerosol-meteorology-snowpack interactions to investigate the effects of various aerosol sources on precipitation and snowpack in California. For example, how aerosols affect clouds and how clouds change the nature of the aerosols. In particular, the research team investigated the impacts of locally emitted and dust aerosols, and aerosols that originated outside California. The team examined several modeling options to best simulate snowpack conditions, temperature, and other weather variables via a series of comparisons of modeling results with observations from ground-based meteorological and hydrological stations and satellite data. The team used Florence Lake and Lake Thomas Alva Edison of the Big Creek Hydroelectric Project in the San Joaquin Region for water years 2013 and 2014 as the case study for this project. Finally, they used Vista, a hydropower management model used by SCE, to facilitate transferring information and results to SCE.

## Project Results

The research team found an average reduction of precipitation from aerosols during October 2013 to June 2014 of about 7 percent. The team also found a 3 percent reduction for snow water equivalent and a 7 percent reduction in surface runoff (flows

of water) for the whole domain; the effects are even more pronounced in the mountaintops. The reduction in snow water equivalent is also more significant during a dry year, with a 9 percent reduction for the whole domain and 16 percent for the mountaintops.

The case study on the Florence Lake and Lake Thomas Alva Edison of the Big Creek Hydroelectric Project in the San Joaquin Region for water years 2013 and 2014 suggests that the presence of aerosols results in a significant reduction of annual reservoir inflow (flow of water to the reservoirs) by 4 to 14 percent.

Finally, the team calculated the effect of aerosols on hydropower generation and revenue for water year 2015 by feeding the inflow forecasts of all of the lakes of the Big Creek Hydroelectric System both with and without considering the impact of aerosols into the Vista Decision Support System. The results suggest that aerosols significantly reduce hydropower generation by 89,356 MWh in water year 2015, which is a 5.61 percent reduction in the annual hydropower generation. This translates to a \$2.8 million loss in revenue in a water year for Southern California Edison. This significant revenue loss due to aerosols provides another justification for stricter environmental regulations to reduce anthropogenic aerosol emissions.

### **Knowledge Transfer**

The research team worked very closely with representatives from SCE and disseminated results by participating in technical conferences and publishing journal papers. This study is the first study to quantify the generation and costs impacts of aerosols on the operation of a hydropower system located in the Sierra Nevada. This study suggests that considering the effect of aerosols on precipitation and streamflow in rivers could significantly improve hydrological forecasts. The Technical Advisory Committee for this project consisted of technical representatives from SCE, the California Department of Water Resources, and the California Energy Commission.

SCE staff co-authored a publication with the research team showcasing the results of the study and presented the results at a national conference organized by the Institute of Electrical and Electronic Engineering.

SCE requested and received one long-term forecast from the research team to help them manage their Big Creek Hydroelectric Project. Additional resources will be necessary to provide this service to SCE for future years to run the models and interpret the results.

### **Benefits for California**

The Energy Commission used the results of this study to inform the design of a new modeling system to create the next generation of climate scenarios for California's Fifth Climate Change Assessment. Energy Commission staff included the requirement for the new modeling system in a call for proposals that successfully ended in a new on-going research project. This new modeling system will simulate the effects of aerosols on climate for the rest of this century. The climate projections generated for the Energy

Commission so far have been the foundation of past studies about the effects of climate change to the energy system and the other sectors of the economy that have been a part of past California climate change assessments. These climate scenarios have also been used to developed long-term plans to manage energy, water, forestry, and other resources in California by the relevant state agencies such as the Energy Commission, CalFire, and the California Department of Water Resources. In addition, the Governor's Office of Planning and Research requires the use of the climate scenarios developed for the Energy Commission for all state activities dealing with climate adaptation in California.

# CHAPTER 1: Aerosol Seasonal Variability and Impacts on Seasonal Precipitation and Snowpack

---

## 1.1 Introduction

Water resources in California are derived predominantly from precipitation (mostly during the wintertime) and storage in the snowpack in the Sierra Nevada. Snowpack provides about one-third of the water used by California's cities and farms. The fresh water stored in the snowpack gradually releases through runoff into river flows during the warm and dry season. The amount and timing of snowmelt are critical factors in determining water resources in this region. It is important to understand the factors influencing precipitation and snowpack on seasonal timescale for water management and hydropower operation.

The 2012-2014 California drought has been attributed to warming and anomalously low precipitation (Griffin and Anchukaitis, 2014). Previous studies suggested that warming trends are amplified in mountains compared to lowlands (Pepin et al., 2015). The amplified warming in mountain areas, also referred to as elevation-dependent warming, is generally attributed to a few important processes (Pepin et al., 2015), such as water vapor changes and latent heat release, surface water vapor changes, radiative flux changes associated with three-dimensional rugged topography (Gu et al., 2012a; Liou et al., 2013; Lee et al., 2015; Zhao et al., 2016), and snow-albedo feedback (Leung et al., 2004). A review and assessment of the mechanisms contributing to an enhanced warming over mountain areas is given in Pepin et al. (2015).

In addition to the warming effects of greenhouse gases, aerosols may have substantial impacts on water resources in California. Recent observational and numerical modeling studies have shown that aerosol pollutants can substantially change precipitation and snowpack in California (for example Rosenfeld et al., 2008a; Qian et al., 2009a; Hadley et al., 2010; Ault et al., 2011; Creamean et al., 2013, 2015; Fan et al., 2014; Oaida et al., 2015). Lee and Liou (2012) illustrated that roughly 26 percent of snow albedo reduction from March to April over the Sierra Nevada is caused by an increase in aerosol optical depth (AOD).

In California, aerosols can be generated locally or transported from remote sources. Among local aerosol types, dust comprises a significant fraction over California (Wu et al., 2017). Based on a four-month, high intensity record of size-segregated particulate matter (PM) samples collected from a high elevation site, Vicars and Sickman (2011) found that the mass concentration of coarse atmospheric PM in the southern Sierra Nevada, California, was dominated by contribution from dust (50 to 80 percent) throughout the study period. Dust aerosols can exert important impact on radiative

forcing and regional climate in California through its interaction with radiation (e.g., Zhao et al., 2013a) as well as its role as cloud condensations nuclei for cloud formation (such as Fan et al., 2014). Anthropogenic aerosols are geographically distributed because of localized emission sources, the short atmospheric residence time, and regional topography. With valleys and surround mountain barriers, dispersion of air pollutants is more difficult for locally emitted anthropogenic air pollution. The anthropogenic aerosols can cause changes in atmospheric circulation and regional climate especially where the aerosol concentrations are high and the synoptic atmospheric systems are not prominent (for example Qian et al., 2003; Fast et al., 2006; Rosenfeld et al., 2008a; Zhao et al., 2013a).

Besides the local aerosol sources, the atmospheric transport of aerosol pollutants from the Asian continent (such as Jiang et al., 2007; Wang et al., 2015; Hu et al., 2016) is also a significant contributor to aerosol loading throughout the Pacific basin. Asian aerosols can reach relatively high concentrations above the marine boundary layer in the western US, representing as much as 85 percent of the total atmospheric burden of PM at some sites (VanCuren, 2003). Trans-Pacific dust transport has been found to be particularly relevant in high-elevation regions such as the Sierra Nevada, which typically represents free-tropospheric conditions due to the limited transport of lowland air pollutants and predominance of upper air subsidence (VanCuren et al., 2005). Observations from the CalWater campaign demonstrated that dust and biological aerosols transported from northern Asia and the Sahara were present in glaciated high-altitude clouds in the Sierra Nevada coincident with elevated ice nuclei (IN) particle concentrations and ice-induced precipitation (Ault et al., 2011; Creamean et al., 2013).

Aerosols can influence precipitation, snowpack and regional climate through three pathways. First, aerosol-radiation interaction (ARI, also known as aerosol direct effect), can warm the atmosphere but cool the surface, resulting in changes in thermodynamic environment for cloud and precipitation and the delay of the snowmelt (Charlson et al., 1992; Kiehl and Briegleb, 1993; Hansen et al., 1997; Koren et al., 2004; Gu et al., 2006, 2016, 2017). Second, aerosol-cloud interaction (ACI, also known as aerosol indirect effect), which is related to aerosols serving as cloud condensation nuclei (CCN) and IN. By changing the size distribution of cloud droplets and ice particles, aerosol may affect cloud microphysics, radiative properties and precipitation efficiency, thus affect the atmospheric hydrological cycle and energy balance (Twomey, 1977; Jiang and Feingold, 2006; Rosenfeld et al., 2008b; Qian et al., 2009b; Gu et al., 2012b). Third, aerosol-snow interaction (ASI). When aerosols (mainly absorbing aerosols, such as dust and black carbon) are deposited on snowpack, they can reduce snow albedo and affect snowmelt (Warren and Wiscombe, 1985; Jacobson, 2004; Flanner et al., 2007; Qian et al., 2011, 2015; Zhao et al., 2014). Numerical experiments have shown that ARI reduces the surface downward radiation fluxes, cools the surface and warms the atmosphere over California (Kim et al., 2006; Zhao et al., 2013a), which could subsequently impact clouds, precipitation and snowpack. In a 2-D simulation, Lynn et al. (2007) shows that ACI decreases orographic precipitation by 30 percent over the length of the mountain slope.

Fan et al. (2014) showed that ACI increases the accumulated precipitation of an Atmospheric River event by 10 to 20 percent from the Central Valley to the Sierra Nevada due to a ~40 percent increase in snow formation. Snow impurities (ASI) increase ground temperature, decrease snow water, shorten snow duration and cause earlier runoff (Jacobson, 2004; Painter et al., 2007, 2010; Qian et al., 2009a; Waliser et al., 2011; Oaida et al., 2015).

This study investigated the seasonal variations of aerosols and the impacts of various aerosol sources on seasonal precipitation and snowpack in California using a fully coupled high-resolution aerosol-meteorology-snowpack model. The researchers distinguish and quantify the impacts of aerosols from local emissions and transport, and the roles of different prevailing aerosol types in California, particularly dust and anthropogenic aerosols.

The unique contributions of this study are:

1. The researchers configured WRF-Chem model for successful use in California region and conducted WRF-Chem simulations that capture aerosol variations in the San Joaquin Valley (SJV), especially in the cold season.
2. The researchers found that high-resolution model simulation could better resolve inhomogeneous distribution of anthropogenic emissions in urban areas, resulting in better simulation of aerosols.
3. The researchers quantified the impact of aerosols on seasonal precipitation and snowpack and found that various aerosol sources in California may influence the region through different pathways.
4. The researchers provided seasonal forecast for precipitation and snowpack in California.

The remainder of this chapter is organized as follows. Section 1.2 provides existing studies using numerical models to investigate the effects of aerosols. Section 1.3 presents the technical methods and data used in this study, including observations, model description, and experiment design. Section 1.4 provides the evaluation of the WRF-Chem model and the seasonal variations of aerosols in SJV. Section 1.5 presents the impact of aerosols on seasonal precipitation and snowpack in California. Section 1.6 provides a 6-month forecast over California. Lastly, concluding remarks are given in Section 1.7.

## **1.2 Literature Review**

Chemical transport models are a useful tool to understanding the formation and evolution of aerosols and their impacts on air quality, weather and climate. However, it is quite challenging to accurately simulate aerosol properties (Fast et al., 2014). Fast et al. (2014) summarized the factors contributing to the errors in regional-scale modeling of aerosol properties. They include 1) emission sources; 2) meteorological parameterizations; 3) representation of aerosol chemistry; 4) limited understanding of

the formation processes of secondary organic aerosol (SOA); 5) spatial resolution; and 6) boundary conditions.

As one of the advanced regional air quality models available presently to the community, the Weather Research and Forecasting model with Chemistry (WRF-Chem) has been widely used to study aerosols and their impacts on regional air quality, weather and climate (for example Misenis and Zhang, 2010; Zhang et al., 2010; Zhao et al., 2010; 2013a, 2013b; 2014; Gao et al., 2011; Wu et al., 2011a, 2011b, 2013; Fast et al., 2012, 2014; Scarino et al., 2014; Tessum et al., 2015; Campbell et al., 2016; Hu et al., 2016). For example, Fast et al. (2014) showed that WRF-Chem simulations at 4 kilometer (km) horizontal resolution captured the observed meteorology and boundary layer structure over California in May and June of 2010 and the spatial and temporal variations of aerosols were reasonably simulated. Aerosol simulations by WRF-Chem are usually sensitive to local emission and long-range transport of aerosols from the boundary conditions provided by the global Model for Ozone and Related chemical Tracers, version 4 (MOZART-4). With a similar model set-up, Zhao et al. (2013b) conducted a one-year simulation at 12 km horizontal resolution and found that the WRF-Chem model represented the observed seasonal and spatial variation of surface particulate matter (PM) concentration over California. However, underestimation of elemental carbon (EC) and organic matter (OM) were noticed in the model simulation, with weak sensitivity to horizontal resolution.

Although recent studies showed that aerosols can substantially influence precipitation and snowpack in California, they focused only on one of the aerosol sources or on a single event or one pathway. A complete account of the aerosol impacts from different sources through three pathways on regional climate in California has not been presented yet. In addition, large seasonal and spatial variation of aerosol occurrence and distribution are observed in the California Central Valley, such as the San Joaquin Valley (SJV). Improved understanding of the aerosol variability and impacts is necessary to provide further guidance for emission control strategies in the California.

## 1.3 Technical Methods

### 1.3.1 Observations

*Column-integrated Aerosol Optical Properties.* AOD is a measure of column-integrated light extinction by aerosols and a proxy for total aerosol loading in the atmospheric column. The Aerosol Robotic Network (AERONET) provides ground measurements of AOD every 15 minutes during daytime under clear skies (Holben et al., 1998), with an accuracy approaching  $\pm 0.01$  (Eck et al., 1999; Holben et al., 2001; Chew et al., 2011). The monthly level 2.0 AOD product with cloud screening and quality control is used in this study. Ångström exponent (AE) is an indicator of aerosol particle size. Small (large) AE values are generally associated with large (small) aerosol particles (Ångström, 1929; Schuster et al., 2006). The AE between 0.4  $\mu\text{m}$  and 0.6  $\mu\text{m}$  is derived from AERONET observed AODs, and is used to evaluate the model-simulated AE. For comparison with

simulated AOD, AERONET AOD is interpolated to 0.55  $\mu\text{m}$  from 0.50  $\mu\text{m}$  and 0.675  $\mu\text{m}$  using the AE. In the SJV, only one AERONET station at Fresno, CA (36.79°N, 119.77°W) has regular observations throughout the California water year 2013 (WY2013) from October 2012 to September 2013.

The Multiangle Imaging Spectroradiometer (MISR) (Diner et al., 1998) instrument onboard the Terra satellite has provided global coverage of AOD once a week since December 1999. The standard MISR retrieval algorithm provides AOD observations at 17.6 km resolution using 16x16 pixels of 1.1 km  $\times$  1.1 km each. About 70 percent of MISR AOD retrievals are within 20 percent of the paired AERONET AOD, and about 50 percent of MISR AOD falls within 10 percent of the AERONET AOD, except in dusty and hybrid (smoke+dust) sites (Kahn et al., 2010). The researchers use version 22 of Level 3 monthly AOD product at 0.5° resolution in this study.

*Surface Mass Concentration.* Surface PM<sub>2.5</sub> speciation and PM<sub>10</sub> (particulate matter with diameter  $\leq 10 \mu\text{m}$ ) data are routinely collected by two national chemical speciation monitoring networks: Interagency Monitoring of Protected Visual Environments (IMPROVE) and the PM<sub>2.5</sub> National Chemical Speciation Network (CSN) operated by Environmental Protection Agency (EPA) (Hand et al. 2011; Solomon et al., 2014). IMPROVE collects 24-h aerosol speciation every third day at mostly rural sites since 1988. The same frequency of aerosol speciation dataset was collected at EPA CSN sites in urban and suburban areas since 2000. The observed organic carbon is converted to OM by multiplying by 1.4 (Zhao et al., 2013b; Hu et al., 2016). Some precursors of aerosol pollutions (such as NO<sub>2</sub> and SO<sub>2</sub>) are observed hourly by EPA (data available at: [https://aqsdrl.epa.gov/aqsweb/aqstmp/airdata/download\\_files.html](https://aqsdrl.epa.gov/aqsweb/aqstmp/airdata/download_files.html)) and are used in this study. Selected IMPROVE and EPA CSN sites used in this study are shown in Figure 1-1a.

*Aerosol Extinction Profile.* The aerosol extinction coefficient profile reflects the attenuation of the light passing through the atmosphere due to the scattering and absorption by aerosol particles as a function of range. Version 3 Level 2 532 nm aerosol extinction profiles derived from Cloud-Aerosol Lidar with Orthogonal Polarization (CALIOP) backscatter profiles collected onboard the Cloud-Aerosol Lidar and Infrared pathfinder Satellite Observation (CALIPSO) satellite are used (Omar et al., 2009; Young and Vaughan, 2009). Seasonal mean profiles are derived for WY2013 based on the methodology outlined in Campbell et al. (2012), whereby quality-assurance protocols are applied to individual profiles before aggregating and averaging the data. The researchers highlight that no individual profiles are included in the averages if the CALIOP Level 2 retrieval failed to resolve any extinction within the column, a potential issue to create bias that has recently been described by Toth et al. (2017). Level 2 532 nm aerosol extinction data classify aerosols into six types: clean marine, dust, polluted continental, clean continental, polluted dust and smoke. Dust and polluted dust are distinguished in the averages in this study for their contribution to total extinction and the vertical profile seasonally in the SJV.

### 1.3.2 Model Description

The WRF-Chem model Version 3.5.1 (Grell et al., 2005) updated by Pacific Northwest National Laboratory (PNNL) is used in this study (Zhao et al., 2014). This study uses the CBM-Z (carbon bond mechanism) photochemical mechanism (Zaveri and Peters, 1999) coupled with the sectional-bin MOSAIC (Model for Simulating Aerosol Interactions and Chemistry) aerosol scheme (Zaveri et al., 2008) as the chemical driver. The major components of aerosols (nitrate, ammonium, EC, primary OM, sulfate, sea salt, dust, water and other inorganic matter) as well as their physical and chemical processes are simulated in the model. For computational efficiency, aerosol particles in this study are partitioned into four-sectional bins with dry diameter within 0.039-0.156  $\mu\text{m}$ , 0.156-0.625  $\mu\text{m}$ , 0.625-2.5  $\mu\text{m}$ , and 2.5-10.0  $\mu\text{m}$ . Zhao et al. (2013a) compared the effect of aerosol size partition on dust simulations. It showed that the 4-bin approach reasonably produces dust mass loading and AOD compared with the 8-bin approach. The size distribution of the 4-bin approach follows that of the 8-bin approach with coarser resolution, resulting in  $\pm 5$  percent difference on the ratio of  $\text{PM}_{2.5}\text{-dust}/\text{PM}_{10}\text{-dust}$  in dusty regions (more large particles and less small particles). Dust number loading and absorptivity are biased high in the 4-bin approach compared with the 8-bin approach.

Aerosols are considered to be spherical and internally mixed in each bin (Barnard et al., 2006; Zhao et al., 2013b). The bulk refractive index for each particle is calculated by volume averaging in each bin. Mie calculations as described by Ghan et al. (2001) are used to derive aerosol optical properties (such as extinction, single-scattering albedo, and the asymmetry parameter for scattering) as a function of wavelength. Aerosol radiation interaction is included in the shortwave and longwave radiation schemes (Fast et al., 2006; Zhao et al., 2011). By linking simulated cloud droplet number with shortwave radiation and microphysics schemes, aerosol cloud interaction is effectively simulated in WRF-Chem (Chapman et al., 2009). Aerosol snow interaction is implemented in this version of WRF-Chem (Zhao et al., 2014) by considering aerosol deposition on snow and the subsequent radiative impacts through the SNICAR (SNow, ICe, and Aerosol Radiative) model (Flanner and Zender, 2005, 2006). Table 1 shows the different model configurations used to evaluate the modeling results.

**Table 1: Experiment Description for Model Evaluation**

Experiment ID	Experiment description
20km	Simulation with the GOCART dust scheme at 20 km horizontal resolution.
20km_D2	Same as 20km, but with the DUSTRAN dust scheme.
20km_P7	Same as 20km_D2, but with the ACM2 PBL scheme.
4km	Same as 20km, but at 4 km horizontal resolution.
4km_D2	Same as 4km, but with the DUSTRAN dust scheme.

Source: University of California, Riverside

The model simulations start on September 1, 2012 and run continuously for 13 months. With the first month used for the model spin-up, the researchers' analysis focuses on WY2013 from October 2012 to September 2013. The model is configured with 40 vertical levels and a model top at 50 hPa. The vertical resolution from the surface to 1 km gradually increases from 28 m to 250 m. The model center is placed at 38°N, 121°W, with  $250 \times 350$  grid points at 4 km horizontal resolution, referred to as "4km", covering California and the surrounding area (Table 2). To test the sensitivity of the aerosol simulations to horizontal resolution, the team conducted one simulation with the same model settings and domain coverage at 20 km horizontal resolution (referred to as "20km").

The physics parameterizations used in the simulations include the Morrison double-moment microphysics scheme (Morrison et al., 2009), Rapid Radiative Transfer Model for General circulation model (RRTMG) shortwave and longwave radiation schemes (Iacono et al., 2008), Community Land Model (CLM) Version 4 land surface scheme (Lawrence et al., 2011). The Yonsei University (YSU) planetary boundary layer (PBL) scheme (Hong et al., 2006) is used in all of the simulations, except one sensitivity experiment that uses the ACM2 (Asymmetric Convective Model with non-local upward mixing and local downward mixing; Pleim, 2007) PBL scheme (referred to as "20km\_P7"). Previous studies showed that YSU and ACM2 schemes have good performance in simulating boundary layer properties (such as Hu et al., 2010; Xie et al., 2012; Cuchiara et al., 2014; Banks and Baldasano, 2016; Banks et al., 2016; Chen et al., 2017). Subgrid convection, convective transport of chemical constituents and aerosols, and wet deposition from subgrid convection are parameterized using the Grell 3D ensemble cumulus scheme (Grell and Devenyi, 2002) in the 20 km simulations while convective processes are resolved in the 4 km simulations. The ERA-Interim reanalysis serves as initial and boundary meteorological conditions for WRF-Chem. The MOZART-4 global chemical transport model (Emmons et al., 2010) is used for initial and boundary chemical conditions. Fast et al. (2014) found that the MOZART-4 model overestimates aerosols in the free troposphere over California, which is also found in one of the researchers' sensitivity experiments. Following Fast et al. (2014), the chemical initial and boundary conditions from MOZART-4 are divided by two in all simulations except 20km\_BC1.

Anthropogenic emissions are provided by US EPA 2005 National Emissions Inventory (NEI05), with area-type emissions on a structured 4-km grid and point-type emissions at specific latitude and longitude locations (US EPA, 2010). Nineteen gases (including  $\text{SO}_2$ , NO,  $\text{NH}_3$  etc.) are emitted, and aerosol emissions include  $\text{SO}_4$ ,  $\text{NO}_3$ , EC, organic aerosols, and total  $\text{PM}_{2.5}$  and  $\text{PM}_{10}$  masses. Anthropogenic emissions are updated every hour to account for diurnal variability, while its seasonal variation is not considered in the simulations. A sensitivity experiment with 2011 NEI emissions does not produce significantly different results from the 2005 NEI emissions. Biogenic emissions are calculated online using the Model of Emissions of Gases and Aerosols from Nature (MEGAN) model (Guenther et al., 2006). Biomass burning emissions are obtained from

the Global Fire Emissions Database version 2.1, with eight-day temporal resolution (Randerson et al., 2007) and updated monthly. Sea salt emissions are derived from the PNNL-updated sea salt emission scheme that includes the correction of particles with radius less than 0.2  $\mu\text{m}$  (Gong et al., 2003) and dependence on sea surface temperature (Jaeglé et al., 2011).

Following Zhao et al. (2013b), dust emission is computed from the GOCART (Goddard Global Ozone Chemistry Aerosol Radiation and Transport) dust scheme (Ginoux et al., 2001) in the 20km and 4km simulations. The GOCART dust scheme estimates the dust emission flux  $F$  as

$$F = CSs_p u_{10m}^2 (u_{10m} - u_t) \quad ,$$

where  $C$  is an empirical proportionality constant,  $S$  is a source function for potential wind erosion that is derived from  $1^\circ \times 1^\circ$  GOCART database (Freitas et al., 2011),  $s_p$  is a fraction of each size class dust in emission,  $u_{10m}$  is 10-m wind speed, and  $u_t$  is a threshold speed for dust emission.

As shown later, a significant amount of dust is observed in the SJV, whereas the GOCART dust scheme produces little dust. Two sensitivity experiments at 20 km and 4 km horizontal resolution (referred to as “20km\_D2” and “4km\_D2”, respectively) are conducted by switching the dust emission scheme to the DUST TRANsport model (DUSTRAN) scheme (Shaw et al., 2008). The DUSTRAN scheme estimates  $F$  as

$$F = \alpha C u_*^4 \left(1 - \frac{f_w u_{*t}}{u_*}\right) \quad ,$$

where  $C$  is an empirical proportionality constant,  $\alpha$  is the vegetation mask,  $u_*$  is the friction velocity,  $u_{*t}$  is a threshold friction velocity, and  $f_w$  is the soil wetness factor. The  $C$  value in GOCART and DUSTRAN is highly tunable for different regions. The original  $C$  values,  $1.0 \mu\text{g s}^2 \text{m}^5$  in GOCART (Ginoux et al., 2001) and  $1.0 \times 10^{-14} \text{ g cm}^{-6} \text{ s}^{-3}$  in DUSTRAN (Shaw et al., 2008), are used in this study.

### 1.3.3 Experiment Design

Since the model explicitly considers different sources and types of aerosols and contains the physical processes to represent various aerosol effects (ARI, ASI, and ACI), it is useful to decompose the aerosol effects based on aerosol sources/types and pathways. Note that the overall aerosols effects are not a simple sum of different aerosol sources/types, nor a linear combination of the ARI, ASI, and ACI effects. Differences between various simulations, however, help to identify the effect of a single source or pathway and the decomposition approach is a common practice in the experiment design of modeling studies. To examine the overall aerosol effects and the roles of locally generated and transported aerosols, the following five experiments have been designed (Table 2):

**Table 2: Experiment Design for Impacts of Various Aerosol Sources.**

Experiment	Anthropogenic Aerosols	Dust Aerosol	Transport	Description
CTRL	Y	Y	Y	Control experiment with all aerosol emissions/transport included
NoLocDust	Y	N	Y	Local dust aerosol emission is not included
NoLocAnth	N	Y	Y	Local anthropogenic aerosol emissions are not included
NoTran	Y	Y	N	Aerosols transported from outside the model domain are not included
CLEAN	N	N	N	Aerosol emissions/transport are not included

**CTRL:** This is the control experiment with all aerosol emissions and transports included in the simulation.

Source: University of California, Riverside

2) NoLocDust: This experiment is performed without any local dust emission. Differences between the CTRL and NoLocDust experiments illustrate the effect of dust aerosols locally emitted.

3) NoLocAnth: This experiment is similar to NoLocDust, except that emissions of local anthropogenic aerosols are turned off. Comparison between CTRL and this experiment will elucidate the effect of local anthropogenic aerosols.

4) NoTran: The initial and boundary chemical conditions in the CTRL simulation are taken from the global Model for Ozone and Related Chemical Tracers, version 4 (MOZART-4; Emmons et al., 2010). The chemical species transported into the model domain include organic carbon, black carbon, sulfate, nitrate, ammonium, sea salt, dust, etc. In the NoTran experiment, aerosols transport from outside the model domain, including those from East Asia and other regions, are not considered by setting the lateral boundary conditions for aerosols to zero. Differences between CTRL and NoTran will show the effect of transported aerosols.

5) CLEAN: This experiment is performed without any local aerosol emissions or transport from outside the model domain while all the transported chemical species are kept, and therefore represents a scenario of clean condition. Aerosols are low in the simulation, but not zero, possibly due to aerosol chemistry. The CCN concentration at supersaturation of 0.1 percent is on the order of  $10 \text{ cm}^{-3}$  at most times of the CLEAN simulation. The distribution of liquid water path and ice water path in the CLEAN

simulation is also similar to that in the CTRL simulation, with differences in magnitude. Differences between the CTRL and CLEAN experiments would illustrate the effects of all primary aerosol types, including those locally emitted and transported from outside the domain.

To distinguish the pathways through which the aerosols influence the precipitation and snowpack, the researchers also conducted a few other experiments (Table 3):

6) NARI: This experiment is similar to the CTRL run, except that ARI is not included. Comparison between CTRL and this experiment will elucidate the effect of ARI.

7) NASI: This experiment is similar to the CTRL run, except that ASI is not included. Comparison between CTRL and this experiment will show the effect of ASI.

8) NARS: This experiment is similar to the CTRL run, except that both ARI and ASI are not included. By comparing this experiment and CLEAN, the effect due to ACI can be examined.

**Table 3: Experiment Design for Various Aerosol Pathways**

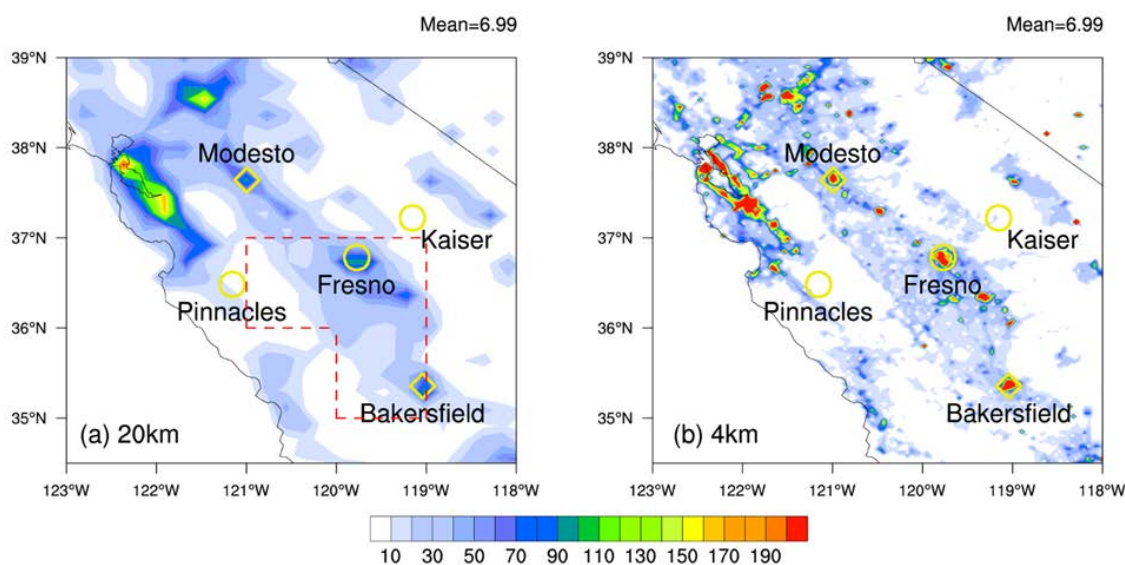
Experiment	ARI	ACI	ASI	Description
NARI	N	Y	Y	ARI is not included
NASI	Y	Y	N	ASI is not included
NARS	N	Y	N	ARI and ASI are not included

Source: University of California, Riverside

## 1.4 Model Evaluation

Shown in Figure 1, the researchers' model domain includes three urban sites (Fresno, Bakersfield and Modesto) and two rural sites (Pinnacles and Kaiser) where surface measurements of aerosols are available. Because aerosols properties and model performance are similar at all urban sites, the researchers' discussion is focused on the results at Fresno.

**Figure 1: Daily Mean Anthropogenic PM<sub>2.5</sub> Emission Rate**



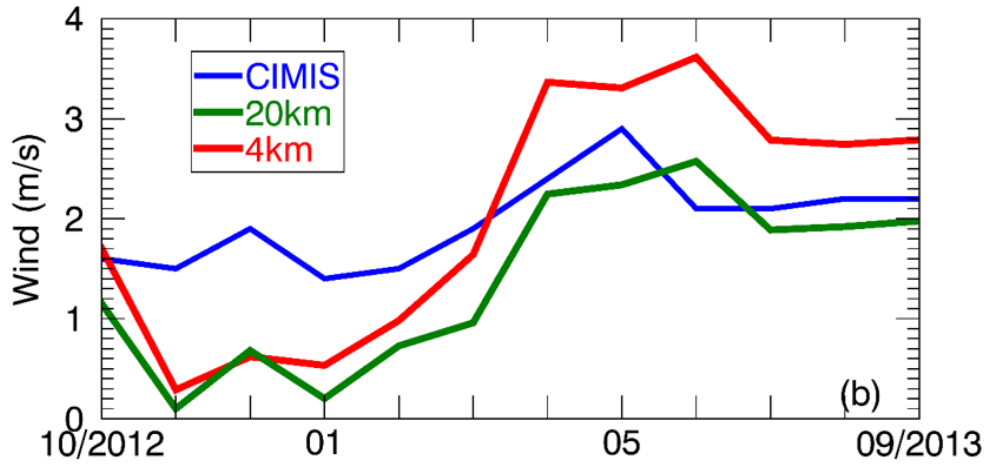
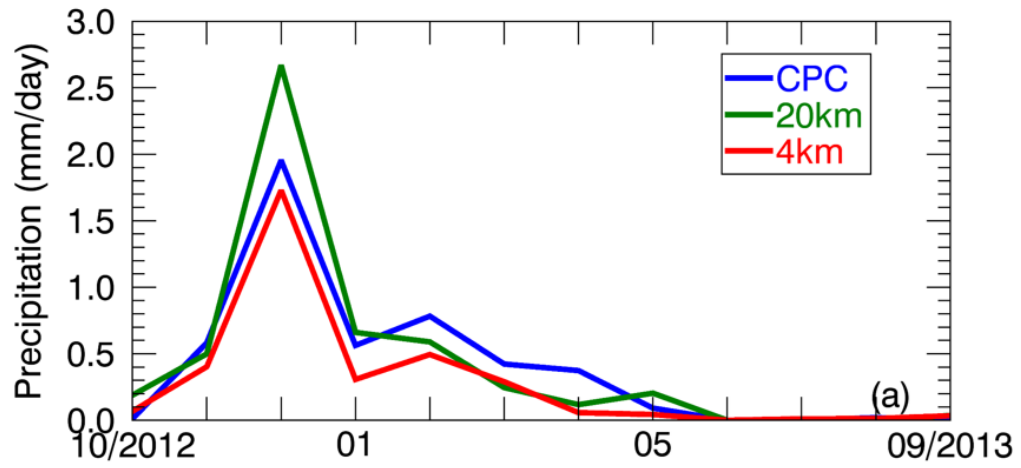
Source: University of California, Riverside

### 1.4.1 Sensitivity to Horizontal Resolution

Daily mean anthropogenic PM<sub>2.5</sub> emission rates used in the 20km and 4km simulations, respectively are featured. Although both emission rates are derived from the 4 km NEI05 dataset, localized high emission rates with sharp gradients are evident in urban areas from the 4km simulation. The 20km simulation exhibits lower emission rates at the urban areas with weaker gradients due to the reappportionment process. As precipitation is an important process that removes aerosols, the researchers examine the simulated precipitation for the 20km and 4km runs and find that the 20km simulation produces 51 percent more precipitation, although the domain-averaged precipitation is lower in the 20km run than the 4km run (Figure 2).

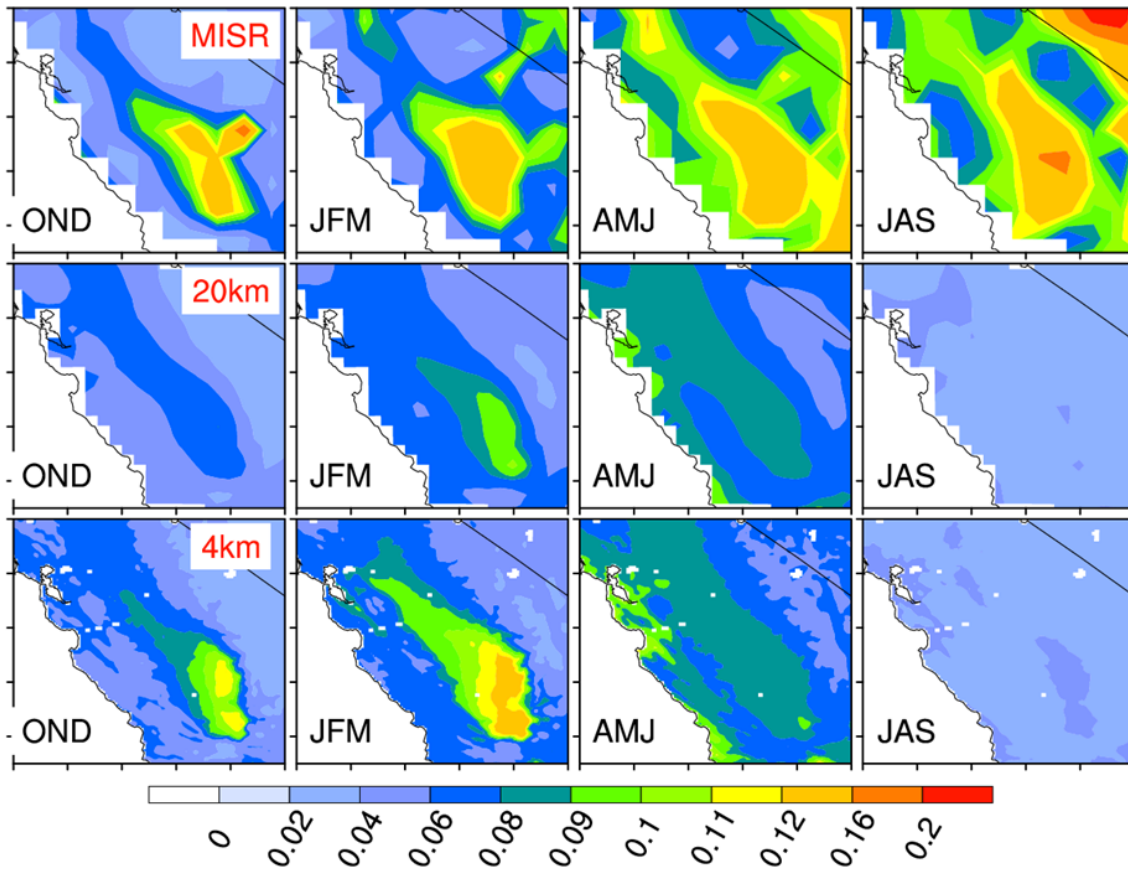
Consistent with higher emission rates and lower precipitation at Fresno, the 4km run simulates higher AOD than the 20km run in the cold season - October-November-December and January-February-March; OND and JFM. (Figure 3). Averaged over a broad area encompassing Fresno and Bakersfield, the most polluted region in the SJV, the AOD is 0.090 in the 4km and 0.073 in the 20km, a 23 percent difference. Compared to the MISR observations, the 4km simulation reproduces the spatial distribution and magnitude of AOD in the cold season. However, the AOD difference between the 20km and 4km runs is small in the warm season (April-May-June and July-August-September; AMJ and JAS ), and both runs underestimate AOD by ~50 percent with respect to the MISR observations.

Figure 2: Monthly Precipitation (mm/day) from CPC



Source: University of California, Riverside

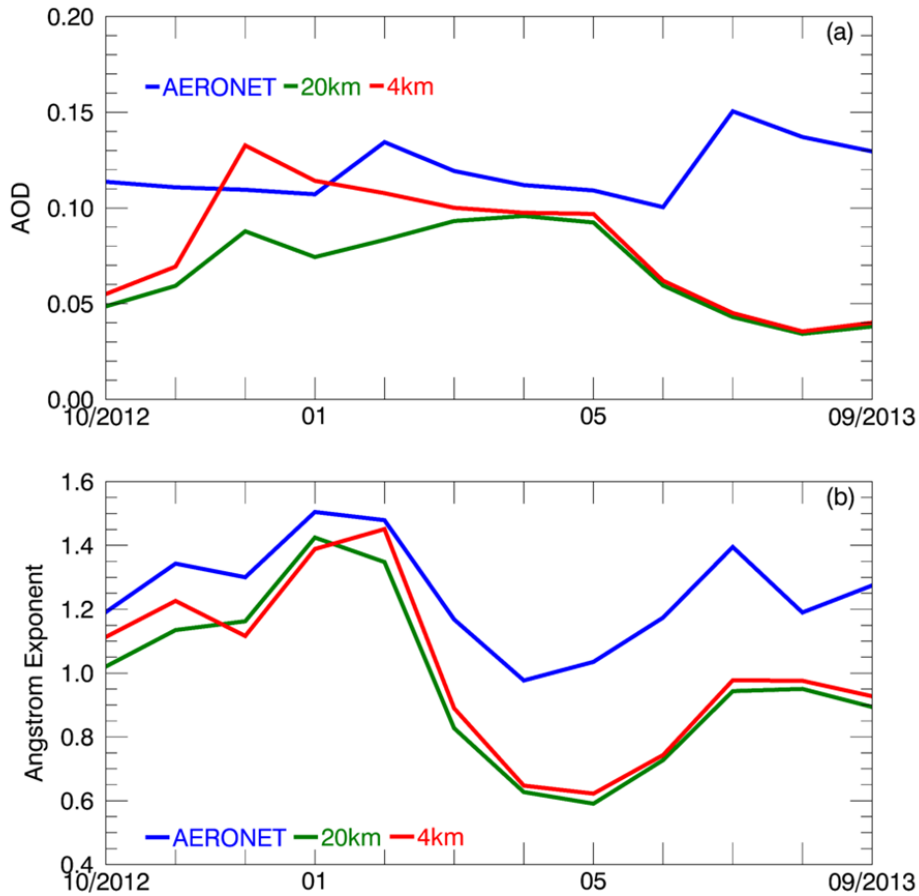
Figure 3: Spatial Distribution of Seasonal Mean 550 nm AOD



Source: University of California, Riverside

Comparing the point values at Fresno in the 4km and 20km simulations (Figure 4), the researchers find similar results: the 4km AOD is closer to the AERONET measurements and is about 23 percent higher than that in the 20km run during the cold season, while both runs are biased low in AOD during the warm season. The different model sensitivities to horizontal resolution between the cold and warm seasons suggest that the dominant aerosol sources may be different for the two seasons. The researchers will elaborate upon the aerosol composition in the following section. MISR and AERONET observations display weak seasonal AOD variation in the SJV and at Fresno, respectively, which is not well represented in the 20km and 4km simulations.

**Figure 4: Monthly Mean 550 nm AOD and 400-600 nm**



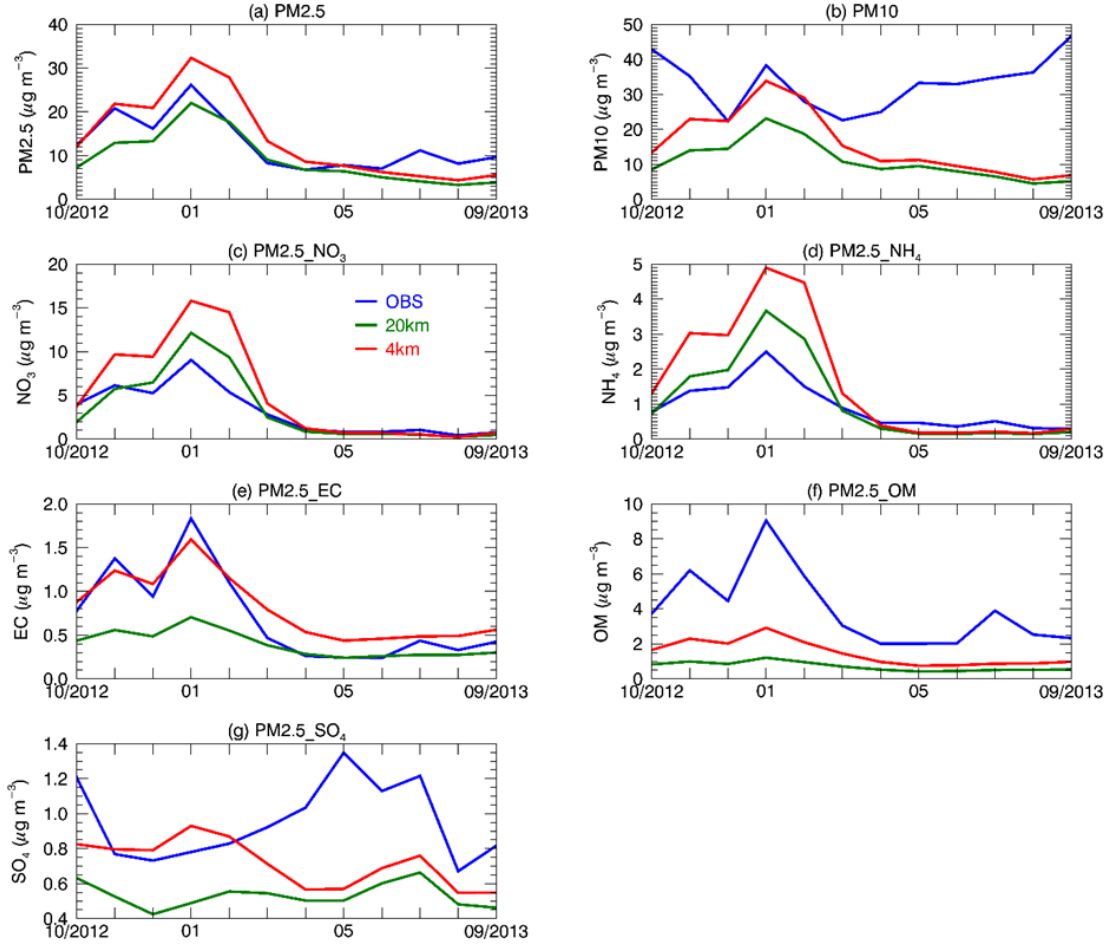
Source: University of California, Riverside

Aside from AOD, significant seasonal variability of AE is shown at Fresno. AE exhibits a maximum about 1.50 in January and a minimum of 0.98 in April, suggesting relatively small particles in the winter and large particles in the spring. A relatively large AE value of 1.40 (corresponding to small particles) is observed in July, possibly related to the wild fires in late July in the SJV. WRF-Chem captures the seasonal variability of the AE well, with a correlation of 0.90 in the 20km and 4km simulations. The magnitude of AE is also approximately simulated in the cold season, with a mean of 1.15 (1.20) in the 20km (4km) runs compared to 1.33 in the observation. However, the simulated AE is underestimated by ~30 percent in the warm season, indicating that the simulated particle size is biased high during this period.

Significant seasonal variability of  $PM_{2.5}$  is observed in the SJV urban areas (Figure 5).  $PM_{2.5}$  at Fresno peaks in January ( $26.18 \mu g m^{-3}$ ) and reaches a minimum of  $7.03 \mu g m^{-3}$  in June, with an annual nonattainment value of  $12.64 \mu g m^{-3}$ . The 20km and 4km runs approximately capture the observed seasonal variability of  $PM_{2.5}$ , with a correlation around 0.90 (Table 4). In the cold season, the 4km simulation overestimates  $PM_{2.5}$  by 27

percent while the 20km simulation exhibits a low bias of 19 percent compared with IMPROVE observations at Fresno (Table 5). The 4km simulation of PM<sub>10</sub> is in good agreement with IMPROVE in the winter (December, January and February), but has significant low biases of between 30 and 85 percent in other months. The 20 km simulation underestimates PM<sub>10</sub> throughout WY2013.

**Figure 5: Aerosol Mass ( $\mu\text{g m}^{-3}$ ) for Different Species From OBS**



Source: University of California, Riverside

**Table 4: Correlation With Observations for Different Species at Fresno, CA**

Species	20km	4km	4km_D2	20km_D2	20km_P7
PM <sub>2.5</sub>	0.89	0.90	0.86	0.78	0.03
PM <sub>2.5</sub> _NO <sub>3</sub>	0.94	0.95	0.94	0.94	0.91
PM <sub>2.5</sub> _NH <sub>4</sub>	0.97	0.96	0.96	0.98	0.96
PM <sub>2.5</sub> _OM	0.93	0.93	0.94	0.93	0.91

PM <sub>2.5</sub> _EC	0.98	0.98	0.98	0.98	0.96
PM <sub>2.5</sub> _SO <sub>4</sub>	0.63	-0.16	-0.14	0.61	0.63
PM <sub>2.5</sub> _dust	-0.55	-0.50	0.48	0.55	0.36
PM <sub>10</sub>	-0.25	-0.23	-0.08	0.01	-0.03

Source: University of California, Riverside

**Table 5: Surface Aerosol Mass ( $\mu\text{g m}^{-3}$ ) for Different Species at Fresno, CA**

Species	Cold season						Warm season					
	OBS	20km	4km	4km_ D2	20km_ D2	20km_ P7	OBS	20km	4km	4km_ D2	20km_ _D2	20km _P7
PM <sub>2.5</sub>	16.84	13.71	21.38	22.48	14.90	13.77	8.44	4.91	6.29	12.85	10.12	14.85
PM <sub>2.5</sub> _N O <sub>3</sub>	5.43	6.36	9.54	9.22	6.22	3.16	0.84	0.55	0.69	0.79	0.66	0.57
PM <sub>2.5</sub> _N H <sub>4</sub>	1.42	1.97	2.99	2.88	1.91	0.98	0.40	0.19	0.24	0.20	0.16	0.13
PM <sub>2.5</sub> _O M	5.39	0.92	2.07	2.07	0.93	1.04	2.47	0.49	0.87	0.87	0.50	0.55
PM <sub>2.5</sub> _EC	1.08	0.52	1.12	1.13	0.52	0.58	0.32	0.27	0.49	0.49	0.27	0.30
PM <sub>2.5</sub> _SO <sub>4</sub>	0.87	0.53	0.82	0.81	0.53	0.46	1.04	0.54	0.61	0.60	0.53	0.49
PM <sub>2.5</sub> _du st	0.90	0.11	0.11	1.65	1.50	4.18	2.08	0.04	0.03	6.49	5.16	10.05
PM <sub>10</sub>	31.55	14.93	22.81	28.32	20.10	24.52	34.82	7.08	8.69	38.12	30.19	48.02

Source: University of California, Riverside

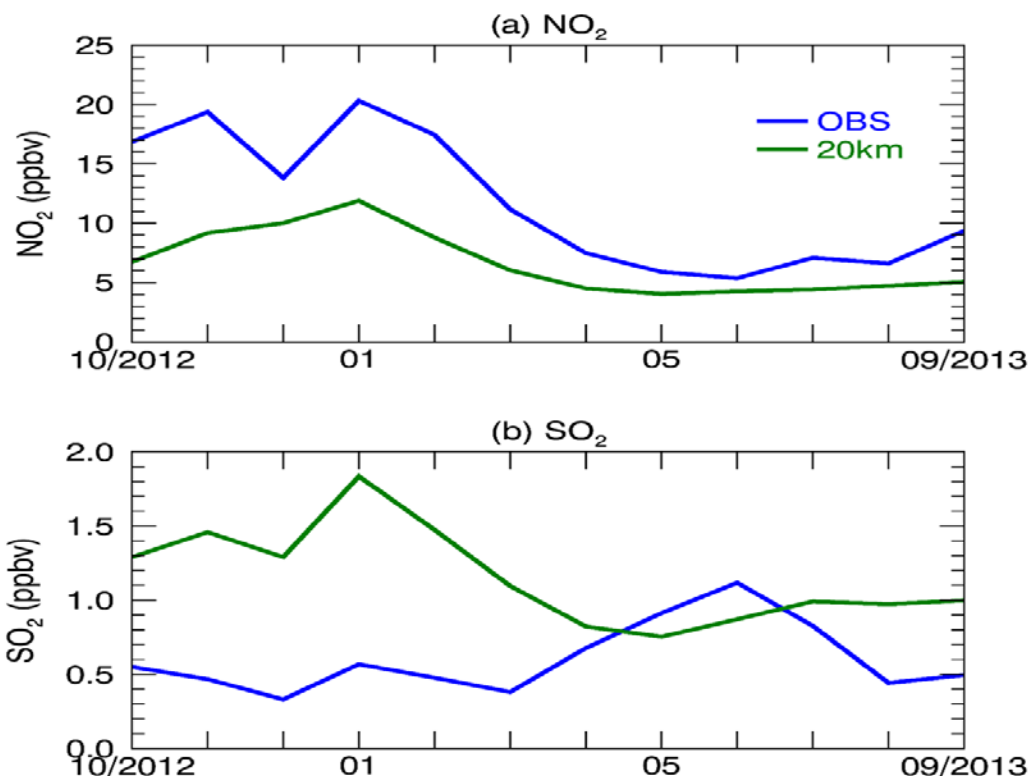
PM<sub>2.5</sub> is a mixture of nitrate (NO<sub>3</sub>), ammonia (NH<sub>4</sub>), OM, EC, sulfate (SO<sub>4</sub>), dust and other aerosols. High concentrations of PM<sub>2.5</sub> are primarily the result of NO<sub>3</sub> at Fresno (Figure-5 [c]). Both simulations produce the seasonal variability of NO<sub>3</sub> with a correlation of 0.94, but high bias of 17 percent (75 percent) is found in the 20km (4km) simulations during the cold season. As one precursor of NO<sub>3</sub>, NO<sub>2</sub> is underestimated by 43 percent in the 20km run (Figure 6[a]). The overestimation in NO<sub>3</sub> and underestimation in NO<sub>2</sub> suggest that the precursor emissions may not be the reason for the high biases in NO<sub>3</sub>. NH<sub>4</sub> shows a similar performance to NO<sub>3</sub>, with an overestimation by 38 percent (111 percent) in the 20km (4km) runs during the cold seasons. As shown later in section 1.4.3, both NO<sub>3</sub> and NH<sub>4</sub> simulations are quite sensitive to the PBL scheme applied.

OM, the second largest contributing species to cold season PM<sub>2.5</sub> in the SJV (Table 5), is significantly underestimated by 82 percent in the 20km simulation. The 4km simulation produces higher OM, but it is still lower than the IMPROVE observations by 63 percent. Underestimating OM is expected, because SOA processes are not included in the researchers' model infrastructure. Fast et al. (2014) used the simplified two-product volatility basis set parameterization to simulate equilibrium SOA partitioning in WRF-Chem although SOA was still underestimated in their simulation. It remains ongoing research how to correctly represent SOA processes in regional climate models.

Both the 20km and 4km simulations reproduce the seasonal variability of EC, with a correlation of 0.98 between the modeled and observed time series (Table 4). The 20km simulation underestimates EC by 52 percent (16 percent) in the cold (warm) season (Figure 5[e] and Table 5). The 4km simulated EC (1.12  $\mu\text{g m}^{-3}$ ) exhibits good agreement with IMPROVE (1.08  $\mu\text{g m}^{-3}$ ) in the cold season, but overestimates EC by 53 percent in the warm season.

The seasonal variability of SO<sub>4</sub> at Fresno is very different from other PM<sub>2.5</sub> species. It peaks in May at 1.35  $\mu\text{g m}^{-3}$  and reaches the minimum of 0.67  $\mu\text{g m}^{-3}$  in August (Figure 5[g]). The 20km simulated SO<sub>4</sub> exhibits good correlation of 0.63 with the observation (Table 4), but is biased low by 28 to 63 percent throughout WY2013. Although the observed SO<sub>2</sub>, the precursor of SO<sub>4</sub>, has approximately similar seasonal variation to the observed SO<sub>4</sub> (Figure 6[b]), the 20km simulated seasonal variability of SO<sub>2</sub> resembles other anthropogenic emissions, with high values in the cold season and low values in the warm season, out of phase with the simulated SO<sub>4</sub> and the observed SO<sub>2</sub>. The 4km simulation produces higher SO<sub>4</sub> than the 20km run, resulting in better agreement with the observation (0.82  $\mu\text{g m}^{-3}$  vs. 0.87  $\mu\text{g m}^{-3}$ ) during the cold season (Figure 5[g] and Table 5). However, the 4km run produces an increase of SO<sub>4</sub> by only 13 percent comparing to the 20km run in the warm season, resulting in a correlation of -0.16 between the 4km simulation and the observation.

Figure 6: NO<sub>2</sub> and SO<sub>2</sub> From EPA (OBS) and the 20km Run at Fresno, California



Source: University of California, Riverside

To explore the possible cause for underestimating SO<sub>4</sub> and SO<sub>2</sub> in the warm season in the 20km and 4km simulations, the researchers conduct a sensitivity experiment with different chemical boundary conditions from the baseline runs. The researchers find that SO<sub>4</sub> in the SJV is partly contributed to by marine intrusions (the different chemical boundary conditions between 20km\_BC1 and 20km\_D2) throughout the year, as pointed out by Fast et al. (2014). Including the marine intrusions, the 20km\_BC1 simulated SO<sub>4</sub> tracks the observation at a correlation of 0.78. Doubled chemical boundary conditions in the 20km simulation results in 41 percent increase in SO<sub>4</sub> at Fresno, with a stronger increase in the warm season. Compared to the observed SO<sub>4</sub> of 1.04  $\mu\text{g m}^{-3}$  in the warm season, the simulated SO<sub>4</sub> of 0.79  $\mu\text{g m}^{-3}$  in the 20km\_BC1 run is closer to the observation than that simulated in the 20km\_D2 run (0.53  $\mu\text{g m}^{-3}$ ). The relative contributions of local emissions and remote transports (as well as other emission sources, such as wild fires) to SO<sub>4</sub> concentrations in different seasons of the SJV require further investigation.

Overall, the 4km simulation produces higher AOD and surface PM than the 20km simulation in urban areas of the SJV, especially during the cold season, resulting in better agreement with satellite and surface observations than the 20km simulation. Both the 20km and 4km simulations approximately capture the seasonal variability of PM<sub>2.5</sub> and most of its speciation. However, significant low biases of AOD and PM<sub>10</sub> are found

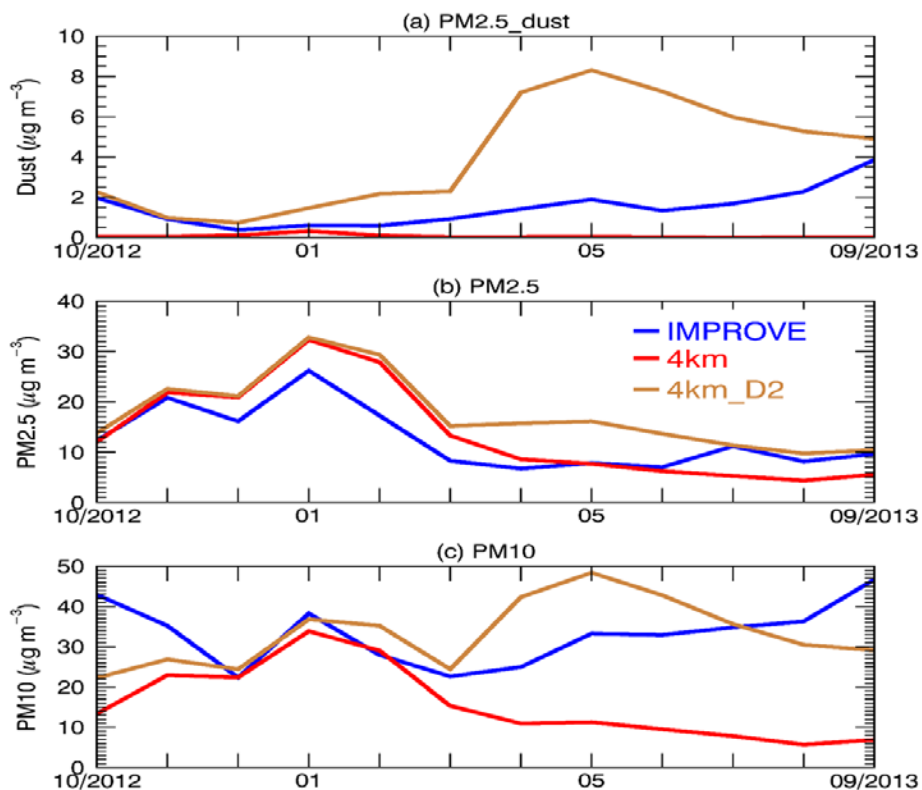
during the warm season in both simulations. The underestimation also exists in a sensitivity experiment (not shown) with the same model setups except initialized in April, indicating that the identified model biases during the warm season are not caused by potential model drift after a relatively long simulation period. The relatively good performance in simulating  $PM_{2.5}$  but not  $PM_{10}$  during the warm season suggests that coarse aerosol particle mass (CM;  $10 \mu m \geq$  particulate matter with diameter  $> 2.5 \mu m$ ), mainly dust in the SJV, is not properly represented in the model. The impact of dust parameterizations is investigated in the 4km\_D2 experiment.

#### 1.4.2 Sensitivity to Dust Scheme

Limited amounts of  $PM_{2.5\_dust}$  (dust with diameter  $\leq 2.5 \mu m$ ) are observed in the SJV cold season, with a minimum of  $0.37 \mu g m^{-3}$  in December (Figure 7). The amount of  $PM_{2.5\_dust}$  increases in the warm season, with a peak of  $3.86 \mu g m^{-3}$  in September. The 4km simulation produces comparable  $PM_{2.5\_dust}$  relative to IMPROVE in the winter, but almost no dust in other months (Figure 8 [upper panel]). On the other hand, the dust emission rate in the 4km\_D2 run is significantly higher than the 4km run. The researchers have found that the source function, S, for potential wind erosion in the SJV is set to zero in the  $1^\circ \times 1^\circ$  GOCART dataset used for the 4km simulation. An updated source function, S, at higher resolution is needed for the GOCART dust scheme to correctly represent dust emissions in the SJV.

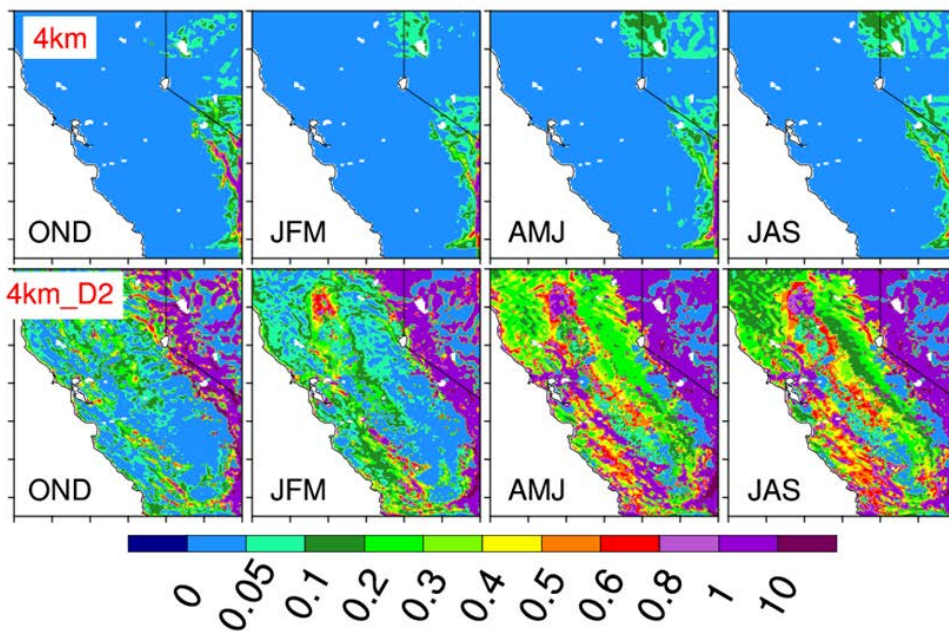
The 4km\_D2 simulation reproduces the amount of  $PM_{2.5\_dust}$  in OND. However, it overestimates  $PM_{2.5\_dust}$  by up to a factor of three in the warm season, resulting in an overestimation of  $PM_{2.5}$  by 52 percent (Figure 7[b] and Table 5).  $PM_{2.5\_dust}$  is not sensitive to long-range transport (from chemical boundary conditions in the model simulation). Both the 4km and 4km\_D2 simulations capture the seasonal variability of  $PM_{2.5}$ , but not that of  $PM_{10}$  (Figure 7[c]). The magnitude of  $PM_{10}$  in the 4km\_D2 run is larger than the 4km simulation.  $PM_{10}$  in the 4km\_D2 run is overestimated in April-May-June (AMJ) but underestimated in July-August-September (JAS), leading to a comparable season mean of  $38.12 \mu g m^{-3}$  with IMPROVE observed  $34.82 \mu g m^{-3}$ . The overestimation of AMJ  $PM_{10}$  and  $PM_{2.5\_dust}$  in the 4km\_D2 run is likely associated with the high bias in the simulated wind speed.

**Figure 7: PM2.5\_Dust, PM2.5, and PM10 From IMPROVE**



Source: University of California, Riverside

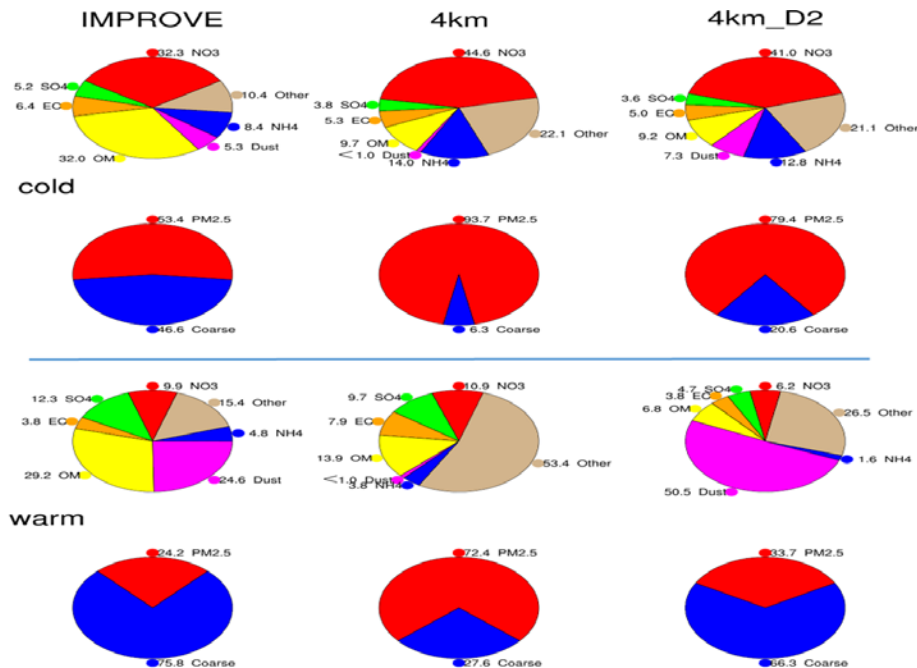
**Figure 8: Mean Dust Emission Rate ( $\mu\text{g m}^{-2} \text{s}^{-1}$ ) From the 4km and 4km\_D2 Runs**



Source: University of California, Riverside

On the relative contribution of different aerosol species, IMPROVE observations at Fresno show that  $\text{NO}_3$  is the primary contributor (32.3 percent) to  $\text{PM}_{2.5}$  while only 5.3 percent of  $\text{PM}_{2.5}$  is dust in the cold season (Figure-9 [Panel 1]). The 4km and 4km\_D2 runs roughly reproduce the relative contributions to  $\text{PM}_{2.5}$  in the cold season, with an overestimation of  $\text{NO}_3$  and  $\text{NH}_4$  and an underestimation of OM, consistent with the time series in Figure 5. Relative contributions of dust to  $\text{PM}_{2.5}$  are better simulated in the 4km\_D2 run (7.3 percent than the 4km one (<1.0 percent)). IMPROVE shows that 46.6 percent of  $\text{PM}_{10}$  is CM in the cold season (Figure 9 [Panel 2]). The 4km (6.3 percent) and 4km\_D2 (20.6 percent) runs underestimate the contribution of CM to  $\text{PM}_{10}$ , mainly in October and November. In the warm season, dust (24.6 percent) becomes the primary contributor to  $\text{PM}_{2.5}$  while the contribution from  $\text{NO}_3$  decreases to 9.9 percent in IMPROVE observations Figure 9 [Panel 3]). Almost no  $\text{PM}_{2.5}$ \_dust is simulated in the 4km run while too much  $\text{PM}_{2.5}$ \_dust is produced in the 4km\_D2 (50.5 percent) run during the warm season. The relative contribution of CM to  $\text{PM}_{10}$  is too small (27.6 percent) in the 4km run, while the 4km\_D2 run reflects an better relative contribution of 66.3 percent (as compared to an IMPROVE observed 75.8 percent (Figure 9 [Panel 4])).

**Figure 9: Relative Contribution (%) of Aerosol Species from IMPROVE and the WRF-Chem (4km and 4km\_D2)**

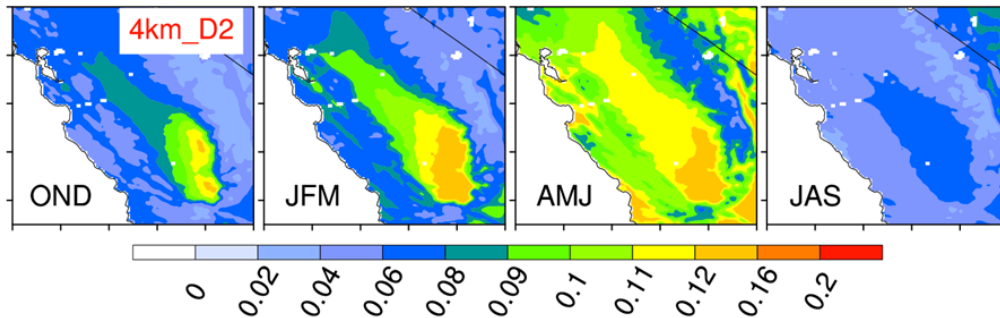


Source: University of California, Riverside

AOD simulations are improved in the 4km\_D2 experiment (Figure 10), with better agreement found from MISR in AMJ. AOD (0.114) in the 4km\_D2 run is comparable to observations (0.131) in AMJ, but still underestimated by 53 percent in JAS. Consistent with AOD, the vertical distribution of aerosol extinction is reasonably simulated during the cold season in the WRF-Chem simulations, while large discrepancies are found in the

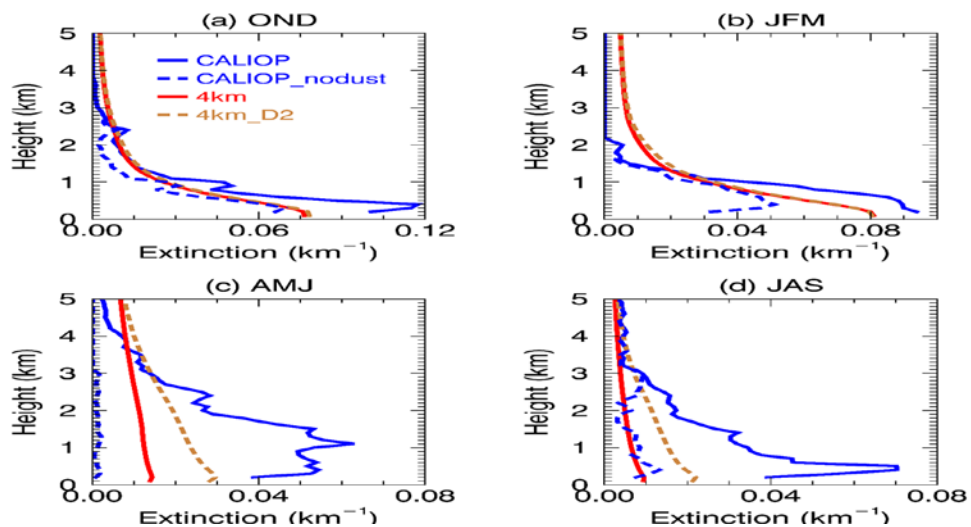
warm season (Figure 11). As observed by CALIOP at 532 nm, aerosols are confined below 1 km in the cold season and decrease sharply with height. During AMJ, aerosols are well mixed between the surface and the altitude of 1.5 km and then decrease with height gradually. During JAS, the well-mixed aerosol layer is shallower than that in AMJ and the vertical profile of aerosol extinction is in-between the cold season and AMJ. Model simulations roughly capture the “bottom-heavy” structure of the extinction profiles observed by CALIOP especially in the cold season, but significant biases exist. One common problem for all four seasons is the low bias in the boundary layer and high bias in the free atmosphere. Similar discrepancy between the model simulations and CALIOP is shown in other studies (Wu et al., 2011a; Hu et al., 2016). The model does not capture the well-mixed aerosol layer during AMJ. The difference in the aerosol extinction profiles between the 4km and 4km\_D2 runs is small during the cold season.

**Figure 10: Spatial Distribution of Seasonal Mean 550 nm AOD from the 4km\_D2 Run in WY2013**



Source: University of California, Riverside

**Figure 11: Vertical Distribution of Seasonal Mean 532 nm Aerosol Extinction Coefficient (km<sup>-1</sup>)**



Source: University of California, Riverside

Dust in the boundary layer is a primary factor contributing to aerosol extinction in the SJV, as illustrated by the differences between the bulk seasonal CALIOP mean profile and those excluding the contributions of the dust and polluted dust (CALIOP\_nodust) profiles. Simulated aerosol extinction falls between the two in all seasons, suggesting that dust is the primary factor contributing to the model biases in aerosol extinction. Although a small portion of PM<sub>2.5</sub> is dust in the cold season, it contributes to about 50 percent of total aerosol extinction (Figure 11[a] and [b]). A predominant portion of aerosol extinction in the lower troposphere is contributed by dust in the warm season (Figure 11[c] and [d]). There, the 4km\_D2 simulation produces higher aerosol extinction between 0.3 km and 3 km than the 4km simulation, although it is still lower than CALIOP. The simulated aerosol extinction in the free troposphere is close to or larger than CALIOP, suggesting that aerosols transported from remote areas through chemical boundary conditions may not be the major factor contributing to the underestimation of dust between 0.3 km and 3 km in the SJV.

Overall, the poor simulations of dust play a dominant role in the low bias of aerosols in the boundary layer during the warm season. The GOCART and DUSTRAN dust emission schemes used in this study have difficulties in reproducing dust emissions in the SJV, with an underestimation in GOCART and an overestimation in DUSTRAN. Improvement on the dust emission schemes is needed for capturing the seasonal variability of aerosols in the SJV.

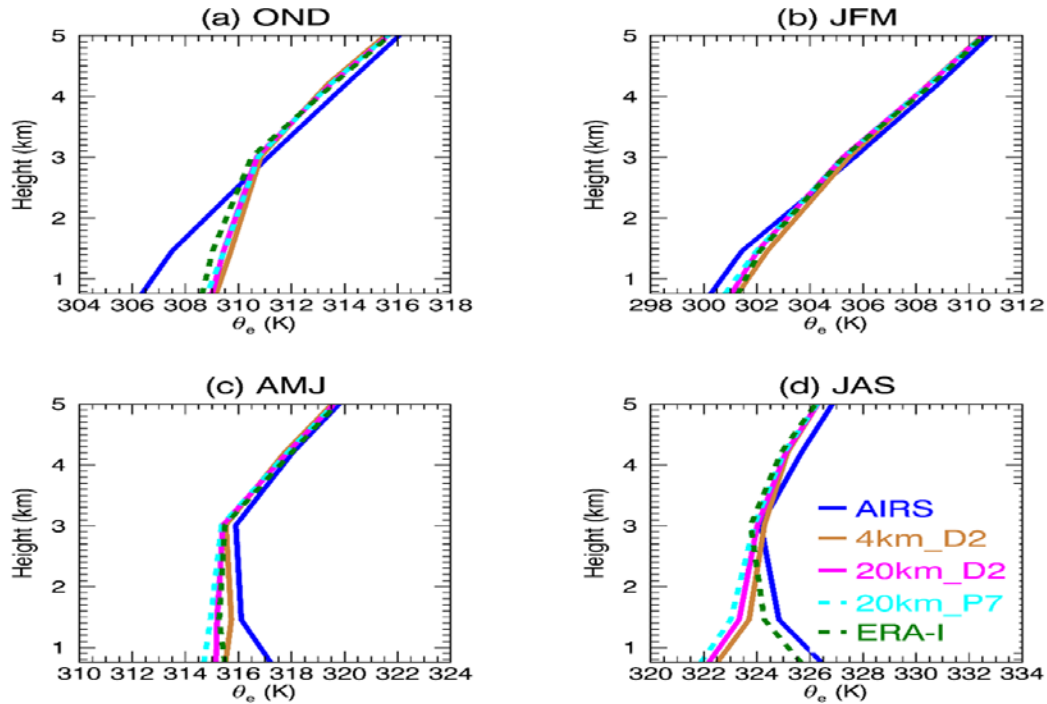
### 1.4.3 The Role of Meteorology

The WRF-Chem simulations approximately reproduce the seasonal variations of meteorological variables near the surface (correlations > 0.80), including temperature, RH, wind speed and precipitation. All of the model simulations exhibit warm and dry biases near surface and in the boundary layer, with cold and wet biases in the free atmosphere. The dry bias in the 4km\_D2 run is about 10 percent near the surface throughout WY2013. Due to the relative dry environment (RH<50 percent) in the warm season, the underestimation of boundary layer aerosol extinction and column-integrated AOD is unlikely caused by the hygroscopic effects (Feingold and Morley, 2003). In the cold season, the surface wind speed is underestimated by 0.67 m s<sup>-1</sup> (1.00 m s<sup>-1</sup>) in the 4km\_D2 (20km\_D2) runs. In the warm season, the 4km\_D2 run overestimates wind speed by 0.78 m s<sup>-1</sup>, while the 20km\_D2 run has an underestimation of 0.16 m s<sup>-1</sup>. These results suggest that wind speed is not a major factor contributing to the low biases of aerosols in the boundary layer between 0.3 km and 3 km. Furthermore, the seasonal variability of precipitation is well captured in the simulations, while the magnitude of precipitation is weaker than the observations during the warm season. Thus, the researchers conclude that wet removal processes would not be a primary reason for the aerosol biases in the warm season.

In the warm season, more aerosols are observed above 1.5 km than in the cold season. A well-mixed layer of aerosols is observed below 1.5 km in AMJ, consistent with the unstable lower troposphere below 1.5 km shown in AIRS and ERA-Interim (Figure 12).

The WRF-Chem model simulates neutral (or weakly stable) layers below 1.5 km, which may limit uplifting of aerosols from the surface, failing to create a deep well-mixed layer of aerosols. Although the dust emission at the surface is overestimated in AMJ in the 4km\_D2 run, the simulated neutral or weakly stable thermal structure does not favor convective vertical mixing, resulting in the low biases of aerosols between 0.3 km and 3 km.

**Figure 12: Vertical Distribution of Season Mean Equivalent Potential Temperature ( $\theta_e$ ; K)**



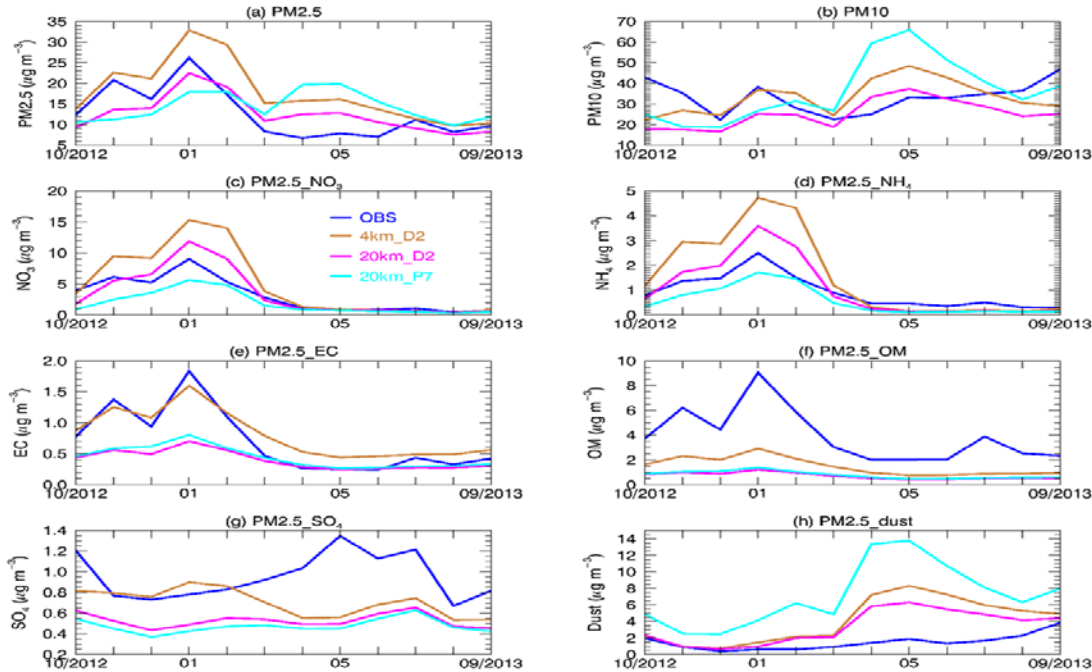
Source: University of California, Riverside

Similar biases of aerosol and instability in the lower troposphere are also shown in JAS (Figure 11[d] and Figure 12[d]). The stable boundary layer limits vertical transport of aerosols from the surface, contributing to the low bias of column-integrated AOD in JAS. In JAS, aerosol extinction close to the CALIOP observation is simulated in the free atmosphere, suggesting that the low bias in AOD is not due to the halved chemical boundary conditions from MOZART-4. In the cold season, in spite of some discrepancies in the magnitude of atmospheric stability, all of the simulations capture the stable lower troposphere (Figure 12[a] and [b]), consistent with relatively good performance of aerosol simulations in the cold season.

As biases in the model simulations are found mainly within the boundary layer, a sensitivity experiment is conducted at 20 km resolution using the ACM2 PBL scheme (20km\_P7). Although the changes in the meteorological variables (not shown) and atmospheric static stability are rather small, the simulated surface NO<sub>3</sub> and NH<sub>4</sub> in the 20km\_P7 run decrease by 50 percent compared to the 20km\_D2 run (Figure 13).

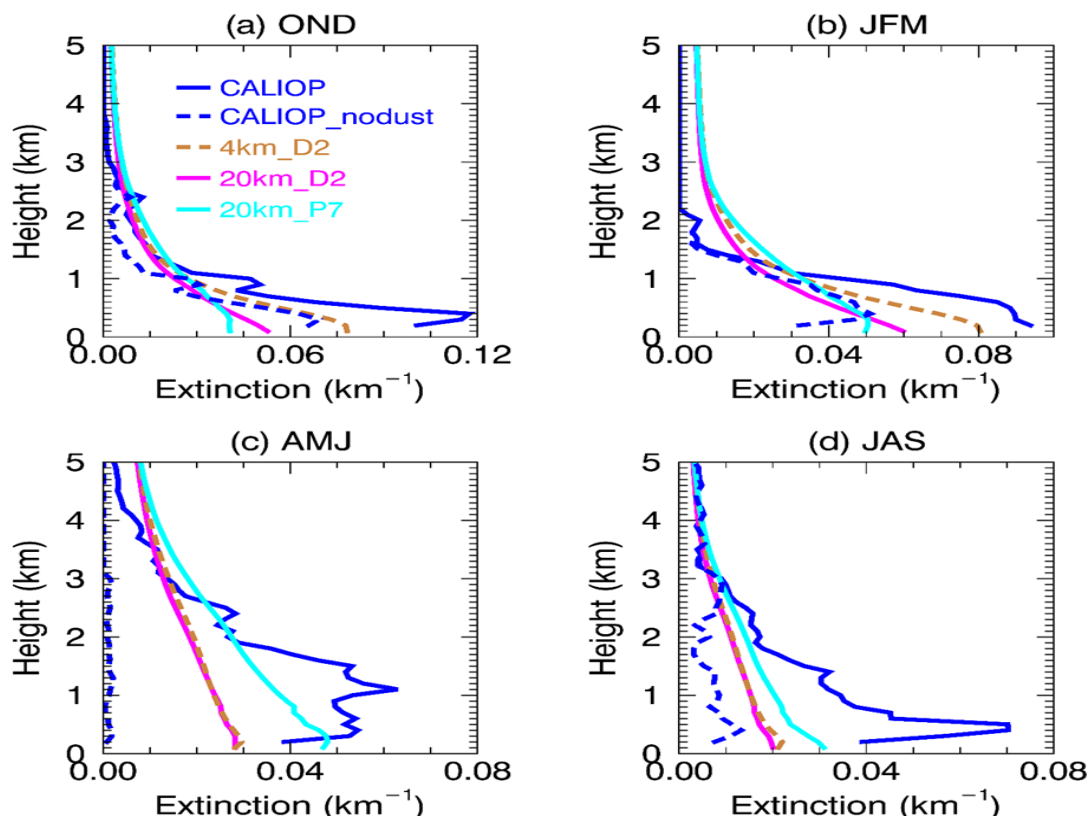
Considering that more  $\text{NO}_3$  and  $\text{NH}_4$  are simulated at 4 km resolution than at 20 km resolution as shown in section 2.4.1, the use of the ACM2 PBL scheme at 4 km simulation would largely resolve the high biases of  $\text{NO}_3$  and  $\text{NH}_4$  in the 4km\_D2 simulation. The decrease of  $\text{NO}_3$  and  $\text{NH}_4$  near the surface is because more aerosols are transported to the layers above 0.5 km (Figure 14 [a] and [b]), possibly resulting from different convective vertical mixing in the PBL schemes. However,  $\text{PM}_{2.5\_dust}$  is significantly overestimated by a factor of 4 in the 20km\_P7 simulation (Figure 14 [h]), leading to a small decrease of  $\text{PM}_{2.5}$  by only 8 percent compared with the 20km\_D2 run in the cold season. In the warm season,  $\text{PM}_{2.5\_dust}$  in the 20km\_P7 run is overestimated by a factor of five, causing an overestimation of  $\text{PM}_{2.5}$  and  $\text{PM}_{10}$  (Figure 13[a] and [b]). Aerosol extinctions in the boundary layer above the surface increase in the warm season (Figure 14 [c] and [d]), possibly related to overestimation of dust emissions and more conducive convective vertical transport in the PBL scheme.

**Figure 13: Aerosol Mass ( $\mu\text{g m}^{-3}$ ) for Different Species from OBS, the 4km\_D2, 20km\_D2 and 20km\_P7 Simulations**



Source: University of California, Riverside

Figure 14: Vertical Distribution of Seasonal Mean 532 nm Aerosol Extinction Coefficient (km<sup>-1</sup>)



Source: University of California, Riverside

In summary, the WRF-Chem model captures the seasonal variations of meteorological variables (temperature, RH, wind speed and precipitation), despite some deviations in magnitude. The low biases in aerosol optical properties of the warm season likely do not originate from hygroscopic effects, wet removal processes or dust emissions associated with the wind speed bias. The model simulates a stable environment in the warm season, which is opposite to the observed unstable environment. The simulated stable environment may be most likely responsible for low biases in the aerosol extinction above the surface (0.3-3 km) and the column-integrated AOD in the warm season. Switching to the ACM2 PBL scheme leads to improved vertical displacement of aerosols in the boundary layer, thus an improvement in the simulations of NO<sub>3</sub> and NH<sub>4</sub> in the cold season. However, dust emissions are significantly overestimated with the ACM2 PBL scheme, which contributes partly to the better simulation of aerosol extinction in the boundary layer and AOD in the column. These results highlight that improving the simulation of boundary layer structure and processes are critical for capturing the vertical profiles of aerosol extinction.

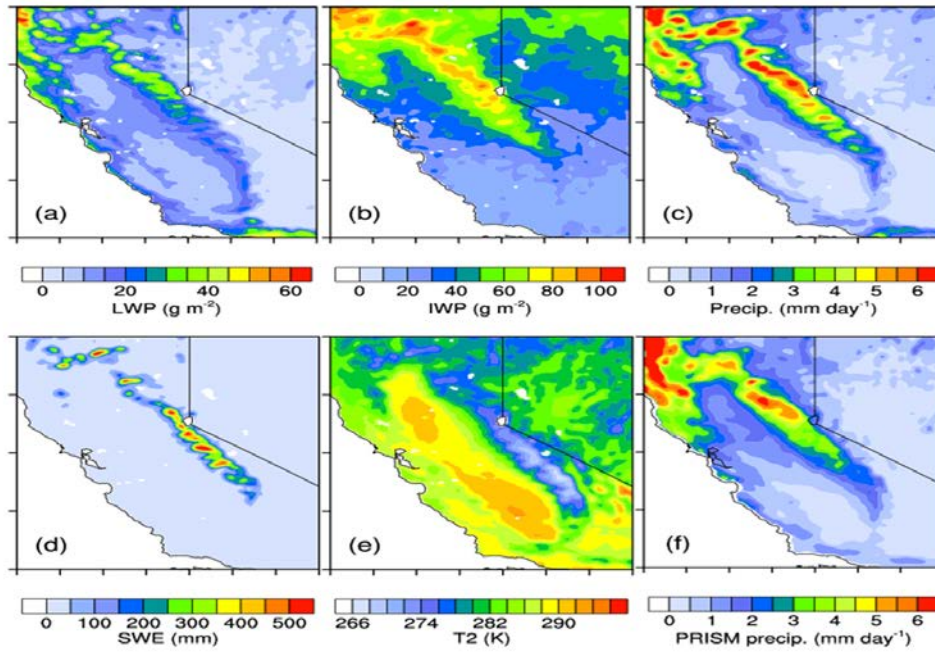
## 1.5 Impacts of Aerosols on Precipitation and Snowpack in California

### 1.5.1 Validation of Model Results

Since the researchers' focus is on the changes in precipitation and snowpack due to aerosol effects, the spatial distribution of averaged results over the period from October 2012 to June 2013 when snow normally presents over the Sierra Nevada are first shown. Figure 15 illustrates a few important and relevant variables that the model simulates in the CTRL experiment, including liquid water path (LWP), ice water path (IWP), precipitation, snow water equivalent (SWE), and temperature at two meters (T2) above the ground. SWE is a common snowpack measurement. It is the amount of water contained within the snowpack and can be regarded as the depth of water over unit flat surface that would theoretically result if the entire snowpack melted instantaneously. Here, the model simulated SWE is the mean value of the accumulated SWE from 3-hourly model outputs. It is shown that clouds (Figure 15[a] and [b]), precipitation (Figure 1 [c]), snowpack (Figure 15[d]), and surface runoff mostly occur over the Sierra Nevada and Klamath Mountains in northern California. For temperature (Figure 15[e]), the central valley area appears to be relatively warm with two maxima over the northern and southern part of the central valley, respectively, while colder temperatures are found over the mountain ranges. The model-simulated precipitation is compared with corresponding observations from the Parameter elevation Regression on Independent Slopes Model (PRISM, 2004) gridded data product at 4 km resolution (Figure 15[f]). Compared to the PRISM observations, the model successfully captures the precipitation pattern, including the locations of the major precipitation centers, but slightly overestimates the magnitude over the Sierra Nevada.

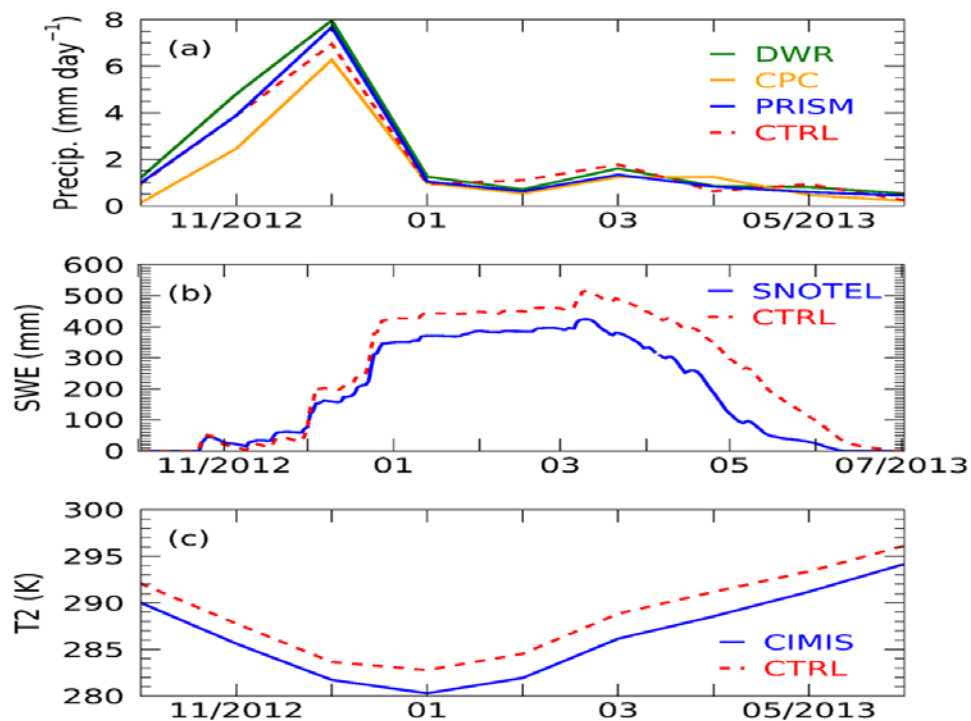
To validate the simulated seasonal variations, the monthly mean model simulated precipitation and T2 are compared with observations (Figure 16[a] and [c]). Model data are sampled onto observational sites before the comparison is conducted. For precipitation observations, besides the PRISM product, the researchers also employ the Climate Prediction Center (CPC) Unified Gauge-Based Analysis of Daily Precipitation product (Chen et al., 2008) at  $0.25^\circ \times 0.25^\circ$  resolution and the gauge measurements from Department of Water Resources (DWR). Observed air temperature is obtained from the California Irrigation Management Information System (Snyder, 1984). For SWE, daily accumulated SWE simulations are compared with measurements collected at Snow Telemetry (SNOTEL) stations. SNOTEL SWE is measured using a snow pillow sensor and biases in SWE measurement could occur when temperature differences between surrounding ground cover and the pillow sensor create uneven distribution of snow (Meyer et al., 2012). Both under- and over-estimation could happen depending on the snowmelt conditions and the snow density rate of change (Serreze et al., 1999; Serreze et al., 2001; Johnson and Marks, 2004).

Figure 15: Model Simulated (a) LWP ( $\text{g m}^{-2}$ ), (b) IWP ( $\text{g m}^{-2}$ ), (c) Precipitation ( $\text{mm day}^{-1}$ ), (d) SWE (mm), and (e) Temperature at 2 Meters, T2 (K) From the CTRL Simulation, and (f) PRISM Observed Precipitation ( $\text{mm day}^{-1}$ ), Averaged Over October 2012 to June 2013



Source: University of California, Riverside

Figure 16: Monthly Mean Precipitation, T2, and SWE



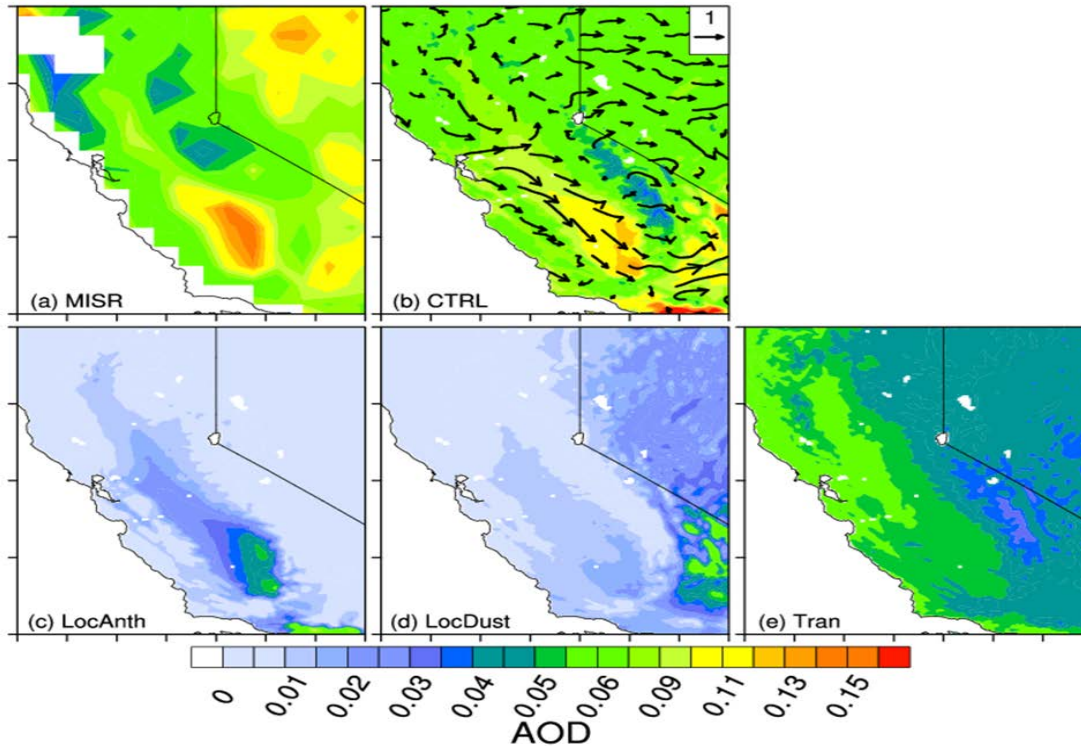
Source: University of California, Riverside

It is shown that the model captures the maximum precipitation in December, with the magnitude falling between the observations from CPC and PRISM/DWR during winter, which is the major rainy season in California (Figure 16[a]). In the relative dry months from February to June, the simulated precipitation has similar magnitude to the observations, with slightly overestimation or underestimation in different months. For SWE, the model simulations represent seasonal variations of SWE with the maximum between March and April (Figure 16[b]), but the model overestimates SWE amount comparing to SNOTEL. While the model overestimates the surface temperature in magnitude, it captures the seasonal variations well, including the highest/lowest temperature in July/January, respectively (Figure 16[c]).

The simulated aerosols over California using this model have been validated extensively in Wu et al. (2017) and in Section 1.4 by comparing to observations, such as MISR (Multiangle Imaging Spectroradiometer) and AERONET (Aerosol Robotic Network) AOD, CALIPSO (Cloud-Aerosol Lidar and Infrared pathfinder Satellite Observation) aerosol extinction, IMPROVE (Interagency Monitoring of Protected Visual Environments) and EPA CSN (National Chemical Speciation Network operated by Environmental Protection Agency) aerosol speciation.

Here, The researchers present the distributions of AOD averaged over October 2012 to June 2013 for the MISR (Diner et al., 1998) observation and all aerosols in the CTRL simulation, together with locally emitted aerosols and those transported from outside the model domain, derived from the difference between the CTRL simulation and the corresponding experiment (NoLocAnth, NoLocDust and NoTran), respectively, to facilitate the understanding of the aerosol effects in different regions and from different sources (Figure 17). It is shown that the model simulation well captures the spatial distribution of AOD in California, including the maximum over the southern part of the valley area and larger AODs over the lower lands to the southeast of the Sierra Nevada (Figure 17[a] and [b]). Note that the smoother contour in MISR is due to the coarser horizontal resolution ( $0.5^\circ$ ) of the MISR data. The distribution of the locally emitted anthropogenic aerosols (Figure 17[c]), which are mostly located over the central valley associated with the emissions from local industries and farms, presents a similar pattern to the total AOD and substantially contributes to the maxima AOD over the region. Local dust aerosols mainly reside over the lower lands to the southeast of the Sierra Nevada while substantial amounts are also seen over the central valley (Figure 17[d]). Transported aerosols are carried into the domain by atmospheric circulation and widely distributed, with more over the central valley due to the trapping of aerosols by the surrounding mountains (Figure 17[e]).

**Figure 17: Spatial Distribution of Aerosol Optical Depth (AOD) Averaged Over October 2012 to June 2013**



Source: University of California, Riverside

Overall, the WRF-Chem model that the researchers employ in this study is a reliable tool for examining the impact of aerosols on the seasonal variations of precipitation and snowpack in California, especially over the Sierra Nevada.

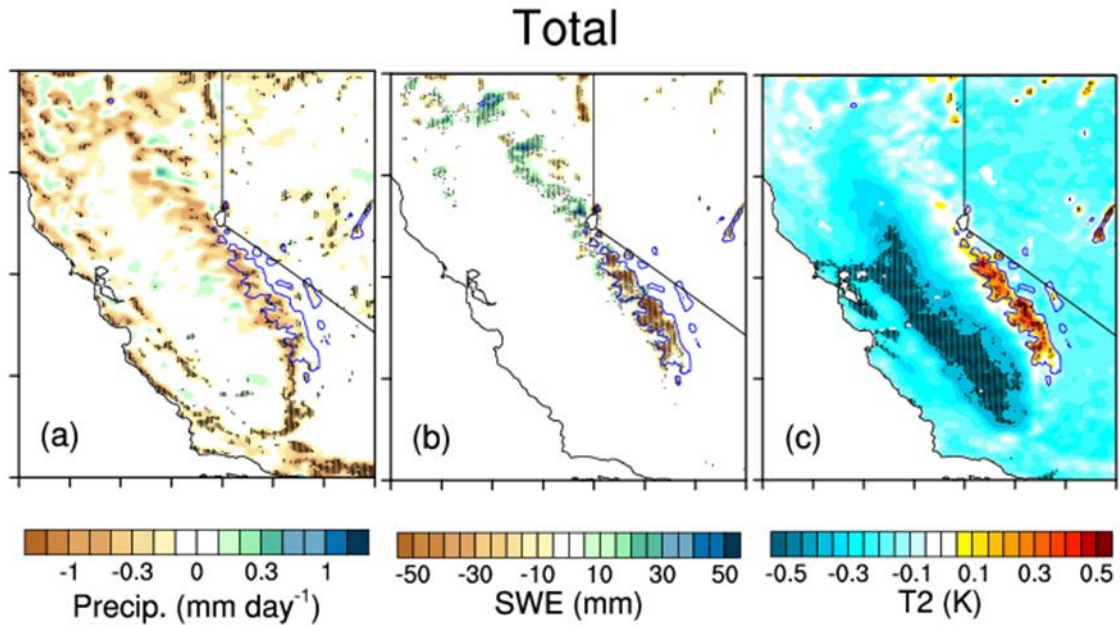
### 1.5.2 Aerosol Effects on Precipitation and Snowpack

The overall aerosol effects, from all aerosol types and sources (including locally emitted and transported) through the three pathways (ARI, ASI, and ACI), can be examined from the differences between the experiments CTRL and CLEAN. The two-tailed Student's t test, in which deviations of the estimated parameter in either direction are considered theoretically possible, is applied to the 3-hourly data for each experiment in this study to measure the statistical significance of the simulations. Figure 5 shows the differences averaged over October 2012 to June 2013 in precipitation, SWE, and T2, where the dots represent differences of the 3-hourly data being statistically significant at above 90 percent level. Due to the aerosol effects, temperature decreases over the central valley, where most aerosols are located, while significant warming occurs over the mountain tops (Figure 18[c]). Precipitation decreases over the Sierra Nevada (Figure 18[a]), consequently leading to decreased SWE (Figure 18[b]).

To understand how the aerosols affect these important variables, the researchers examine the effects of ARI, ASI, and ACI separately. In the following figures (Figure 19 to Figure 25), the differences are statistically significant at 70 percent level. It is seen that

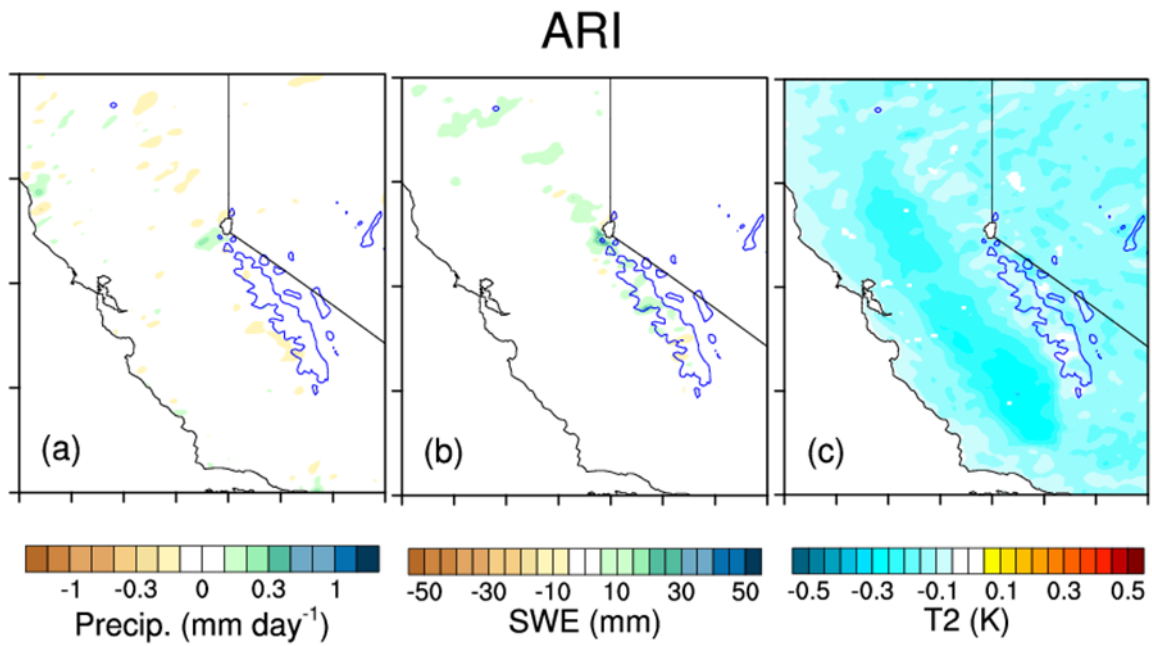
the major effect of ARI is to decrease the surface temperature over the whole domain through the scattering and absorption of solar radiation, with the maxima over the central valley where the aerosols are mostly located, contributing to the surface cooling caused by the total aerosols effects in that region (Figure 19[c]). The ARI induced surface cooling over the Sierra Nevada, although not as strong as over the central valley, leads to reduced snowmelt and hence slight increase in SWE, opposite to the overall aerosol effect on SWE (Figure 19[b]). The effect of ARI on rainfall is not very significant (Figure 19[a]). The main effect of ASI is to increase the temperature (Figure 20[c]) over the snowy area of the Sierra Nevada through the reduction of snow albedo (Figure 20[d]) and hence more absorption of solar radiation at the surface, contributing to the reduced SWE over the Sierra Nevada (Figure 20[b]). The effect of ASI on precipitation is also minimal.

**Figure 18: Total Aerosol Effects (CTRL – CLEAN) on Spatial Distribution of Precipitation (mm day<sup>-1</sup>), SWE (mm), and T2 (K)**



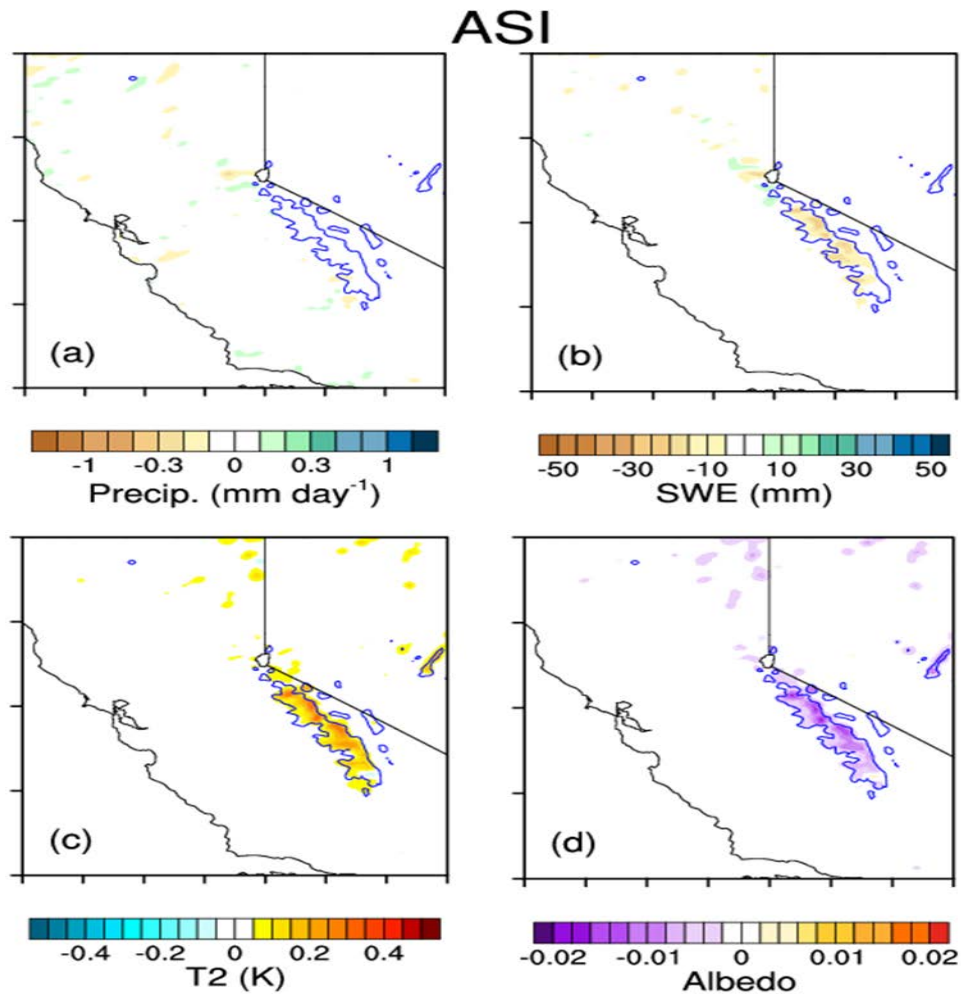
Source: University of California, Riverside

Figure 19: ARI effects (CTRL – NARI) on Spatial Distribution of Precipitation (mm day-1), SWE (mm), and T2 (K)



Source: University of California, Riverside

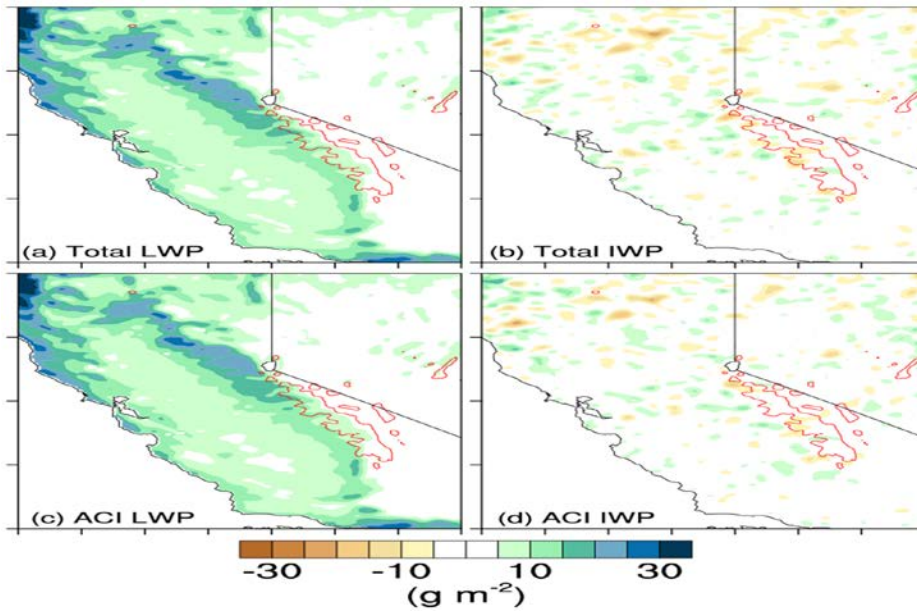
**Figure 20: ASI Effects (CTRL – NASI) on Spatial Distribution of Precipitation (mm day<sup>-1</sup>), SWE (mm), T2 (K), and Surface Albedo**



Source: University of California, Riverside

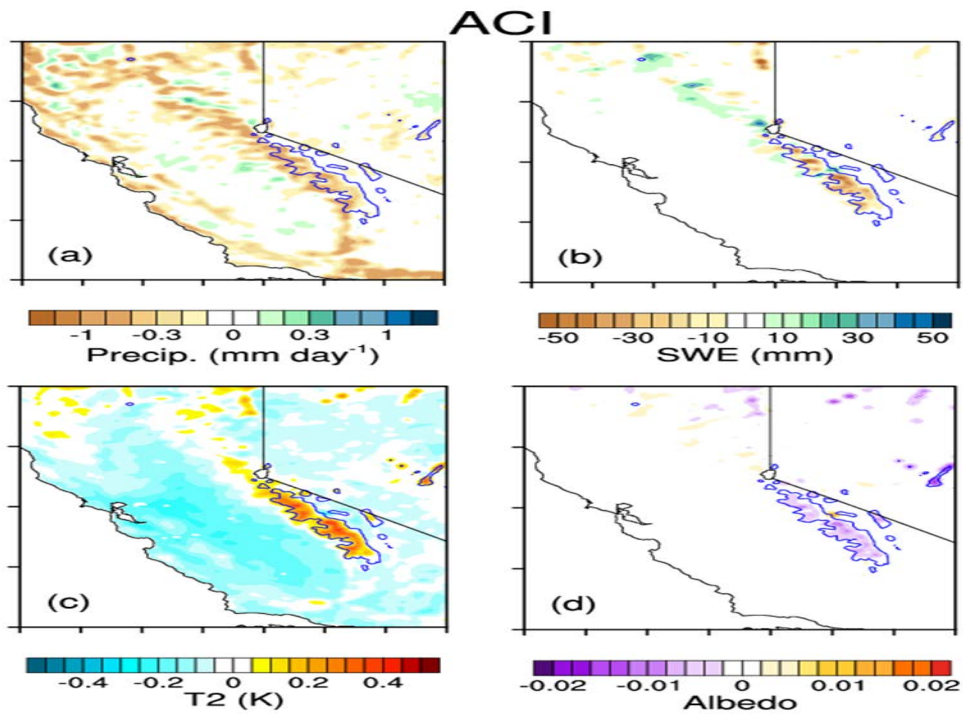
Figure 21 shows the effect of aerosols on clouds through ACI. When more aerosols are present in the atmosphere, more CCN are available for the formation of clouds with smaller cloud droplets. As a result, more non-precipitating clouds are produced when aerosol are included in the model. The enhanced LWP (Figure 21[a]) is primarily produced by the ACI effect (Figure 21[c]). There are no significant changes in IWP (including ice, snow, and graupel) because the aerosol effect on ice cloud formation is not explicitly treated in the model. The ACI effect leads to reduced precipitation and less SWE over the mountains (Figures 22[a] and [b]). Temperature decreases over the valley due to more clouds formed associated with the ACI effect. The increase in temperature over the mountain areas (Figure 22[c]) is caused by the reduced snow amount, which results in weaker surface albedo (Figure 22[d]) and enhanced solar absorption at the surface and overwhelms the decrease of temperature, which may be caused by increased clouds.

Figure 21: Differences in LWP (g m<sup>-2</sup>), IWP (g m<sup>-2</sup>), (CTRL – CLEAN), LWP (g m<sup>-2</sup>), IWP (g m<sup>-2</sup>), and (NARS – CLEAN)



Source: University of California, Riverside

Figure 22: Differences in ACI Effects



Source: University of California, Riverside

Overall, aerosols affect surface temperature, precipitation, and snowpack in California through the three pathways. ACI plays a dominant role in increasing cloud water but reducing precipitation, leading to reduced SWE and surface runoff over the Sierra Nevada. ASI also reduces SWE due to the smaller snow albedo associated with dirty snow, leading to more surface absorption and snowmelt. ARI, on the other hand, slightly increases SWE through the cooling of the surface. For surface temperature, ARI and ACI contribute together to the cooling of the valley area, while ACI and ASI significantly warm the surface over the mountaintops. Note that for the ASI effect, warming of the snow cover area through aerosol induced snow-albedo feedback is the cause for the reduced SWE. For the ACI effect, however, warming over the mountain region is a result from the reduced SWE, which can also induce snow-albedo feedback and result in smaller surface albedo and more surface absorption of solar radiation.

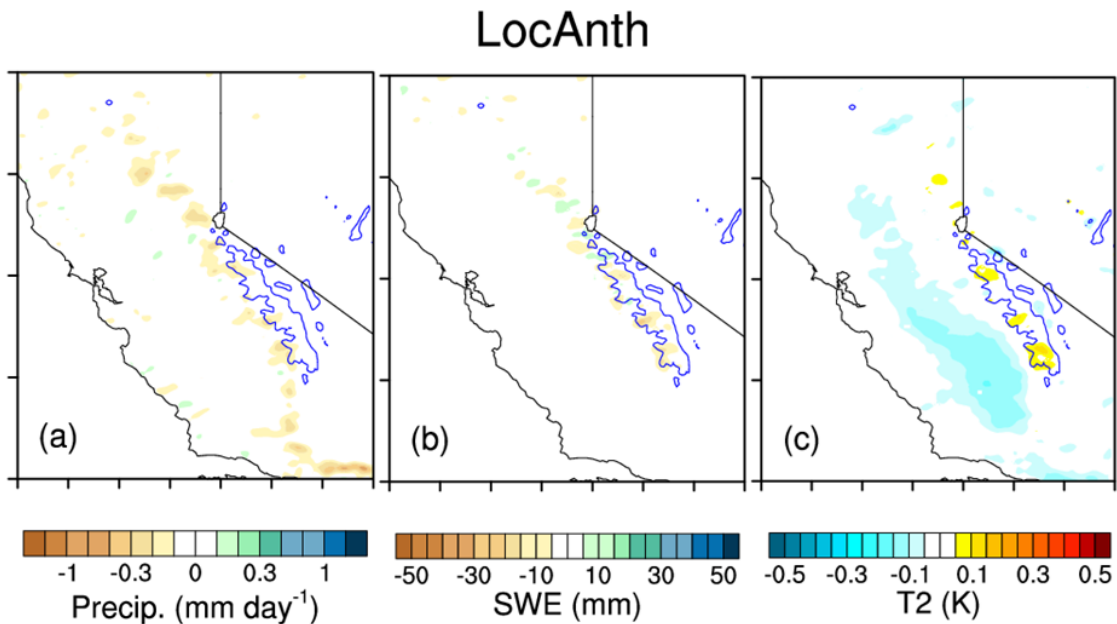
Next, the researchers examine the roles of local anthropogenic aerosols and local dust as well as transported aerosols. The effect of local anthropogenic aerosols can be discovered from the differences between CTRL and NoLocAnth. It is shown that local anthropogenic aerosols slightly suppress precipitation (Figure 23[a]) via ACI, leading to a reduced SWE (Figure 23[b]) and a warming over the mountain tops (Figure 23[c]). The cooling of the valley area, where locally emitted anthropogenic aerosols are mostly located, is associated with the ARI effect and more non-precipitating clouds produced through ACI. Dust aerosols emitted from local sources mainly warm the surface through the reduction of snow albedo (ASI, Figure 24[c]), consequently enhancing the snowmelt and leading to the reduced SWE (Figure 24[b]). Local dust aerosols have no significant effect on precipitation (Figure 24[a]).

Note that the effects of local anthropogenic and dust aerosols do not seem to be able to explain the total effects of aerosols, raising the question whether the transported aerosols play an important role in the precipitation and snowpack over the Sierra Nevada. Figure 25 illustrates the impact of aerosols transported from outside the model domain. It is shown that transported aerosols reduce the precipitation through ACI (Figure 25[a]), which exceeds the ARI effect and leads to decreased SWE and increased temperature over the southern part of the Sierra Nevada (Figure 25[b] and [c]). Over the central valley, as well as over the northern part of the Sierra Nevada, temperature decreases (Figure 25[c]) due to the relatively larger ARI effect of the transported aerosols compared to the ACI effect, resulting in less snowmelt and increased SWE over that region (Figure 25[b]).

The overall changes induced by aerosols for surface temperature (K) and precipitation, SWE, and surface runoff in percentage averaged over October to June are given in Table 6 for the whole domain (34-42 °N, 117-124 °W, not including ocean points), mountain tops (elevation  $\geq 2.5$  km), and lower elevations (elevation  $< 2.5$  km). For the whole domain in year 2012-2013, temperature is cooled by 0.19 K due to aerosol ARI (-0.14 K), as well as ACI ( $\sim 0.06$  K) mainly associated with transported aerosols (-0.17 K),

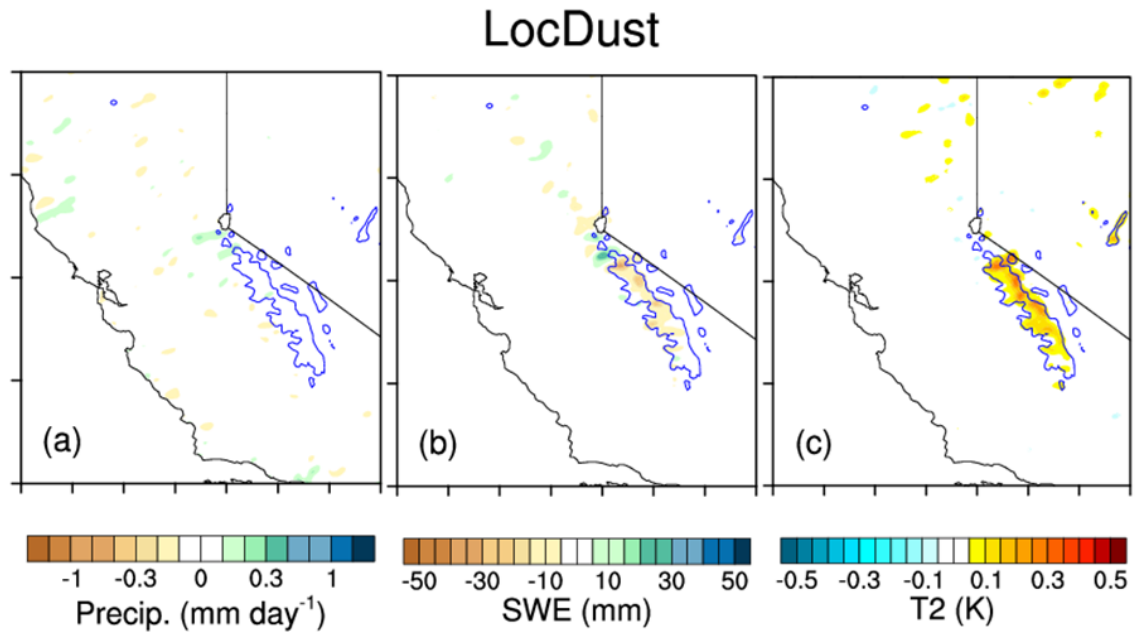
accompanied by reduction in precipitation, SWE, and surface runoff of about 7 percent, 3 percent, and 7 percent, respectively. Reduction in precipitation is mainly caused by ACI (-6.26 percent) associated with transported (-2.97 percent) and local anthropogenic (-1.02 percent) aerosols. For SWE, reduction is attributed to ACI (-2.67 percent) and ASI (-1.96 percent), while ARI contributes to an increase (1.88 percent). Surface runoff is defined as water from precipitation, snowmelt, or other sources that flows over the land surface, and is a major component of the hydrological cycle. Overall changes in surface runoff are similar to those in precipitation, accompanied by contributions from changes in snowmelt. For the mountaintops, warming of 0.22 K is found attributed to ASI (0.12 K) and ACI (0.17 K) associated with local dust and anthropogenic aerosols, respectively, with 10 percent or more reduction in precipitation, snowpack, and surface runoff. Therefore, aerosols may contribute to California drought through both the warming of mountaintops and anomalously low precipitation over the whole area. For the lower elevations, the domain-averaged changes are similar to those for the whole domain, except for SWE, which slightly increases by 0.42 percent due to ARI (2.43 percent) with main contribution from transported aerosols (4.01 percent).

**Figure 23: Effect of Local Anthropogenic Aerosols on Spatial Distribution**



Source: University of California, Riverside

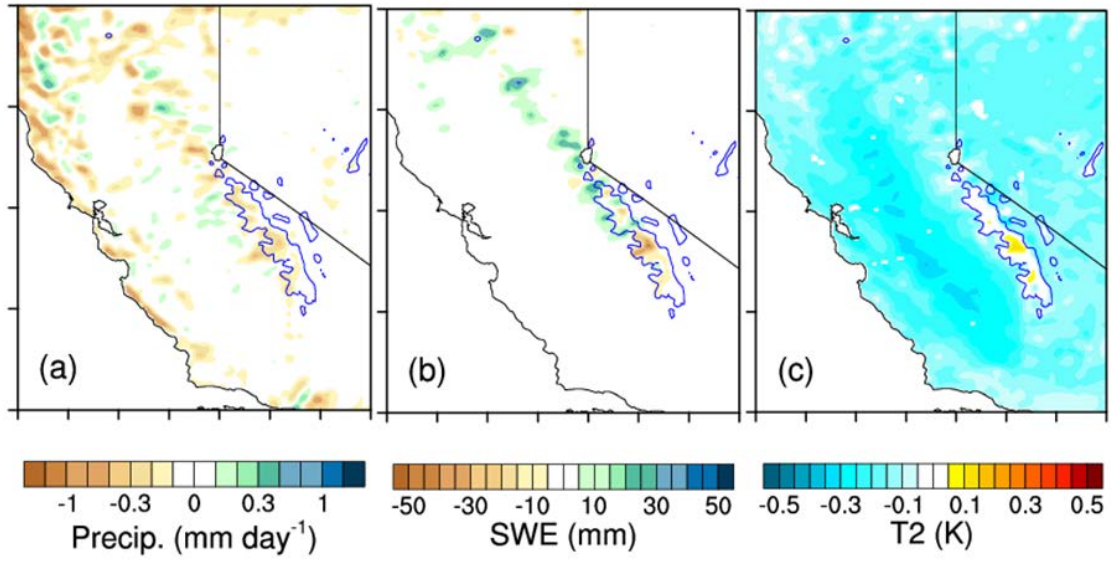
Figure 24: Effect of Local Anthropogenic Aerosols on Dust Aerosols



Source: University of California, Riverside

Figure 25: Effect of Local Anthropogenic Aerosols on Transported Aerosols

# Tran



Source: University of California, Riverside

**Table 6: Changes in Surface Temperature (K) and Precipitation, SWE, and Surface Runoff in Percentage Averaged Over October 2012 to June 2013**

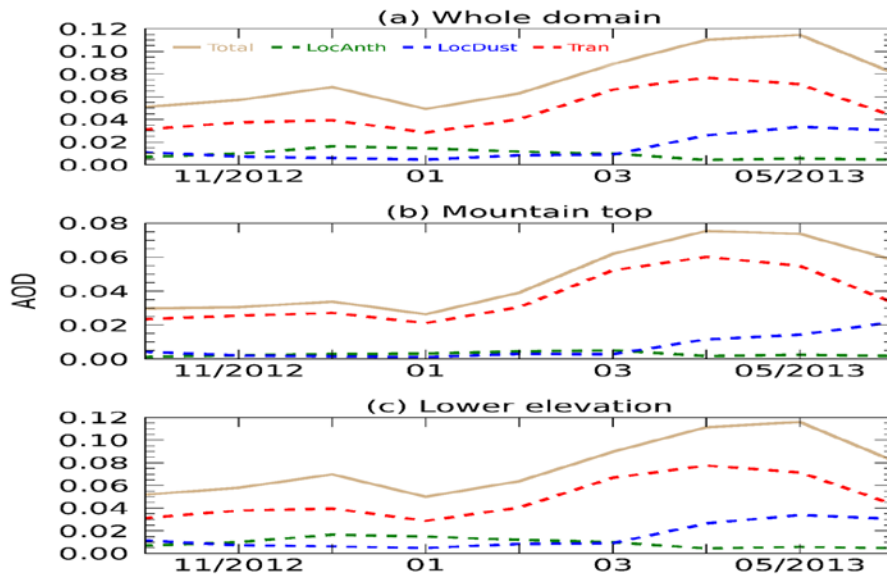
Region	Source/pathway	T2 (K)	Precipitation (%)	SWE (%)	Surface runoff (%)
Whole Domain	Total	-0.19	-6.87	-3.17	-6.58
	ARI	-0.14	-0.47	1.88	-0.21
	ASI	0.01	-0.03	-1.96	0.04
	ACI	-0.06	-6.26	-2.67	-6.30
	LocAnth	-0.02	-1.02	-0.91	-0.94
	LocDust	0.00	-0.19	-1.35	0.01
	Tran	-0.17	-2.97	1.89	-2.90
Mountain Tops	Total	0.22	-11.53	-10.50	-9.58
	ARI	-0.09	-0.61	0.76	-0.49
	ASI	0.12	0.26	-3.94	1.10
	ACI	0.17	-11.03	-7.57	-10.25
	LocAnth	0.03	-1.75	-1.60	-2.06
	LocDust	0.10	0.31	-2.99	1.49
	Tran	-0.02	-5.25	-2.43	-4.76
Lower Elevations	Total	-0.21	-6.62	0.42	-6.42
	ARI	-0.14	-0.46	2.43	-0.19
	ASI	0.00	-0.04	-0.99	-0.01
	ACI	-0.07	-6.00	-0.27	-6.09
	LocAnth	-0.03	-0.98	-0.57	-0.89
	LocDust	0.00	-0.22	-0.55	-0.07
	Tran	-0.17	-2.85	4.01	-2.81

Source: University of California, Riverside

### 1.5.3 Seasonal Variations of Aerosol Effects

Figure 26 depicts the monthly mean AOD for total aerosols (brown solid), local anthropogenic aerosols (green dashed), local dust (blue dashed), and transported aerosols (red dashed) averaged over the whole domain, mountaintops, and lower elevation area from October 2012 to June 2013. It is seen that transported aerosols contribute to about two-thirds of the total AOD. The total AOD has two maxima, one in December and one in May, mainly associated with the seasonal variations of transported aerosols and local dust aerosols. Local dust AOD starts to increase in March and reaches a maximum around May, while transported aerosol AOD peaks in April (Figure 26[a]). The seasonal variations of AOD over the mountaintops and lower elevations are similar to those of the whole domain (Figures 26[b] and [c]).

**Figure 26: Monthly Mean AOD Simulated from CTRL for Total Aerosols, Local Anthropogenic Aerosols, Local Dust, and Transported Aerosols**

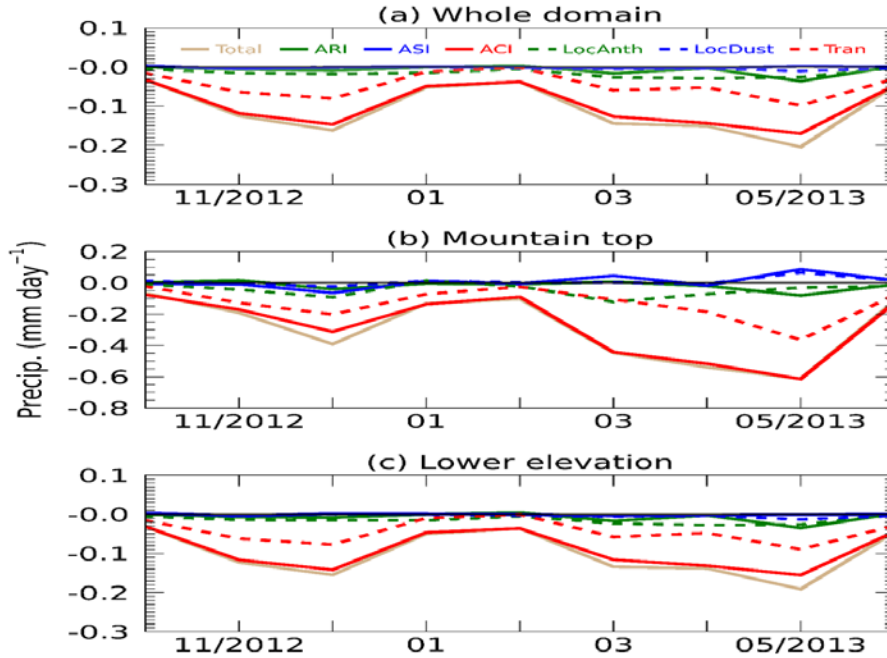


Source: University of California, Riverside

The monthly mean differences in precipitation due to the total aerosols (brown solid), ARI (green solid), ASI (blue solid), ACI (red solid), local anthropogenic aerosols (green dashed), local dust (blue dashed), and transported aerosols (red dashed) are shown in Figure 27. Reduced precipitation is seen over the whole domain, with the most contribution from transported aerosols, followed by local anthropogenic aerosols, both of which play roles in precipitation changes through ACI as previously shown. ARI, ASI, or locally emitted dust aerosols do not seem to play an important role in the monthly mean precipitation changes (Figure 27[a]). Two maxima of aerosol effects are found: one in December when it is the rainy season of the California and at the same time relatively larger AOD presents over this region (Figure 26[a]); the other peak reduction in precipitation due to the aerosol effects is found in May with a value of about 0.2 mm day<sup>-1</sup> (Figure 27[a]), probably associated with the maximum aerosols (Figure 26[a]) and

also the orographic precipitation over the mountain region during that time period (Lee et al., 2015). Given that the monthly mean precipitation in May is only about 1 mm day<sup>-1</sup>, the reduction caused by aerosols is about 20 percent. For monthly mean precipitation, changes over the mountaintops and the lower elevation area, respectively, have similar seasonal variation patterns (Figure-27[b] and [c]).

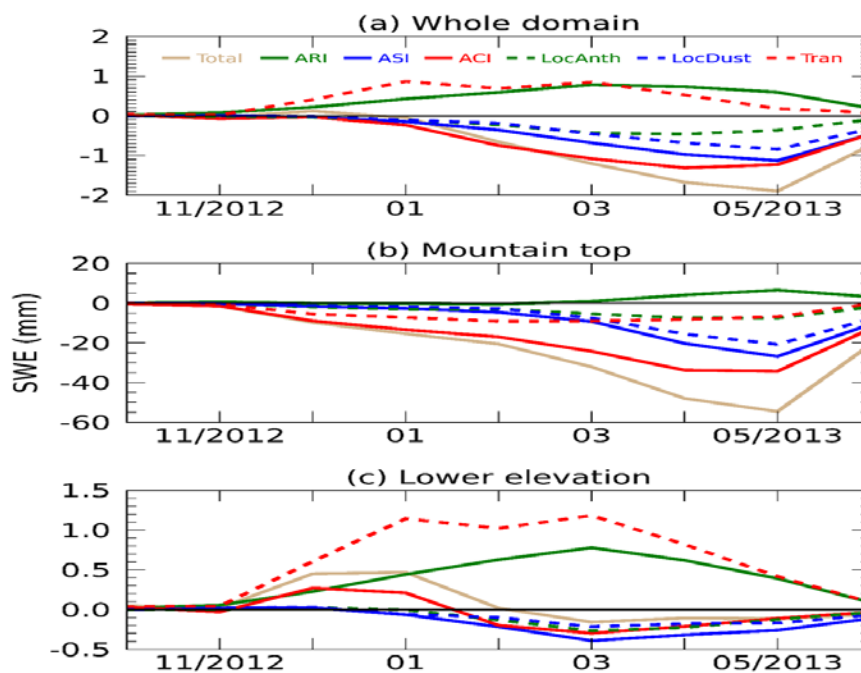
**Figure 27: Monthly Mean Differences in Precipitation (mm day<sup>-1</sup>)**



Source: University of California, Riverside

For SWE, however, changes over the mountaintops are different from those in the lower area (Figure 28). For mountaintops, negative changes in SWE are seen over the whole period, with a maximum reduction of about 60 mm in May corresponding to the maximum AOD (Figure 28[b]). Major contribution is from local dust aerosols through ASI, as well as transported and local anthropogenic aerosols through ACI. ARI produces small positive changes (~ 5 mm in May) in SWE due to the scattering and absorption of solar radiation by aerosols which leads to surface cooling. For lower elevation area, slightly enhanced SWE is found during the winter time, associated with the effects of transported aerosols that produce more clouds through ACI, and together with the ARI effect, lead to the cooling of the surface and hence less snowmelt (Figure 28[c]). Over the whole domain, SWE is reduced with a maximum of about 2 mm in May, equivalent to about 2 percent reduction, mainly attributed to the local dust particles through ASI, and local anthropogenic and transported aerosols through ACI (Figure 28[a]).

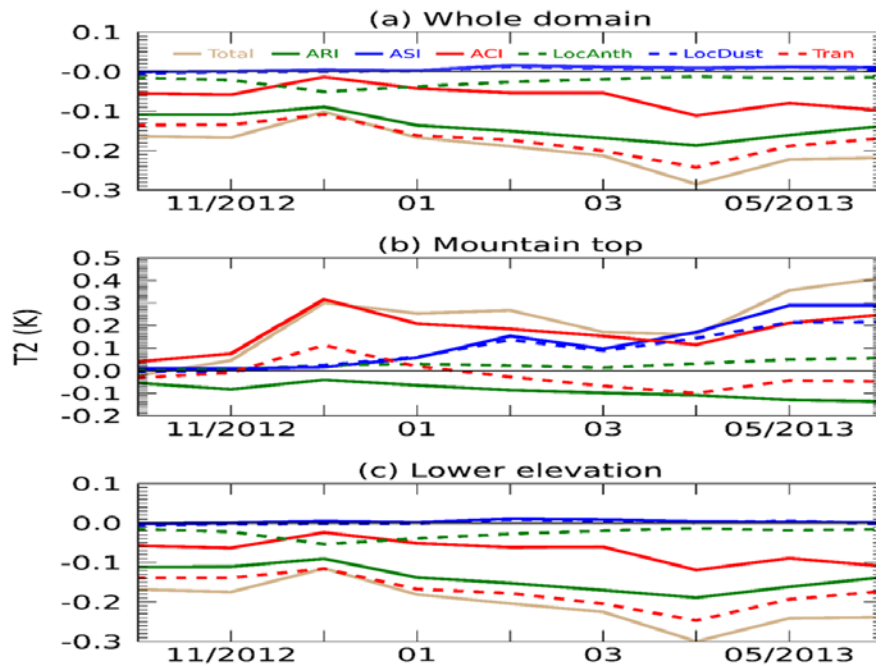
**Figure 28: Monthly Mean Differences in SWE (mm)**



Source: University of California, Riverside

Changes in temperature also exhibit different patterns over the mountaintops and the lower elevations (Figure 29). Warming over the mountaintops is produced by dust aerosols through ASI with a maximum around May, and by transported aerosols through ACI during winter, which leads to reduced precipitation and SWE with a maximum in January (Figure 29[b]). Cooling over the lower elevation areas is caused by ARI, and is induced by more clouds generated in the model simulations due to transported aerosols through ACI, with a maximum cooling of about 0.3 K in April, corresponding to the maximum AOD of transported aerosols (Figure 29[c]). The average temperature changes over the whole domain are negative because of the large area of the lower elevations (Figure 29[a]).

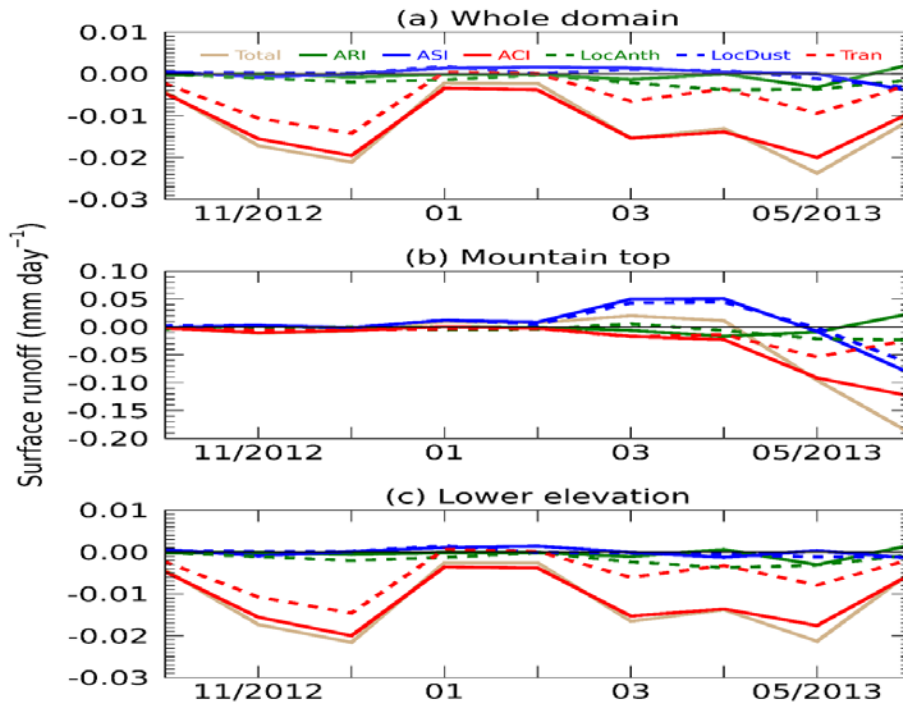
**Figure 29: Monthly Mean Differences in T2 (K)**



Source: University of California, Riverside

Surface runoff reaches a maximum in December for the lower elevations and the whole domain, but a peak value in May for mountaintops when the temperature is warmer. For lower elevations where there is not much snow, surface runoff is mainly associated with precipitation and the changes present a similar pattern to those in precipitation (Figure30[c]). Changes in surface runoff for the whole area present similar patterns to those of the lower elevations because of the larger area of lower elevations (Figure 30[a]). However, for mountaintops, changes in surface runoff are also associated with changes in snowmelt. Surface runoff over the mountaintops shows a slight increase in spring, and then a decrease after April (Figure-30[b]). The increase can be explained by the effect of local dust aerosols deposited on the snow, which reduces the snow albedo through ASI and warms the surface, leading to more and earlier snowmelt than normal, consistent with negative changes in SWE. The decrease after April is a combined effect of less snowpack available for melting caused by earlier snowmelt due to local dust aerosols and reduced precipitation caused by transported and local anthropogenic aerosols through ACI. Thus, the impact of aerosols is to speed up snowmelt at the mountaintops in spring and modify the seasonal cycle of surface runoff.

**Figure 30: Monthly Mean Differences in Surface Runoff (mm day<sup>-1</sup>)**



Source: University of California, Riverside

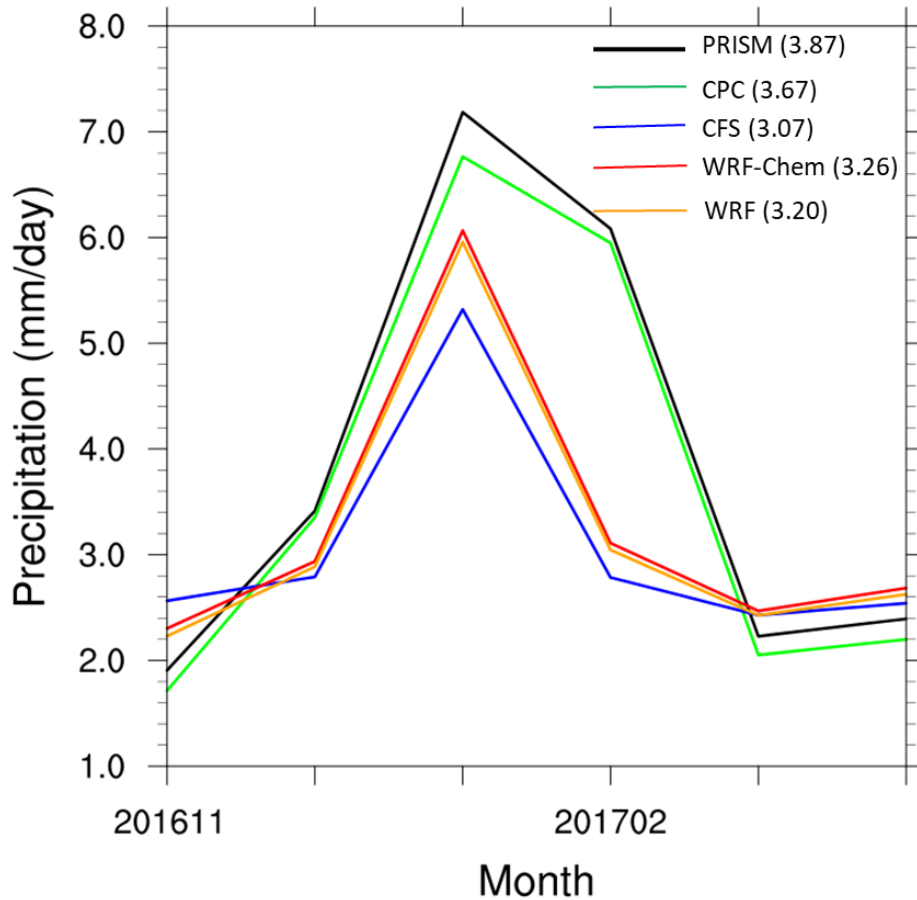
## 1.6 Seasonal Forecast for California

The researchers have run 10 downscaling WRF and WRF-Chem simulations, respectively, to do 6-month forecast for November 2016 to April 2017 over California using different initial and boundary conditions obtained from global forecast data from NCEP Coupled Forecast System Model Version 2 (CFS). Figure 31 shows the monthly mean precipitation from the model ensemble results (CFS and WRF-Chem & WRF) and observations from PRISM and CPC. It shows that CFS and WRF models capture the seasonal variations with peak in January, although they underestimate the precipitation during December 2016 – February 2017. The maximum underestimates occur in February 2017, and the underestimates in WRF-Chem and WRF are closely associated with the low biases in the large-scale CFS model. In terms of 6-month averages (the values in the brackets), WRF-Chem improves the forecast by about 5 percent as compared to CFS, and is also better than the result by WRF.

Figure 32 shows the precipitation observations from CPC and PRISM, model ensemble prediction results from CFSV2, WRF-Chem, and WRF, and the differences between WRF-Chem and WRF, for January 2017. Compared to observations (Figures 32[a] and [b]), CFS model obviously missed the strong precipitation band along the Sierra Nevada, and only simulated the precipitation center over the coastal area of northern California. WRF and WRF-Chem predictions, however, well captured the precipitation pattern and magnitude (Figures 32[d] and [e]) over the entire California for January 2017, which illustrates the importance and improvement of dynamical downscaling approach in the regional

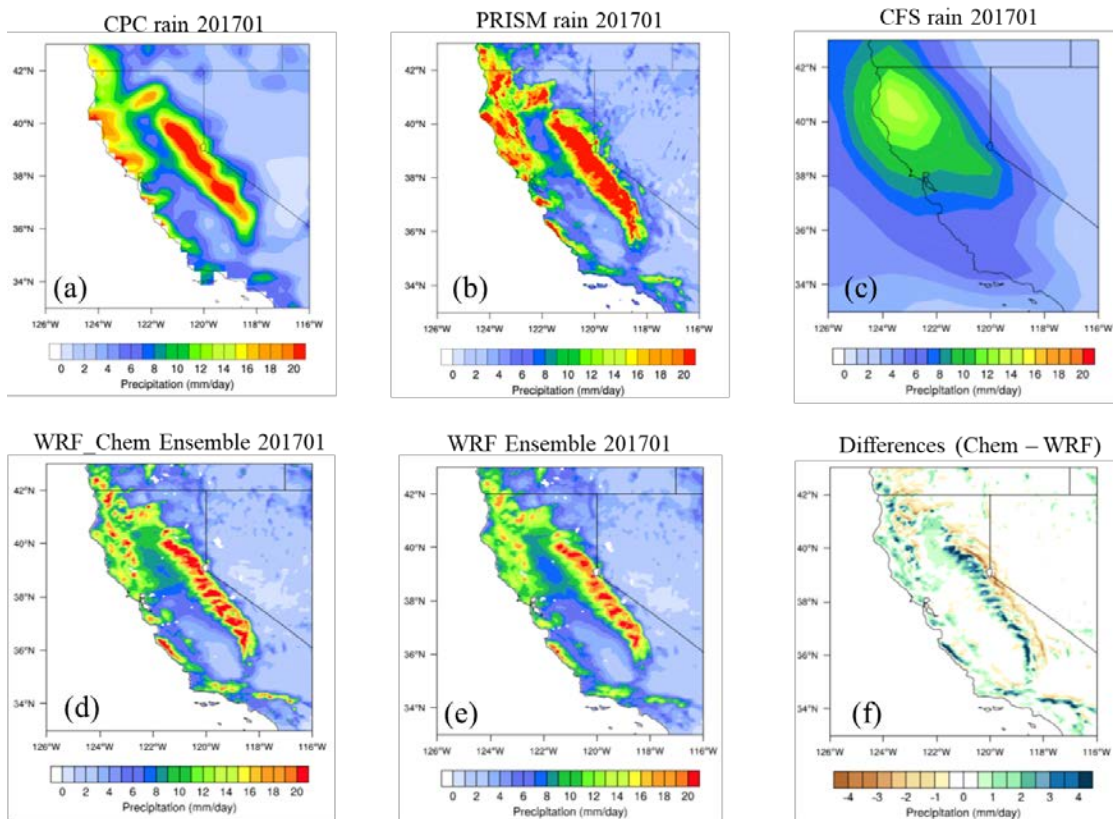
forecast. It can also be seen that the simulations with aerosols included produced noticeable differences in the spatial distribution of precipitation (Figures 32[d]-[f]). More precipitation is found over the Sierra Nevada when aerosol effects are considered in the forecast, which, to some extent, corrects the underestimate of precipitation in WRF results.

**Figure 31: Monthly Mean Precipitation During November 2016 to April 2017**



Source: University of California, Riverside

**Figure 32: Precipitation Observations for January 2017**



Source: University of California, Riverside

## 1.7 Summary and Conclusion

The research team employed a version of the WRF-Chem model with fully coupled aerosol-meteorology-snowpack to investigate the aerosol seasonal variability and the impacts of various aerosol sources on precipitation and snowpack in California. The team evaluated model simulations of aerosol seasonal variability in the San Joaquin Valley (SJV), California by satellite and in-situ observations. Results show that the WRF-Chem model successfully captures the distribution, magnitude, and variation of SJV aerosols during the cold season. However, aerosols are not well represented in the warm season. Aerosol simulations in urban areas during the cold season are sensitive to model horizontal resolution, with better simulations at 4 km resolution than at 20 km resolution, mainly due to inhomogeneous distribution of anthropogenic emissions and better represented precipitation in the 4 km simulation. In rural areas, the model sensitivity to grid size is rather small. The researchers' observational analysis reveals that dust is a primary contributor to aerosols in the SJV, especially during the warm season. Aerosol simulations in the warm season are sensitive to parameterization of dust emission in WRF-Chem. The GOCART (Goddard Global Ozone Chemistry Aerosol Radiation and Transport) dust scheme produces very little dust in the SJV while the DUSTRAN (DUST TRANsport model) scheme overestimates dust emission. Vertical

mixing of aerosols is not adequately represented in the model based on CALIPSO (Cloud-Aerosol Lidar and Infrared pathfinder Satellite Observation) aerosol extinction profiles. Improved representation of dust emission and vertical mixing in the boundary layer are needed for better simulations of aerosols during the warm season in the SJV.

The relative roles of locally emitted anthropogenic and dust aerosols, and aerosols originating from outside the model domain are differentiated through the three pathways, aerosol-radiation interaction (ARI), aerosol-snow interaction (ASI), and aerosol-cloud interaction (ACI). The convection-permitting model simulations show that precipitation, snow water equivalent (SWE), and surface air temperature averaged over the whole domain (34-42 °N, 117-124 °W, not including ocean points) are reduced when aerosols are included, therefore reducing large biases of these variables due to the absence of aerosol effects in the model. Aerosols affect California water resources through the warming of mountaintops and the reduction of precipitation; however, different aerosol sources play different roles in changing surface temperature, precipitation and snowpack in California by means of various weights of the three pathways. ARI by all aerosols mainly cools the surface, leading to slightly increased SWE over the mountains. Locally emitted dust aerosols warm the surface of mountaintops through ASI, in which the reduced snow albedo associated with dusty snow leads to more surface absorption of solar radiation and reduced SWE. Transported aerosols and local anthropogenic aerosols play a dominant role in increasing non-precipitating clouds but reducing precipitation through ACI, leading to reduced SWE and runoff over the Sierra Nevada, as well as the warming of mountain tops associated with decreased SWE and hence lower surface albedo. The average changes in surface temperature from October 2012 to June 2013 are about -0.19 K and 0.22 K for the whole domain and over mountain tops, respectively. Overall, the average reduction during October to June is about 7 percent for precipitation, 3 percent for SWE, and 7 percent for surface runoff for the whole domain, while the corresponding numbers are 12 percent, 10 percent, and 10 percent for the mountaintops. The reduction in SWE is more significant in a dry year, with a 9 percent reduction for the whole domain and 16 percent for the mountain tops. The maximum reduction of ~20 percent in precipitation occurs in May associated with the maximum of aerosol loadings, leading to the largest decrease in SWE and surface runoff over that period. It is also found that dust aerosols could cause early snowmelt at the mountaintops and reduced surface runoff after April.

Six-month downscaling forecast over California has been carried out using WRF and WRF-Chem driven by global forecast data from NCEP Coupled Forecast System Model Version 2 (CFSV2) as initial and boundary conditions. WRF and WRF-Chem predictions well captured the precipitation pattern over the entire California, which illustrates the importance and improvement of dynamical downscaling approach in the regional forecast. Initial conditions seem to play an important role in the model forecast. More detailed analysis and in depth studies will be needed to evaluate the performance of the high-resolution dynamical downscaling and examine the impacts of initial conditions on seasonal forecast.

# CHAPTER 2:

## Impact of Aerosols on Reservoir Inflow: A Case Study for Big Creek Hydroelectric System in California

---

### 2.1 Introduction

Hydroelectric power plants play a key role in supporting the integration of increasing amounts of wind and solar energy as they have high level of operational flexibility and storage capability. Hydroelectric power plants take on important responsibilities such as flood control, navigation, irrigation, agricultural, urban water supply, and recreation in addition to enhancing the stability of power systems and security of power supply. Hence, it is important to determine the optimal operational schedule of single-stage or multistage hydroelectric power plants. An accurate and reliable reservoir inflow forecast model is in crucial need to enable optimal and efficient scheduling of hydroelectric resources (Gagne, et al., 2015; Madsen, et al., 2009; Valipour, et al., 2013)

Typically, the river runoff in the Sierra Nevada region are highly influenced by meteorological variables such as temperature, precipitation, and snow water equivalent (SWE) (Cayan, et al., 1993). Since the reservoir inflows of this region are generated by the runoff captured by the reservoirs, therefore, these meteorological variables can be used as explanatory variables in reservoir inflow forecast models. In the past decade, researchers have discovered that the presence of aerosol particles in the atmosphere can exert great influence on the hydrological cycle in a region through the meteorological variables (Barnett, et al., 2005; Lohmann, 2005; Qian, et al., 2009; Ramanathan, et al., 2001).

Aerosols are a mixture of tiny particles or liquids that are suspended in air and can range from 0.001 to 10  $\mu\text{m}$  in size. A discussion on types and components of aerosol particles considered in this study is provided in Section 2.5.2. It has been shown that an increase in atmospheric aerosols primarily affects solar radiation entering earth's atmosphere, snow albedo, cloud formation, and precipitation. Aerosol effects can be differentiated in three pathways- aerosol-radiation interaction (ARI) or direct effect, aerosol-snow interaction (ASI), and aerosol-cloud interaction (ACI) or indirect effect. Reflective aerosol particles, such as nitrate and sulphate particles, scatter the solar and thermal radiation and increase planetary albedo cooling both surface and atmosphere (Andreae, et al., 2005; Charlson, et al., 1992; Haywood & Boucher, 2000; Johnson, et al., 2004; Kaufman, et al., 2002; Kiehl & Briegleb, 1993; Penner, et al., 2006; Quaas, et al., 2008). However, absorptive aerosols such as black carbon absorb radiation, decrease planetary reflectivity and increase air temperature (Jacobson, 2001; Johnson, et al., 2004). Presence of soot particles and dust in snow darkens the surface and reduces the

snow albedo through aerosol-snow interaction (ASI) (Chylek, et al., 1983; Clarke & Noone, 1985; Doherty, et al., 2010; Flanner, et al., 2007; Grenfell, et al., 2002; Hansen & Nazarenko, 2004; Jacobson, 2004; Lee-Taylor & Madronich, 2002; Marks & King, 2013; Marks & King, 2014) (Reay, et al., 2012; Warren, 1984; Warren & Clarke, 1990; Wiscombe & Warren, 1980; Ye, et al., 2012). Snow albedo perturbations increase the surface air temperature and accelerate snowmelt (Barnett, et al., 2005; Flanner, et al., 2007; Hansen & Nazarenko, 2004; Lau, et al., 2010; Ming, et al., 2009; Qian, et al., 2009; Wiscombe & Warren, 1980; Xu, et al., 2009). Further reduction of snow albedo takes place by snow albedo feedback (Brandt, et al., 2011; Flanner, et al., 2007; Hadley & Kirchstetter, 2012; Hansen & Nazarenko, 2004).

Aerosol-cloud interaction or indirect effect of aerosols on climate includes a change in microphysical and optical properties of cloud droplets, which is related to aerosols acting as cloud condensation nuclei (CCN). Increasing the number concentration of CCN can lead to formation of more cloud droplets, which results in a decrease in cloud droplet radius leading to higher cloud albedo (Jones, et al., 1994; Twomey, 1974; Twomey, 1991). Another effect of decrease in cloud droplet size is the reduced precipitation through the 'second indirect effect' (Ramanathan, et al., 2001; Rosenfeld, 2000). This is because small water droplets continue to drift in air and are less likely to grow to sufficient size to fall out as precipitation prolonging cloud lifetime (Albrecht, 1989; Ackerman, et al., 2004; Kaufman, et al., 2005; Rosenfeld, 2000). Higher cloud reflectivity and increase in cloud lifetime also produce a net cooling effect on earth's surface by shading it from solar radiation. Absorptive aerosols can reduce low-cloud cover through the 'semi-direct effect' (Johnson, et al., 2004; Hansen, et al., 1997) leading to positive radiative forcing. A detailed description of the effect of aerosol on precipitation and snow water equivalent in California (Wu, et al., 2017b) showed that aerosols reduce precipitation and SWE by 10 *percent* over mountaintops in the Sierra Nevada region. This is a result of (both anthropogenic and naturally occurring) aerosols serving as CCN, which leads to an increase of non-precipitating clouds. Aerosol deposition on snow increases absorption of solar radiation, leading to warming and further reduction of SWE over mountaintops. As the level of anthropogenic aerosol particles (such as sulfate and carbonaceous aerosols) increases rapidly from preindustrial times to the present-day over urban and industrial regions, their impact is becoming more significant on the hydrological cycle and thereby on reservoir inflow (Charlson, et al., 1991; Charlson, et al., 1992; Lohmann, 2005; Schwartz, 1996). It should be mentioned that, since aerosols are not evenly distributed around the earth, their impact on reservoir inflow varies quite a lot from region to region. It is critical to understand and quantify the impact of aerosols on reservoir inflow as it can influence hydropower generation and reservoir operations.

The primary objective of this paper is to develop a reservoir inflow forecast model and subsequently quantify the impact of aerosols on inflow into Florence Lake and Lake Thomas Alva Edison in the Big Creek Hydroelectric System. Since Florence Lake and Lake Edison are the higher elevation reservoirs of the system, an accurate forecast of inflow

into these reservoirs can also improve the operational efficiency of the system greatly. The Big Creek Hydroelectric System resides in the San Joaquin Valley, which is surrounded by the Sierra Nevada mountain range in the east. San Joaquin Valley has one of the highest pollutant concentrations in the United States due to its unique geographical location. A detailed description of the study area is provided in Appendix 2.3. Autoregressive integrated moving average model (ARIMA) is a well-known univariate time series model frequently used in hydrological forecasting. ARIMA models can predict a time series variable based on its own past values (AR term) and past values of the error term (MA term). Including exogenous variables in ARIMA model improves forecasting accuracy and is commonly known as ARIMAX model or dynamic regression model. In this paper, the researchers first develop a statistical hydrologic model with dynamic regression method where meteorological variables such as temperature, precipitation, and SWE are used as explanatory variables. The best parsimonious dynamic regression model is selected using the Akaike Information Criterion (AIC), residual diagnostics and goodness-of-fit. Meteorological variables are then simulated using the WRF-Chem model with different aerosol emission levels. These simulated meteorological variables with and without aerosol impacts are fed into the dynamic regression model to quantify the impact of aerosols on reservoir inflow in the Big Creek Hydroelectric System. Detailed analysis of aerosol impacts on temperature, precipitation and SWE in California is not the objective of this study since it has been provided in (Wu, et al., 2017b).

1. The unique contributions of this paper are listed as follows.
2. The researchers developed an innovative and comprehensive framework for evaluating the impact of aerosols on reservoir inflow. The framework seamlessly integrates the numerical weather forecasting model (WRF-Chem) and the statistical inflow forecasting model (dynamic regression).
3. The researchers developed a dynamic regression model to forecast daily inflow into the hydroelectric reservoirs. The model coefficients for the meteorological variables provide an intuitive understanding of how temperature, precipitation, and snow water equivalent influence reservoir inflow.
4. The researchers quantified the impact of aerosols on reservoir inflow in the Big Creek Hydroelectric System based on the proposed dynamic regression model and WRF-Chem model. The simulation results show that the presence of aerosols resulted in a reduction of the annual reservoir inflow by 4 to 14 percent.

The existing research on the effect of climate change and human activities on streamflow (Gleick & Chalecki, 1999; Knowles & Cayan, 2002; Lettenmaier & Gan, 1990; VanRheenen, et al., 2004) and inflow into reservoirs (Brekke, et al., 2004) in the San Joaquin Basin focus on the effect of carbon dioxide and several other greenhouse gases. There are very few examples in the literature studying the effect of natural and anthropogenic aerosols on streamflow and reservoir inflow (Givati & Rosenfeld, 2007). The researchers' study focuses on exploring the impact of aerosols on inflow at the Big

Creek hydroelectric System located in the upper San Joaquin River system in the Sierra Nevada Mountains of Central California.

The remainder of the paper is organized as follows. Section 2.2 summarizes existing studies on statistical inflow forecasting models and discusses the rationality of choosing dynamic regression model. Section 2.3 describes the study area. Section 2.4 presents the overall framework of the researchers' study. Section 2.5 presents the technical methods used in building the dynamic regression model to forecast reservoir inflow and the WRF-Chem model. Section 2.6 describes development of the dynamic regression models and their goodness of fit. Section 2.7 shows the evaluation of the WRF-Chem model and the impact of aerosols on inflow into the two hydropower reservoirs. Lastly, Section 2.8 concludes the paper by discussing the direction of future research and limitations of the study.

## **2.2 Literature Review**

This section presents a review of research articles relevant to this paper that can be grouped into two categories, 1) statistical inflow forecasting models and 2) impact of aerosols on reservoir inflow.

### **2.2.1 Statistical Inflow Forecasting Models**

The existing models for hydrological modeling and forecasting can be separated into three groups; time series models (Moeeni, et al., 2017; Mohammadi, et al., 2005; Papamichail & Georgiou, 2001; Valipour, et al., 2013; Valipour, 2015), regression models (Galeati, 1990; Lall & Bosworth, 1994; Mohammadi, et al., 2005), and artificial neural network (ANN) models (Coulibaly, et al., 2000; Jain, et al., 1999; Kiliç & Cigizoglu, 2003; Mohammadi, et al., 2005; Valipour, 2015; Xu & Li, 2002). (Mohammadi, et al., 2005) compared regression, ARIMA, and ANN models to forecast spring inflows into the Amir Kabir reservoir in the Karaj watershed. (Valipour, et al., 2013) compared ARMA, ARIMA and the autoregressive ANN models to forecast monthly inflows of the Dez dam reservoir. Both of these studies chose ANN as the best model. (Moeeni, et al., 2017) compared SARIMA (seasonal ARIMA) and ANN-GA (ANN combined with genetic algorithm) models in making short-term and long-term predictions of monthly inflow into a dam where SARIMA model outperformed the ANN-GA model, especially in forecasting low values. (Papamichail & Georgiou, 2001) used stochastic SARIMA model to forecast monthly inflow of one or more months ahead into the planned Amopeos Reservoir in Northern Greece, which helped evaluate the optimal real time reservoir operation policies. The monthly forecasts were used to generate a synthetic series of monthly inflows that preserves the key statistics of the historical monthly inflows and their persistence Hurst coefficient, providing a probabilistic framework for reservoir design. Monthly means and the monthly standard deviations of the forecasted inflows were close to that of the measured inflows demonstrating the ability of SARIMA models to forecast monthly inflows and generate synthetic series of monthly inflows. (Valipour, 2015) investigated SARIMA and ARIMA models for long-term runoff forecasting in the

United States. They found SARIMA model to be the best model in their study with an error of < 5 percent for all states. Therefore, ARIMA model can be considered as an effective tool for forecasting reservoir inflow. Including exogenous covariates in ARIMA model (ARIMAX) helps explain the dynamic relationship between the response time series and the explanatory variable time series and improve forecast accuracy.

Some of the underlying assumptions of regression model, such as normal distribution, homoscedasticity and no autocorrelation of error terms, are frequently violated when being applied to time series data (Makridakis, et al., 2008). The ARIMA modeling approach can be applied to model the information contained in the error term, which can take care of its autocorrelation. A transfer function model can be used to model the relationship between the response variable and explanatory variables. The regression model with ARIMA errors and transfer function is effectively the ARIMAX or dynamic regression model. Lastly, though ANN models might improve forecast accuracy, it is challenging to interpret the impact of aerosols on inflow by examining the weights on the meteorological input variables. In the light of all these considerations, the researchers decided to adopt the dynamic regression model to forecast inflow into the hydropower reservoirs.

### **2.2.2 Impact of Aerosols on Reservoir Inflow**

Few studies were conducted to examine the impact of anthropogenic aerosols on hydrology and water resources. (Givati & Rosenfeld, 2007) studied the impact of anthropogenic aerosols on available water resources in the Sea of Galilee in northern Israel and outflows of the main springs of Jordan River where large portion of water resources result from orographic precipitation.

They applied the methodology developed by (Givati & Rosenfeld, 2004; Givati & Rosenfeld, 2005) to quantify the trend in orographic precipitation in the catchment areas and relate it to trends in runoff and spring outflows. They concluded that air pollution is the main reason behind the suppression of orographic precipitation over the hilly areas and the subsequent decreasing trend in the available water in the Sea of Galilee. However, the researchers' study is not limited to anthropogenic aerosols. It also includes aerosols from various kinds of natural sources.

## **2.3 Study Area: San Joaquin Region and Big Creek Hydroelectric Project**

The Big Creek Hydroelectric Project is an extensive hydroelectric system that accounts for 12 percent of California's total hydroelectric generation. The project is located on the upper San Joaquin River system in the Sierra Nevada Mountains of Central California. Sierra Nevada is a mountainous region where most precipitation are retained as snow until temperatures are sufficient for melt (Cayan, et al., 1993).

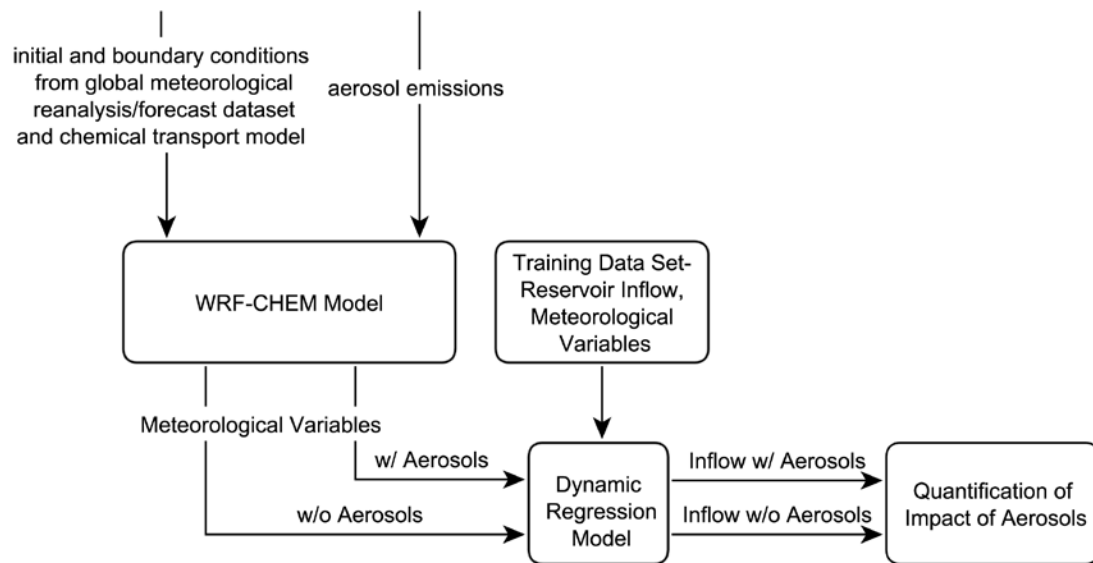
The hydroelectric project is owned and operated by Southern California Edison (SCE), which has a total installed capacity of 1,000 MW accounting for approximately

20 percent of SCE's total generation capacity. The hydroelectric system includes 27 dams, 23 generating units in nine powerhouses, miles of underground tunnels, and six major reservoirs with a combined storage capacity of 560,000 acre feet. Water from lakes in higher elevation are routed through the nine powerhouses and discharged to lakes in lower elevations that are connected through tunnels and penstocks. The water travels a combined vertical distance of 6,655 feet before being discharged through the last powerhouse into the San Joaquin River. Florence Lake and Lake Thomas Alva Edison are the higher elevation reservoirs of the system having surface elevation of 7300 and 7648 feet respectively. The dam at Florence Lake captures runoff from the South Fork San Joaquin River, diverting it through the Ward Tunnel towards the Portal Powerhouse, which is the first powerhouse in the system to receive water. Lake Thomas Alva Edison is formed by the Vermillion Valley Dam constructed across the Mono Creek, a tributary of the South Fork of the San Joaquin River. It discharges some of its water to the Ward Tunnel and thereby further regulates the water supply to the Portal Powerhouse. Water running through Portal Powerhouse is discharged into the Huntington Lake where it is in turn diverted to lakes of lower elevation through other powerhouses. Thus, an accurate forecast of inflow into Lake Thomas Alva Edison and Florence Lake can greatly improve the operational efficiency of the Big Creek Hydroelectric Project.

## 2.4 Framework

This study aims at quantifying the impact of aerosol particles on inflow into Florence Lake Reservoir and Lake Edison and developing daily inflow forecasts for these two reservoirs. A dynamic regression model was developed to forecast the inflow, which uses meteorological variables like daily mean temperature, accumulative snow water equivalent, and incremental precipitation as explanatory variables. Observed inflow data and observed meteorological variables data were split into a training set and a testing set. Testing set was formed by withholding the data for the last water year from the model identification and estimation process and the rest are used as the training set. The training data set was used to estimate the model parameters. The forecasting accuracy of the model was assessed by performing out-of-sample forecasting on the testing set. Forecasts of the predictor variables considering the impact of aerosols on regional climate were calculated in the San Joaquin Valley of California using a version of Weather Research and Forecasting Model with Chemistry (Grell, et al., 2005; Zhao, et al., 2014) with fully coupled aerosol-meteorology-snowpack. Meteorological variable forecasts without impact of aerosols were also calculated for the same region. Both forecasts were used as respective testing sets for calculating inflow forecasts with and without impact of aerosols. Yearly and seasonally aggregated inflow forecasts were then compared to quantify the impact of aerosols on inflow into Lake Edison and Florence Lake. The procedure is summarized schematically in Figure 33.

**Figure 33: The Overall Framework for Quantifying the Impact of Aerosols on Reservoir Inflow**



Source: University of California, Riverside

## 2.5 Technical Methods

### 2.5.1 Dynamic Regression Model

A dynamic regression model or ARIMAX model (Pankratz, 2012) uses time lagged explanatory variables to forecast the dependent variable while modeling the error term with an ARIMA model (Box, et al., 2015). Reasons for choosing dynamic regression model were discussed in Section 2.2. The researchers conducted model development by applying relevant theory to choose the input variables and then following standard methodology for building dynamic regression models. The linear transfer function (LTF) method suggested by (Pankratz, 2012) was applied here to specify the transfer functions and the methodology described by (Box, et al., 2015) was applied to determine ARMA order of the error time series. Finally, the coefficients of the entire model were estimated and the model was checked for adequacy. An overview of the dynamic regression model and LTF method is provided.

A dynamic regression model is shown in Equation (2.1). A crucial assumption in dynamic regression is that the explanatory variables are not affected by the dependent variable, i.e. there is no feedback between the variables.

$$Y_t = v(B)X_t + N_t \quad (2.1)$$

where

$Y_t$  = Dependent variable

$X_t$  = The vector of explanatory variables

$v(B)$  = Transfer function

$N_t$  = Noise time series

A free form distributed lag transfer function model like Equation (2.2) for M explanatory variables can be estimated where the noise series is approximated by a low order regular AR term proxy. The order of the transfer function  $k_i$  is chosen based on the empirical understanding of the model.

$$Y_t = \sum_{i=1}^M \sum_{j=0}^{k_i} v_{i,j} X_{i,t-j} + \frac{1}{\phi(B)} a_t \quad (2.2)$$

where

$X_{i,t}$  = i-th explanatory variable

$\phi(B)$  = Low-order autoregressive proxy

$a_t$  = White Noise

The individual weights  $v_{i,j}$  are called impulse response weights. The transfer function can be written in a parsimonious form known as a rational distributed lag transfer function model as shown in Equation (2.3).

$$Y_t = \mu + \sum_{i=1}^M \frac{\omega_i(B)}{\delta_i(B)} B^{b_i} X_{i,t} + N_t \quad (2.3)$$

where

$Y_t$  = Dependent variable

$X_{i,t}$  = i-th explanatory variable

$\omega_i(B)$  = Numerator polynomial of the transfer function =  $\omega_{i,0} + \omega_{i,1}B + \omega_{i,2}B^2 \dots + \omega_{i,h_i}B^{h_i}$

$\delta_i(B)$  = Denominator polynomial of the transfer function =  $1 - \delta_{i,1}B - \delta_{i,2}B^2 - \dots - \delta_{i,r_i}B^{r_i}$

$b_i$  = Dead time for input  $X_{i,t}$

$B$  = Backshift operator

It should be noted that  $(r_i, h_i, b_i)$  are constants for the  $i$ -th explanatory variable.  $(b, r, h)$  are the orders of the rational distributed lag transfer function. The numerator of the transfer function model captures the lagged effect of the covariates and the denominator represents the decaying effects of the covariates. The noise series  $N_t$  may have an autocorrelated time structure that can be described by an ARIMA model.

The autoregressive (AR) component in the ARIMA model refers to the lagged values of the dependent variable time series; the moving average (MA) component refers to the lagged error terms, i.e. residuals; and the integrated component represents the number

of times a time series must be differenced to achieve stationarity. A general notation for ARIMA models is  $ARIMA(p, d, q)$  where  $p$  denotes the number of autoregressive terms,  $q$  denotes the number of moving average terms, and  $d$  denotes the number of times a series must be differenced to induce stationarity. Using the general notations of an ARIMA model, the noise series can be written as:

$$N_t = \frac{\theta(B)}{\phi(B)} a_t \quad (2.4)$$

where

$$\phi(B) = 1 - \phi_1 B - \dots - \phi_p B^p$$

$$\theta(B) = 1 - \theta_1 B - \dots - \theta_q B^q$$

Here,  $a_t$  is assumed to be white noise. The white noise assumption implies zero mean, normal distribution, and constant variance.

#### 2.5.1.1 Linear Transfer Function (LTF) Method

The linear transfer function (LTF) method suggested by (Pankratz, 2012) was applied in this study to handle multiple inputs. The order of the rational form transfer function  $(b_i, r_i, h_i)$  for each variable  $i$  needs to be determined together with the order of  $ARIMA(p, d, q)$  model for the noise time series  $N_t$ . LTF method uses a free form distributed lag model to estimate the impulse response weights in Equation (2.2) together with an initial autoregressive proxy for the autocorrelation term of the disturbance time series  $N_t$ . If  $N_t$  is not stationary with time varying mean, then both the input and output time series should be differenced accordingly. A parsimonious rational form transfer function similar to Equation (2.3) is then identified by comparing the estimated impulse response weight pattern with theoretical impulse response weight patterns. The methodology described by (Box, et al., 2015) is then applied to determine ARMA order of the error time series  $N_t$ . Finally, the coefficients of the entire model are estimated and the model is checked for adequacy.

Out-of-sample forecasting was performed to assess the forecasting accuracy of the model (Makridakis, et al., 2008). Some of the sample data at the end of the time series were withheld as the testing dataset. They were not used in the model identification and estimation process. The fitted model was used to forecast the response variable. Root mean square error (RMSE) and mean absolute error (MAE) were used as accuracy metrics to evaluate the performance of the proposed model and the benchmark models introduced in Section 2.5.1.1. RMSE and MAE values signify the goodness of fit of the forecast to the observed inflow and hence can evaluate the performance of the dynamic regression model.

$$RMSE = \sqrt{\frac{\sum_{i=1}^n (Y_{fi} - Y_{oi})^2}{n}} \quad (2.5)$$

$$MAE = \sum_{i=1}^n \frac{|Y_{fi} - Y_{oi}|}{n} \quad (2.6)$$

Here,  $i$  denotes the day in a water year,  $Y_{fi}$  represents the forecasted inflow on day  $i$ ,  $Y_{oi}$  denotes the observed inflow on day  $i$ , and  $n$  is the number of days in the water year.

### 2.5.2 WRF-Chem Model

The WRF-Chem model (Grell, et al., 2005) is a weather research and forecasting system that simulates chemistry and aerosols simultaneously with meteorology. This model has been extensively used to study regional air quality and their interactions with weather and climate (Barnard, et al., 2010; Chapman, et al., 2009; Fast, et al., 2012; Fast, et al., 2014; Qian, et al., 2009; Wu, et al., 2011; Wu, et al., 2011; Wu, et al., 2013; Wu, et al., 2017a; Wu, et al., 2017b) (Zhao, et al., 2010; Zhao, et al., 2014; Zhao, et al., 2013). In this study, the researchers used the WRF-Chem version 3.5.1 which includes aerosol interactions with radiation, cloud and snowpack (Zhao, et al., 2014). In the WRF-Chem control (CTRL) experiment, the researchers ran the model at 4 km horizontal resolution with the model domain covering California and surrounding regions. The major components of aerosols (nitrate, ammonium, elemental carbon, primary organic matter, sulfate, sea salt, dust, water, and other inorganic matter) as well as their physical and chemical processes were simulated in the model. Anthropogenic aerosol emissions were obtained from US EPA 2005 National Emissions Inventory (NEI05; US EPA, 2010).

Anthropogenic emissions were updated every hour to account for diurnal variability. However, their seasonal variation was not considered in the simulation. Biomass burning emissions were obtained from the Global Fire Emissions Database version 2.1, with 8-day temporal resolution and monthly updates (Environmental Sciences Division, 2013). However, year-to-year variability in biomass burning aerosols was not taken into account. Dust emissions were calculated using the DUST TRANsport model (DUSTRAN) scheme (Shaw, et al., 2008) following (Wu, et al., 2017a). The microphysics scheme used in this study is the Morrison 2-moment scheme. (Wu, et al., 2017b) showed that the model simulations reproduced the spatial and temporal variation of observed precipitation well. More details of the model setup can be found in (Wu, et al., 2017b).

(Wu, et al., 2017a; Wu, et al., 2017b) evaluated the model performance on simulating aerosols and meteorological variables in California. It has been shown that the model reasonably captures the distribution and seasonal variability of aerosols from October to June, but underestimates aerosols from July to September. Since precipitation, snowpack and inflow are mainly within October-June, the underestimation of aerosols in July-September has limited impacts on the researchers' results. The model reproduced the seasonal variations of temperature, precipitation, and SWE in California with some overestimation of temperature and SWE. In a CLEAN simulation, the researchers turned off local aerosol emissions and set aerosols from boundary conditions as zero, but kept chemical components from boundary conditions with aerosol chemistry on. The CCN in

the CLEAN experiment was approximately  $10 \text{ cm}^{-3}$ , representing a clean environment. The simulations of clouds, precipitation and radiation are reasonable in the CLEAN run. Thus, meteorological variables from the WRF-Chem CTRL and WRF-Chem CLEAN simulations represent conditions with and without considering impact of aerosols respectively. Aerosol impacts on temperature, precipitation, and SWE were investigated in (Wu, et al., 2017b) and discussed in the introduction and Section 2.7.

## 2.6 Building Inflow Forecasting Model

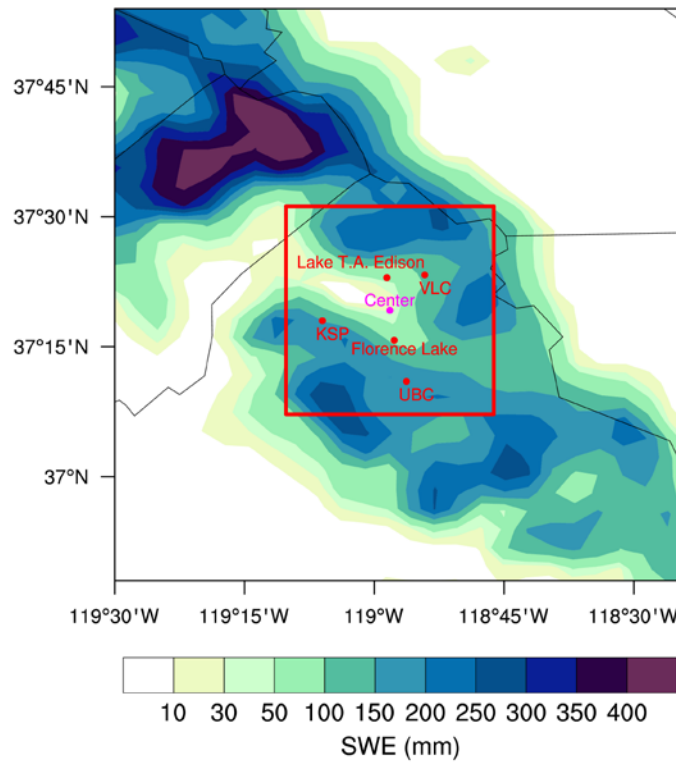
In this section, the researchers explain how to build the dynamic regression model to forecast reservoir inflow of Florence Lake and Lake Edison, which are part of the Big Creek Hydroelectric Project in California.

### 2.6.1 Data Description

The data set contains the daily average reservoir inflow in *cu ft/s* for five consecutive water years 2010-2014. A water year or a hydrological year is a 12-month period between October 1 of one year and September 30 of the next year. To predict the reservoir inflow, the researchers collected the meteorological data such as the daily air temperature, SWE, and incremental precipitation data from the website of California data exchange center. Data for meteorological variables, inflow and WRF-Chem simulations used in this study can be found in (Department of Water Resources, 2017).

The meteorological data were collected and averaged over three weather stations of Kaiser Point (KSP), Volcanic Knob (VLC), and Upper Burnt Corral (UBC) located within the  $0.4 \times 0.4^\circ$  grid box with center at  $(37.32^\circ N, -118.97^\circ E)$ . The study area with the grid box is shown in Figure 34 with the snow depth distribution map averaged over water year 2013 overlaid on it. The observations of these meteorological variables are plotted in Figure 35.

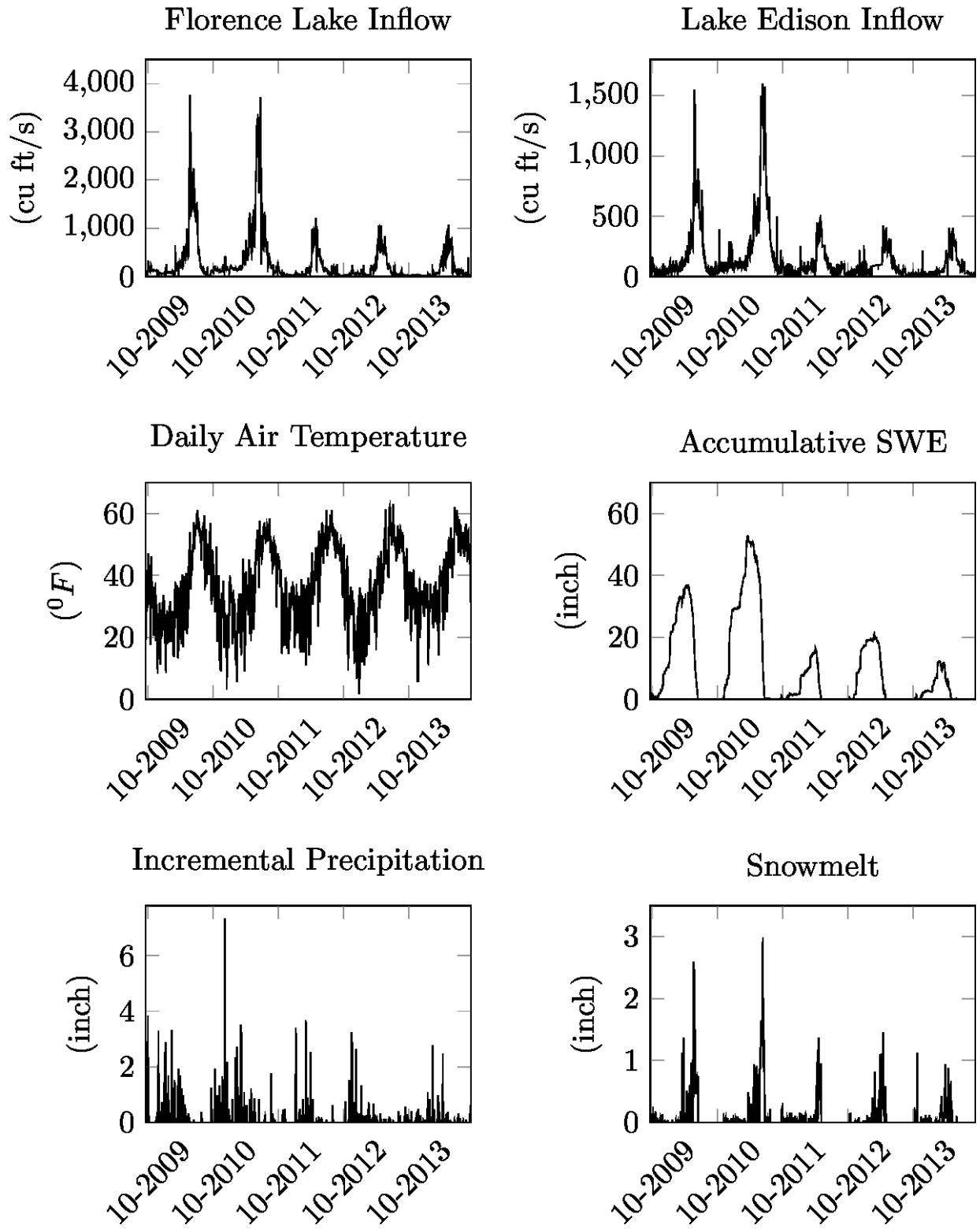
**Figure 34: Study Area With Grid Box and Weather Stations Identified**



Snow depth distribution averaged over water year 2013 is overlaid on the map

Source: University of California, Riverside

Figure 35: Response Variables and the Explanatory Variables for Water Year 2010-2014



Source: University of California, Riverside

## 2.6.2 Predictor/Variable Selection

Selection of appropriate predictors or explanatory variables is essential for accurate forecast and simple model interpretation. The inflows are generated by the runoff captured by the reservoirs from the San Joaquin River. Streamflow in the Sierra Nevada region has high correlation with temperature, SWE, and precipitation (Cayan, et al., 1993). Therefore, these three variables were included in the model to forecast the inflow.

Being a mountainous region, runoff in the Sierra Nevada region is dominated by snowmelt. Maximum runoff in the San Joaquin watershed occurs during the snowmelt runoff period (April-July) (Serreze, et al., 1999; Stewart, et al., 2004). Accordingly, most of the reservoir inflows occur in the late spring and early summer between April and July in both Florence Lake and Lake Edison (Serreze, et al., 1999; Stewart, et al., 2004). Therefore, snowmelt during this period is a useful predictor for reservoir inflow. Snowmelt can be calculated by  $\max SWE_t - SWE_{t-1}$ .

To handle the seasonality, four dummy variables were introduced in Table 7: Response Variables and the Explanatory Variables for Water from 2010-2014 to represent four periods in a year. These periods are early spring, late spring, early summer, and late summer. The researchers also added interaction terms between the four meteorological variables with seasonal dummy variables to model different effects of meteorological variables in different seasons. Since there is a lag of several months between the peak snow accumulation and peak inflow in the researchers' study area as seen from Table 7, 80 days lagged snow water equivalent in the late summer was included in the final model to capture this effect. The complete list of variables in building the statistical dynamic regression model is tabulated in Table 8: List of Variables Used in the Dynamic Regression Model of Variables Used in Dynamic Regression Model.

**Table 7: Response Variables and the Explanatory Variables for Water from 2010-2014**

Dummy Variables	Description	Season
$D_1$	if Date 03/21-04/30, 0 otherwise	Early Spring
$D_2$	If Date 05/01-05/31, 0 otherwise	Late Spring
$D_3$	If Date 06/01-06/21, 0 otherwise	Early Summer
$D_4$	If Date 06/22-09/22, 0 otherwise	Late Summer

Source: University of California, Riverside

**Table 8: List of Variables Used in the Dynamic Regression Model**

Variables	Symbols
Reservoir Inflow	$Y$
Temperature	$X_1$
SWE	$X_2$
Precipitation	$X_3$
Snowmelt	$X_4$
Dummy Variables	$D_1, D_2, D_3, D_4$
Interaction Terms	$X_1D_1, X_1D_2, X_1D_3, X_1D_4, X_2D_1, X_2D_2, X_2D_3, X_2D_4, X_3D_1, X_3D_2, X_3D_3, X_3D_4, X_4D_1, X_4D_2, X_4D_3, X_4D_4$

Source: University of California, Riverside

### 2.6.3 Model Development

The team explored the model performance with and without natural log transformation of the response and explanatory variables and chose untransformed variables for further model building as it offered better prediction results and model interpretation. The development of the dynamic regression model for Florence Lake inflow forecast is described here. Similar procedure can be followed for Lake Edison. The development of dynamic regression model has three stages, (1) model identification, (2) model estimation, and (3) model diagnostic checking.

#### 2.6.3.1 Model Identification

As the first step to identify the appropriate dynamic regression model, a free form distributed lag for the transfer function of the explanatory variables like Equation (2.2) was estimated with a low order regular AR term as proxy for the disturbance series autocorrelation pattern. A multiple regression model was formed and stepwise regression was performed to preliminarily select candidate variables and their time lags for building the free form distributed lag model. The orders of  $v(B)$  for the other variables in the free form distributed lag model were determined to be 15 based on their  $t$ -test statistics. It can be argued that the inflow is zero when the explanatory variables are zero i.e. when there is no snowmelt or precipitation and the temperature is 0°F. Therefore, no constant term was included in the model.

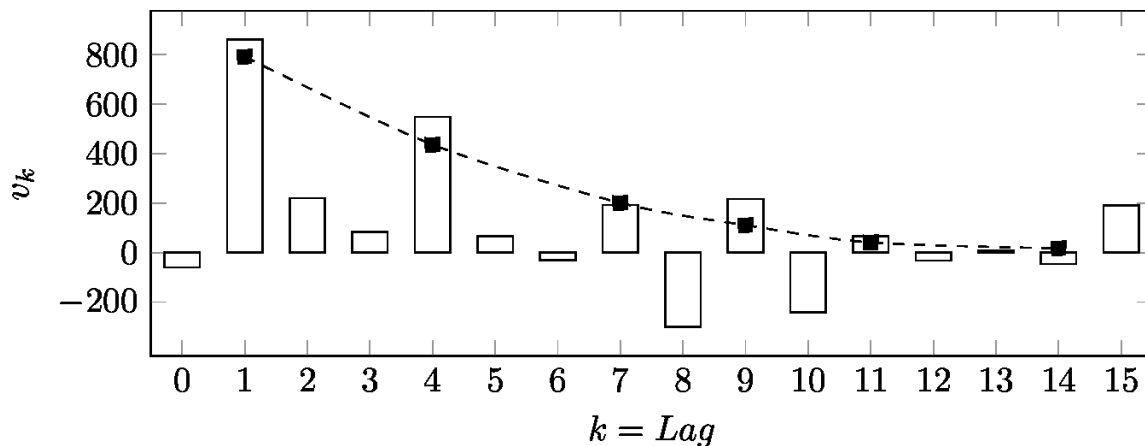
The disturbance series  $N_t$  was then checked for stationarity by augmented Dickey-Fuller test and found to be stationary. A parsimonious rational distributed lag transfer function model of order  $(b, r, h)$  similar to Equation (2.3) was identified by comparing the estimated impulse response weights with theoretical impulse response weight patterns. To demonstrate the process, the estimated impulse response weights of the variable  $X_4D_3$ , which corresponds to snowmelt in early summer, are shown in Table 9: Impulse Response Weights of Input Variable  $X_4D_3$  and plotted in Figure 36.

**Table 9: Impulse Response Weights of Input Variable  $X_4D_3$**

Lag	Estimate	t-value	Lag	Estimate	t-value	p-value
0	59.55	0.67	8	300.71	4.03	<.0001
1	862.75	10.83	9	217.35	3.33	0.0009
2	220.73	2.88	10	-240.18	3.94	<.0001
3	84.11	1.01	11	65.52	1.09	0.2769
4	548.99	6.67	12	-31.77	-0.57	0.5714
5	67.09	0.84	13	8.60	0.15	0.8773
6	-30.91	-0.42	14	-46.42	-0.81	0.4191
7	192.40	2.56	15	190.53	3.39	0.0007

Source: University of California, Riverside

**Figure 36: Impulse Response Weights of Input Variable  $X_4D_3$**



Source: University of California, Riverside

There are six significant  $v$  weights at lag 1, 2, 4, 7, 9 and 15 having  $t$ -value more than 2.0. This suggests that the dead time,  $b_1 = 1$ . Since the 6 significant impulse response weights follow an exponential decay pattern, the order of the denominator operator was

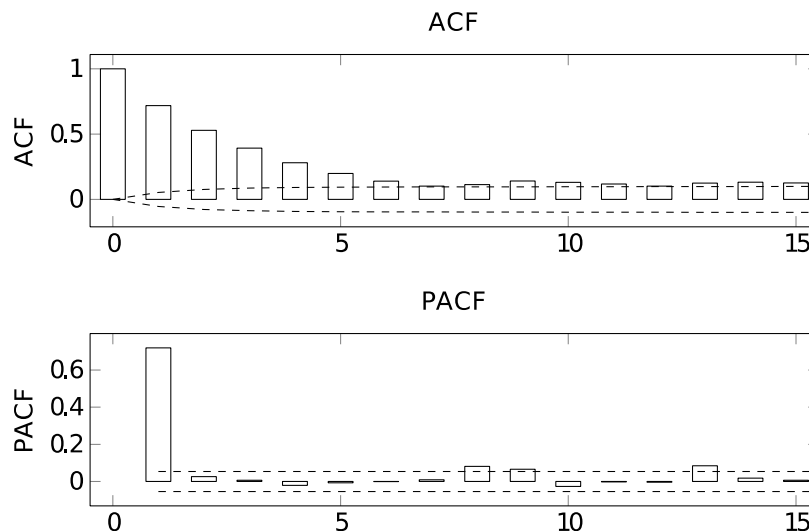
determined to be  $r = 1$ . The number of unpatterned terms is  $u = 0$ . Finally, the order of the numerator operator is  $h = u + r - 1 = 0 + 1 - 1 = 0$ . The order of the rational distributed lag transfer function for input variable snowmelt in early summer  $X_4D_3$  was thus determined to be  $(b, r, h) = (1, 1, 0)$  and the transfer function could be written as  $\frac{\omega_i}{(1-\delta_i)^B}$ . Similar procedure was followed for other input variables, and the dynamic regression model with parsimonious rational distributed lag transfer function similar to Equation (2.3) was determined.

### 2.6.3.2 Model Estimates

An estimate of the parameters of the dynamic regression model was obtained at this stage. An appropriate ARMA model was identified for the error series  $N_t$  and the entire model was refit using the ARMA model for error and the transfer function for the input variables. The parameter estimates of all candidate models were estimated by maximum likelihood estimation.

First, the model was fit using only the transfer function of the input variables. The orders of AR and MA component of the model were identified by matching empirical autocorrelation patterns, e.g. autocorrelation function plot (ACF) and partial autocorrelation function (PACF) plots of the residual series with the AR and MA signature patterns (Figure 37). The ACF and PACF plots of the residual series are plotted in 8. ACF and the PACF exhibit large spikes that gradually die out indicating that they have autoregressive and moving averages properties. Though the ACF decays rather slowly and cuts off at lag 6, an AR order of  $p = 6$  is not realistic. An AR order of  $p = 1$  was selected based on the Akaike Information Criterion (AIC) and ACF of the residuals. The PACF cuts off at lag 1. Therefore, the final ARMA model for the error series was determined to be  $(p, q) = (1, 1)$ . At this stage, the dynamic regression model for Florence Lake can be written as Equation (2.7).

**Figure 37: ACF and PACF of Noise Series  $N_t$**



### 2.6.3.3 Diagnostic Checking

The Ljung-Box test for white noise was used to statistically evaluate the degree to which the residuals are free from serial correlation. For seasonal time series, the lag for Ljung-Box test is recommended to be  $h = \min(2m, \frac{T}{5})$  where  $m$  is the period of seasonality and  $T$  is the sample size. In the researchers' study, the lag was calculated to be  $h = 365 \times \frac{3}{5} = 219$ . Though the residuals are not perfect white noise after lag = 25; for a long time series, this is acceptable. Moreover, Durbin Watson Statistic was calculated to detect presence of autocorrelation in the residuals and found to be 2, which shows that the residuals are not autocorrelated. Normality check of the model residuals was performed by checking a histogram of the residuals and the Q-Q normal plot of the residuals. The residuals were found to be approximately normally distributed and the Q-Q normal plot is approximately a straight line. The explanatory variables in the final model were checked for multicollinearity. For all explanatory variables, variance inflation factor (VIF) was calculated. A VIF close to 1 for an explanatory variable indicates no correlation of that predictor and the remaining explanatory variables. For all explanatory variables in this model, VIF was found to be  $< 1.60$ . Hence, there is no multicollinearity. Since there is no significant residual cross correlation and autocorrelation left, the model is adequate. Similar procedure was followed for Lake Edison. The dynamic regression model for Florence Lake and Lake Edison can be written as Equation (2.7) and (2.8)

$$\begin{aligned}
Y_t = & (\omega_{0,0} + B\omega_{0,1} + B^2\omega_{0,2} + B^3\omega_{0,3} + B^4\omega_{0,4})X_{3,t} + \\
& (\omega_{1,0} + B\omega_{1,1} + B^2\omega_{1,2} + B^3\omega_{1,3})X_{1,t}D_{1,t} + \\
& (\omega_{2,0} + B\omega_{2,1} + B^2\omega_{2,2} + B^3\omega_{2,3})X_{1,t}D_{2,t} + \\
& \frac{\omega_3}{(1-\delta_3B)}X_{4,t}D_{2,t} + (\omega_{4,0} + B\omega_{4,1} + B^2\omega_{4,2} + B^3\omega_{4,3})X_{1,t}D_{3,t} + \\
& \frac{\omega_5}{(1-\delta_5B)}X_{4,t}D_{3,t} + \omega_6B^{80}(X_{2,t})D_{4,t} + \frac{\omega_7}{(1-\delta_7B)}BX_{4,t}D_{4,t} + \frac{(1-\theta_1B)}{(1-\phi_1B)}a_t
\end{aligned} \tag{2.7}$$

$$\begin{aligned}
Y_t = & \omega_0X_{1,t} + \omega_1X_{3,t} + (\omega_{2,0} + B\omega_{2,1} + B^2\omega_{2,2} + B^3\omega_{2,3})X_{1,t}D_{1,t} + \\
& (\omega_{3,0} + B\omega_{3,1} + B^2\omega_{3,2} + B^3\omega_{3,3} + B^4\omega_{3,4})X_{1,t}D_{2,t} + \frac{\omega_4}{(1-\delta_4B)}X_{4,t}D_{2,t} + \\
& (\omega_{5,0} + B\omega_{5,1} + B^2\omega_{5,2} + B^3\omega_{5,3})X_{1,t}D_{3,t} + \frac{\omega_6}{(1-\delta_6B)}X_{4,t}D_{3,t} + \\
& \omega_7B^{80}(X_{2,t})D_{4,t} + \frac{\omega_8}{(1-\delta_8B)}BX_{4,t}D_{4,t} + \frac{(1-\theta_1B)}{(1-\phi_1B)}a_t
\end{aligned} \tag{2.8}$$

**Table 10: Parameter Estimates for Inflow Forecast Model of Florence Lake**

Coefficient	Value	Standard error	<i>t</i> -value	<i>p</i> -value
$\theta_1$	.07	0.04	1.91	0.06
$\phi_1$	0.78	0.02	33.60	<0.0001
$\omega_{0,0}$	14.06	8.81	1.60	0.1
$\omega_{0,1}$	6.37	9.08	0.70	0.5
$\omega_{0,2}$	9.24	9.10	1.01	0.3
$\omega_{0,3}$	7.74	9.079	0.85	0.4
$\omega_{0,4}$	12.79	8.83	1.45	0.1
$\omega_{1,0}$	1.16	1.27	0.92	0.3
$\omega_{1,1}$	6.17	1.38	4.47	<0.0001
$\omega_{1,2}$	1.06	1.38	0.77	0.4
$\omega_{1,3}$	2.10	1.26	1.66	0.09
$\omega_{2,0}$	2.13	1.23	1.73	0.08
$\omega_{2,1}$	8.40	1.29	6.51	<0.0001
$\omega_{2,2}$	-0.50	1.31	-0.38	0.7
$\omega_{2,3}$	0.06	1.23	0.05	0.9
$\omega_3$	93.18	23.23	4.01	<0.0001
$\delta_3$	0.95	0.02	50.05	<0.0001
$\omega_{4,0}$	0.86	1.29	0.66	0.5
$\omega_{4,1}$	3.05	1.12	2.72	0.006
$\omega_{4,2}$	1.97	1.12	1.76	0.08
$\omega_{4,3}$	2.49	1.10	2.25	0.02
$\omega_5$	324.03	38.22	8.48	<0.0001
$\delta_5$	0.79	0.03	26.68	<0.0001
$\omega_6$	12.92	1.94	6.66	<0.0001
$\omega_7$	149.15	19.66	7.59	<0.0001
$\delta_7$	0.92	0.01	62.27	<0.0001

**Table 11: Parameter Estimates for Inflow Forecast Model of Lake Edison Results and Analysis**

Coefficient	Value	Standard error	t-value	p-value
$\theta_1$	-0.03	0.03	-0.89	0.4
$\phi_1$	0.86	0.02	49.14	<0.0001
$\omega_0$	0.52	0.24	2.25	0.02
$\omega_1$	21.55	2.75	7.85	<0.0001
$\omega_{2,0}$	0.31	0.46	0.69	0.5
$\omega_{2,1}$	2.39	0.45	5.36	<0.0001
$\omega_{2,2}$	<b>0.97</b>	0.44	2.17	0.03
$\omega_{2,3}$	0.56	0.43	1.30	0.2
$\omega_{3,0}$	1.16	0.45	2.58	.0099
$\omega_{3,1}$	2.18	0.42	5.15	<0.0001
$\omega_{3,2}$	1.75	0.43	4.06	<0.0001
$\omega_{3,3}$	0.64	0.42	1.51	0.1
$\omega_{3,4}$	0.47	0.37	1.27	0.2
$\omega_4$	56.90	12.65	4.50	<0.0001
$\delta_4$	0.31	0.23	1.35	0.2
$\omega_{5,0}$	0.58	0.46	1.26	0.2
$\omega_{5,1}$	0.68	0.37	1.80	0.07
$\omega_{5,2}$	1.38	0.37	3.69	0.0002
$\omega_{5,3}$	2.12	0.37	5.71	<0.0001
$\omega_6$	126.80	14.58	8.70	<0.0001
$\delta_6$	0.84	0.02	34.52	<0.0001
$\omega_7$	2.48	0.88	2.82	0.0048
$\omega_8$	85.75	8.24	10.40	<0.0001
$\delta_8$	0.94	0.008	107.91	<0.0001

Source: University of California, Riverside

#### 2.6.3.4 Parameter Estimates and Interpretation

The estimated parameter values of the dynamic regression models with their  $t$ -values,  $p$ -values and standard error are shown in Table 10 and Table 11. A larger value of absolute  $t$ -statistic and low  $p$ -value ( $< 0.05$ ) imply that the true parameter value is not 0. It can be observed that, temperature, SWE, and precipitation play important roles in forecasting reservoir inflow. For both lakes, snowmelt during spring and summer has a strong and positive correlation with inflow. With high  $t$ -values, snowmelt is the most important variable in explaining the variability of inflow. This result is consistent with the fact that the runoff in the Sierra Nevada region is dominated by snowmelt. Prior season's SWE is also found to be a useful predictor for inflow during late summer. This can be explained by the fact that the snowpack during cold seasons plays a crucial role in runoff and subsequent reservoir inflow during warmer seasons in the Sierra Nevada region. Current season's temperature has a positive correlation with reservoir inflow in early/late spring and early summer. This is because, in higher elevation rivers, warmer temperature produces faster runoff and less snow (Cayan, et al., 1993). Apart from early/late spring and early summer, temperature does not have a significant impact at Florence Lake, but has moderate impact at Lake Edison. As shown in the model fitting results, same season precipitation has significant impact on reservoir inflow at Florence Lake and Lake Edison. As expected, precipitation is positively correlated with inflow since a higher level of precipitation generally results in more inflow.

#### 2.6.3.5 Inflow Forecast Using Dynamic Regression Model

After calibrating the dynamic regression model with the help of historical data, the next step of the study is to simulate inflow corresponding to the future meteorological variables. The forecast period is set to 365 days. The out-of-sample forecasting ability of the model was assessed by forecasting the reservoir inflow for both lakes in water year 2014 using a testing set containing average meteorological data for the grid box region. The Root Mean Square Error (RMSE) and Mean Absolute Error (MAE) of inflow forecast were calculated and are shown in Table 12

**Table 12: Forecast Error Statistics (cu ft/s) for Water Year 2014**

Lake	Statistics	Dynamic Regression	Regression	Naive
Florence	RMSE	100.75	114.33	136.62
	MAE	73.46	73.46	79.02
Edison	RMSE	44.52	50.97	67.85
	MAE	27.84	38.12	38.31

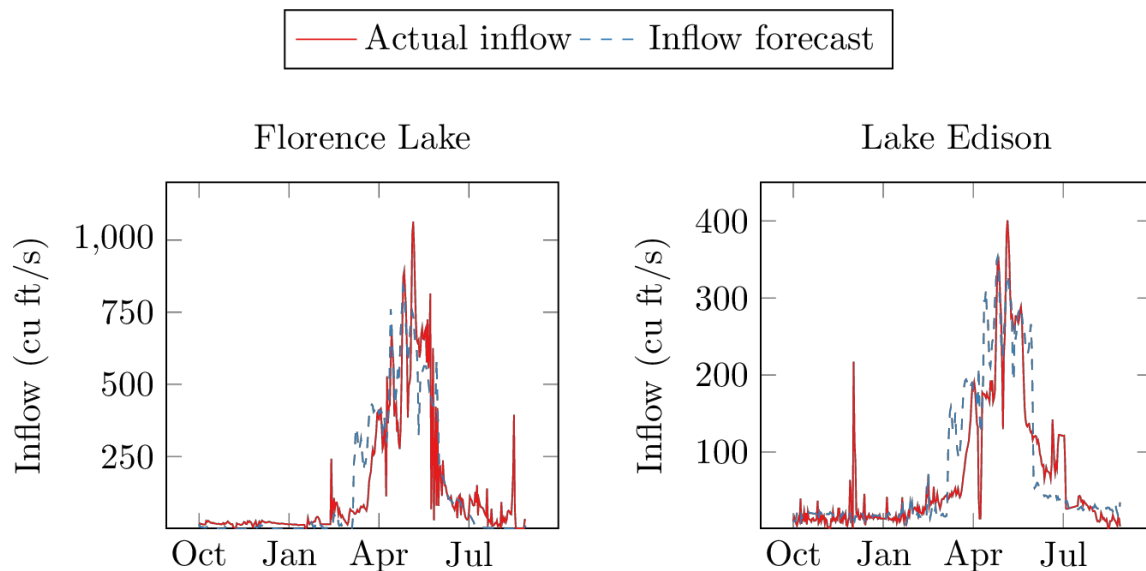
Source: University of California, Berkeley

For comparison, the researchers included a benchmark model, which is a multiple regression model containing the same explanatory variables as the dynamic regression model. The time lagged relationships were incorporated by including the time lagged variables as separate explanatory variables. Inflow of the previous day was also included as an explanatory variable. RMSE and MAE from this multiple regression model are shown in Table 12. Another benchmark model would be a naive model. The naive model in the researchers' study has been determined as Equation (2.9)

$$Y_t = Y_{t-365} \times \frac{\text{Peak SWE}_{\text{current year}}}{\text{Peak SWE}_{\text{previous year}}} \quad (2.9)$$

The small root mean square error indicates that the dynamic regression model is capable of producing a reasonable forecast of inflows into the reservoirs. The error in annual inflow forecast for Florence Lake and Lake Edison are only 0.15 percent and 10 percent respectively. The results of both RMSE and MAE indicate that the dynamic regression model consistently outperforms the benchmark multiple regression model and the naive model. Moreover, the dynamic regression model is more parsimonious compared to the multiple regression model. Actual and forecasted inflow for Lake Edison and Florence Lake are plotted in Figure 38. Based on the plots, the dynamic regression model can perform one year ahead forecast of the reservoir inflow reasonably well.

**Figure 38: Comparison of Actual Inflow and Inflow Forecast with Observed Meteorological Variables in Water Year 2014**



Source: University of California, Riverside

### 2.6.3.6 Sensitivity Analysis of the Dynamic Regression Model

A global sensitivity analysis of the dynamic regression model was performed with the purpose of assessing robustness of the model and simulation results. Input values of

the model were perturbed within their reasonable range and subsequent changes in model output were studied (Baroni & Tarantola, 2014; Chu-Agor, et al., 2011; Tomassini, et al., 2007; Uusitalo, et al., 2015). Changes in input values automatically cause perturbations in parameter estimates of the dynamic regression model. Little change in resultant output values indicates robustness of the model to perturbations of inputs and parameter estimates and shows the uncertainty of the output variables to be relatively small (Uusitalo, et al., 2015).

A qualitative global sensitivity analysis (GSA) was performed in this study by visual inspection of model predictions. All input values were varied simultaneously within the entire allowable ranges of the input space and the effect on the output was studied (Baroni & Tarantola, 2014; Pianosi, et al., 2016). This allowed GSA to evaluate the relative contributions of each input factor to the model output variable and account for effects of nonlinear interactions between different inputs (Baroni & Tarantola, 2014; Ciannelli, et al., 2004; Harper, et al., 2011; Saltelli, et al., 1999). Though local sensitivity analysis where inputs are varied one at a time (OAT) is more common, it assumes linear relationship between inputs and outputs, making it only a perfunctory sensitivity analysis for most models (Saltelli, et al., 2010). GSA does not assume any such specific relationship between inputs and model predictions and therefore, is recommended for any kind of model (Saltelli, et al., 2010; Makler-Pick, et al., 2011; Rosolem, et al., 2012).

The researchers followed the General Probabilistic Framework (GPF) based on Monte Carlo simulation for the global sensitivity analysis of deterministic models proposed by (Baroni & Tarantola, 2014). The flowchart for the GPF can be found in (Baroni & Tarantola, 2014). As is the norm, output in the sensitivity analysis does not refer to the entire range of temporal inflow variable produced by the model (Pianosi, et al., 2016). Rather, it is measured as the variability induced in the model performance measure, RMSE of the testing set. In the first step, all sources of uncertainty in the input meteorological variables  $U_{xi}$  were characterized. Since meteorological data were taken as the average of three weather stations- namely KSP, UBC and VLC, uncertainty may arise due to variability of meteorological variables between the calculated average and actual value at the location of Florence Lake and Lake Edison. Errors and approximations in input data measurement are other sources of uncertainty. Since meteorological variable measurements are not available at Florence Lake and Lake Edison, to account for the uncertainty, a grid box of  $0.5 \times 0.5^\circ$  with center at  $32.32^\circ N, -118.97^\circ E$  was considered. Two more weather stations, Huntington Lake (HNT) and Tamarack Summit (TMR), are located within the grid box along with the three existing weather stations. Average of the meteorological variables in these five weather stations were calculated. In accordance with the comparison between data from the average of three weather stations and five weather stations, a random error was introduced to the daily nominal value of each variable. Measurement difference in the meteorological variables depend on type of water year and season. As such, unnaturally big variability can be introduced if random values are taken from the probability distribution of the difference time series. To preserve the temporal correlation of the meteorological variables, a random

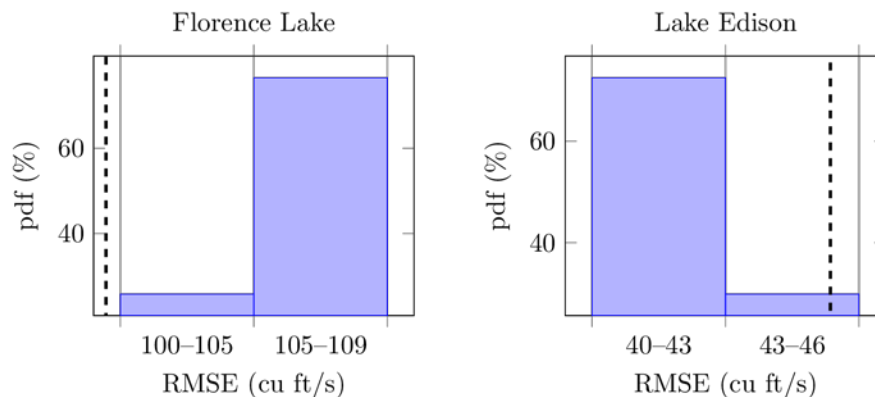
variable following uniform distribution on the interval [0, 1] was multiplied with  $(x_{5\text{ stations}} - X_{3\text{ stations}})$  where  $X$  denotes meteorological variables. The resultant random error was added to the meteorological variables data to produce the perturbed inputs. Each variable was physically constrained to avoid unrealistic values (e.g. negative value for precipitation and SWE).

The realization of each uncertainty was then associated with a scalar input factor  $F_i = 1 \dots 128$  for  $i = 1..3$ . The three input factors were assumed to be independent. To minimize the number of model runs, a quasi-randomized, low-discrepancy sampling design called sobol sequence was used to sample the three discrete uniform distribution according to the method present in (Baroni & Tarantola, 2014; Saltelli, et al., 2010). No correlations among the three input factors were considered in the sampling design. The simulations were run using a number of sampling points  $N = 128$ , which corresponds to total number of model runs,  $N_t = N(2 \times 3 + 2) = 1024$ . A combination of MATLAB and SAS codes were run to perform the sensitivity analysis.

*Result and analysis*

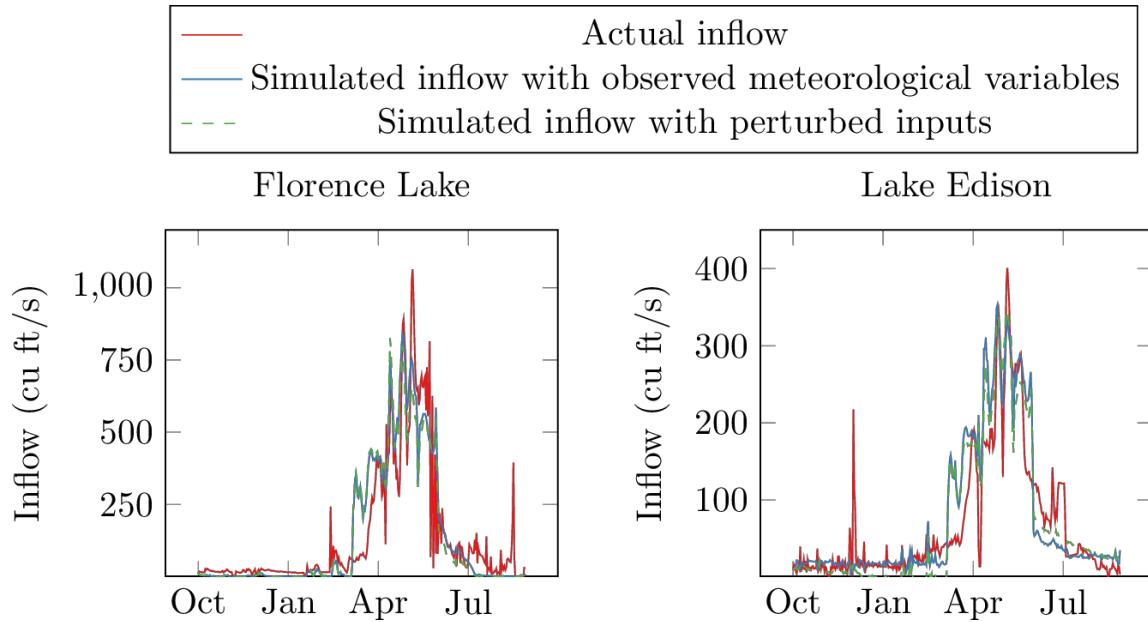
Figure 39 shows the probability distribution of the RMSE of forecasted inflow with perturbed inputs at Florence Lake and Lake Edison in water year 2014. Out of the 1024 model runs performed in the sensitivity analysis, the model that produces median RMSE is selected for analysis of results. Forecasts of the selected perturbed input model are plotted in Figure 40 along with actual inflows and forecasts of reference model for both lakes in water year 2014. The annual inflow of the selected perturbed input model is compared with the observed and reference model inflow forecast for water year 2014 in Table 13. Here, reference model is the inflow forecast model with unperturbed inputs. Annual inflow for the perturbed model has less than 5 percent error for both Florence Lake and Lake Edison. The RMSE results and forecasts show a general good performance of the model under perturbed inputs, which shows the robustness of the model to perturbed inputs and parameter estimates.

**Figure 39: Probability Distribution Function (%) of the RMSE of Forecasted Inflow with Perturbed Inputs in Water Year 2014**



Source: University of California, Riverside

**Figure 40: Comparison of Actual Inflow, Simulated Inflow, and Simulated Inflow from the Selected Perturbed Input Model with Median RMSE in Water Year 2014**



Source: University of California, Riverside

**Table 13: Annual Reservoir Inflow for the Selected Perturbed Input Model with Median RMSE and Reference Model in Water Year 2014**

Lake	Actual	Reference Model	Perturbed Model
Florence	99979	99818	94872
Edison	49339	54062	49270

Source: University of California, Berkeley

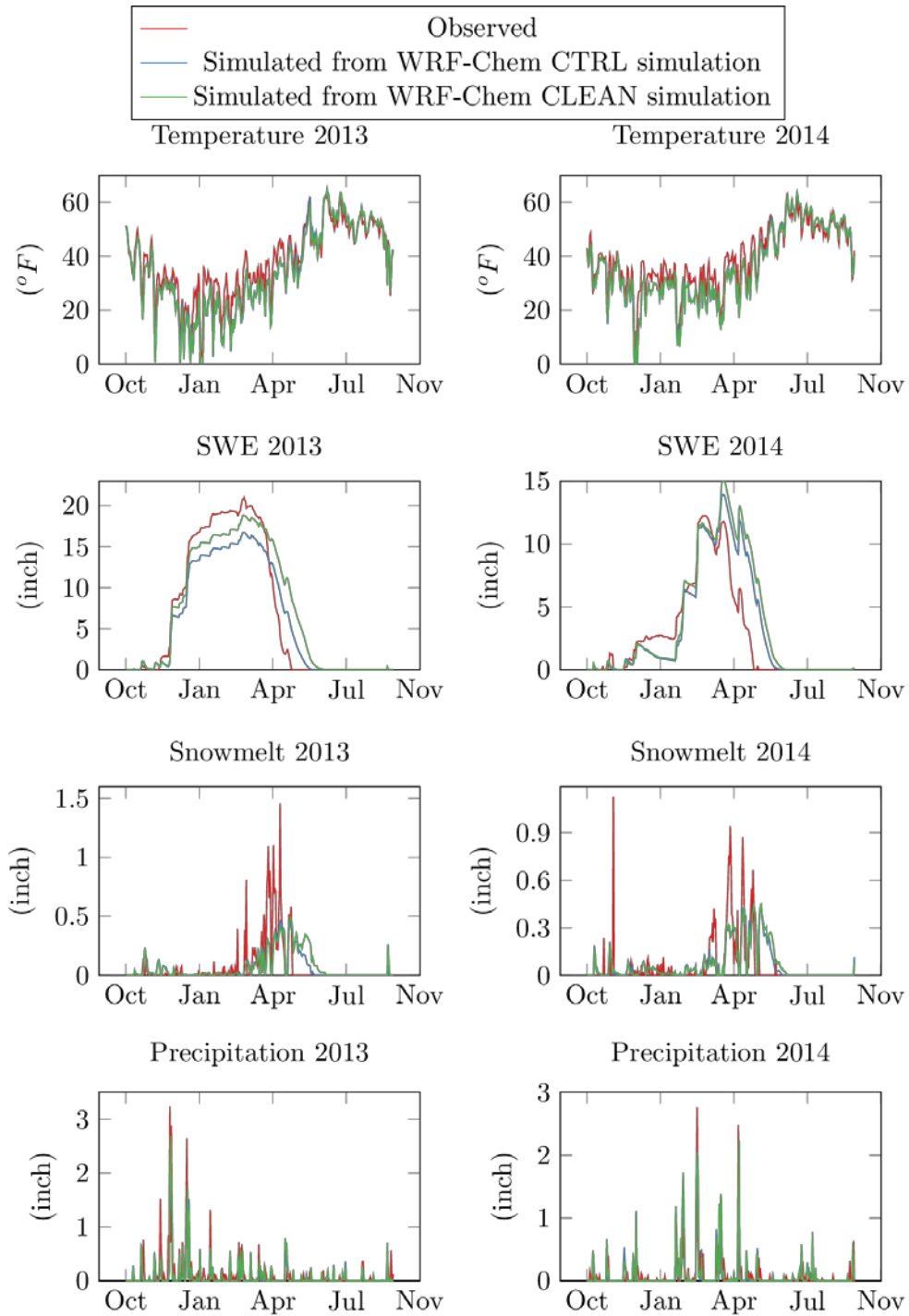
Sensitivity of the dynamic regression model was also performed with respect to number of water years used. Two models were estimated using three and four water years in the training set respectively for both lakes. Water year 2013 and 2014 work as the corresponding testing sets. Parameter estimates of both models are compared for changes in sign. No parameter estimate changes sign between these two simulations for both Florence Lake and Lake Edison. The annual inflow error is 15 percent and 5 percent respectively at Florence Lake and Lake Edison when four water years of data is used in the training set to forecast inflow of water year 2013. Therefore, it can be argued that the model is robust against an increase in the amount of training data.

## **2.7 Quantifying the Impact of Aerosols on Reservoir Inflow**

### **2.7.1 Evaluation of the WRF-Chem Simulation**

The researchers investigate the WRF-Chem model performance in the researchers' region of interest. WRF-Chem CTRL and WRF-Chem CLEAN simulation are WRF-Chem model with and without considering impact of aerosols respectively. As shown in Figure 41 the meteorological variables simulated from the WRF-Chem model are reasonably close to the observed variables. The WRF-Chem model results are highly correlated with the observed meteorological variables for both water years. The correlation coefficients between the observed and WRF-Chem CTRL simulations for temperature and SWE range from 0.88 – 0.97 for 2013. The correlation coefficient for precipitation ranges from 0.66 – 0.73 which is adequate for the researchers' model since it has lesser impact on inflow. Visual inspection and one way ANOVA show that the WRF-Chem model underestimates temperature and precipitation in the researchers' interested region. The model underestimates the SWE from December to March and overestimates the SWE from April to June.

**Figure 41: Comparison of Observed and WRF-Chem CTRL and CLEAN Simulated Meteorological Variables**



Source: University of California, Riverside

The meteorological variables simulated from the WRF-Chem CTRL and WRF-Chem CLEAN models are highly correlated. The RMSE of the simulated meteorological variables with the observed variables are shown in Table 14. It can be observed that the

meteorological variables from the WRF-Chem CTRL simulations are closer to the observed meteorological variables than those from the WRF-Chem CLEAN simulations. In general, temperature from WRF-Chem CTRL simulations is higher than those of the CLEAN simulations because aerosol deposition increases impurity of snow (Wu, et al., 2017b). Precipitation and SWE from WRF-Chem CTRL simulations are lower than the CLEAN simulations. To understand how the aerosols affect these two variables, (Wu, et al., 2017b) the effects of ARI, ACI, and ASI separately and found that ACI plays a dominant role in increasing cloud water but reducing precipitation, leading to reduced SWE. Increase of non-precipitating clouds can be explained by the fact that more CCN are available for the formation of clouds with smaller cloud droplets when more aerosols are present in the atmosphere. More detailed analysis on aerosol impacts on precipitation and snowpack in the researchers' region of interest can be found in (Wu, et al., 2017b). Higher temperature, snow albedo effect and feedback lead to higher snowmelt with aerosols in the late spring. However, snowmelt is lower with aerosols during early/late summer because of lower prior season's SWE and higher snowmelt in the late spring. From the correlation coefficient of WRF-Chem CTRL and CLEAN simulations, and ANOVA, the difference between the simulated SWE and precipitation in the CTRL and CLEAN simulations is larger in 2013 compared to 2014. In other words, the impact of aerosols on these meteorological variables is stronger in 2013.

**Table 14: RMSE of WRF-Chem Simulated Meteorological Variables with Respect to Observed Variables**

Year	Simulation	Temperature ( <i>F</i> )	SWE (inch)	Precipitation (inch)
2013	CTRL	4.86	2.10	0.20
	CLEAN	4.91	2.61	2.61
2014	CTRL	5.78	2.48	0.23
	CLEAN	5.93	2.85	0.25

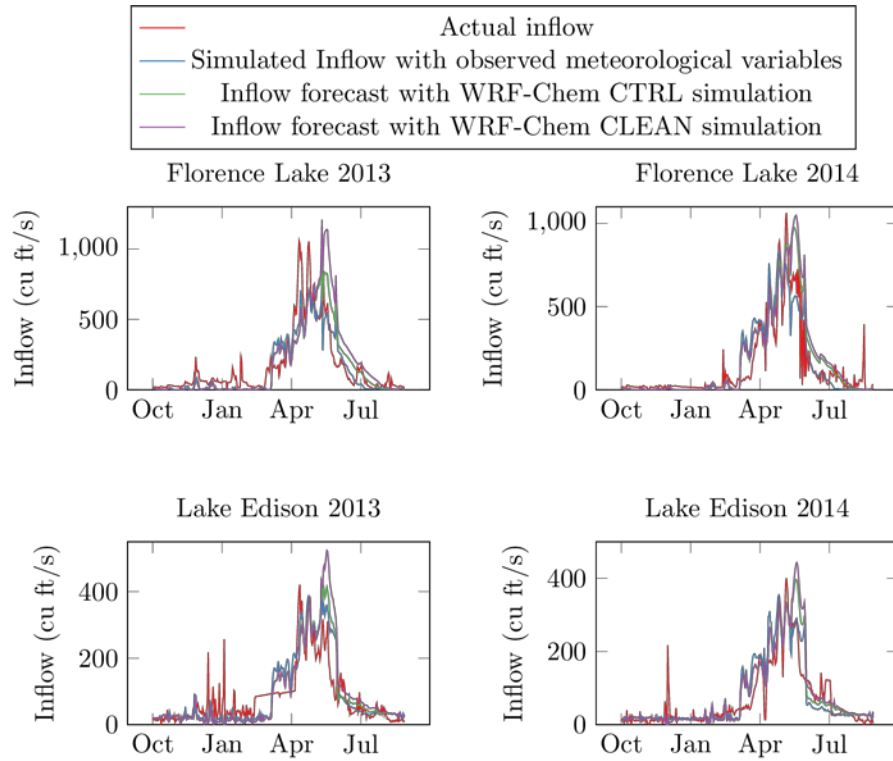
Source: University of California, Riverside

### 2.7.2 Quantification of the Impact of Aerosols on Reservoir Inflow

The impact of aerosols on reservoir inflow was quantified for two water years 2013 and 2014. To quantify the impact of aerosols on inflow, the researchers ran dynamic regression model using the meteorological variables simulated from the WRF-Chem CTRL and CLEAN models as inputs of the testing data set. The actual inflow (red) is compared with simulated inflow from observed meteorological variables (blue) and WRF-Chem simulated meteorological variables (green and purple) in Figure 42. The inflow simulated by the meteorological variables from the CTRL simulations match well with the actual inflow. The difference in inflow between the CTRL and CLEAN simulations  $Inflow_{CTRL} - Inflow_{CLEAN}$  represents the impact of aerosols, which is plotted

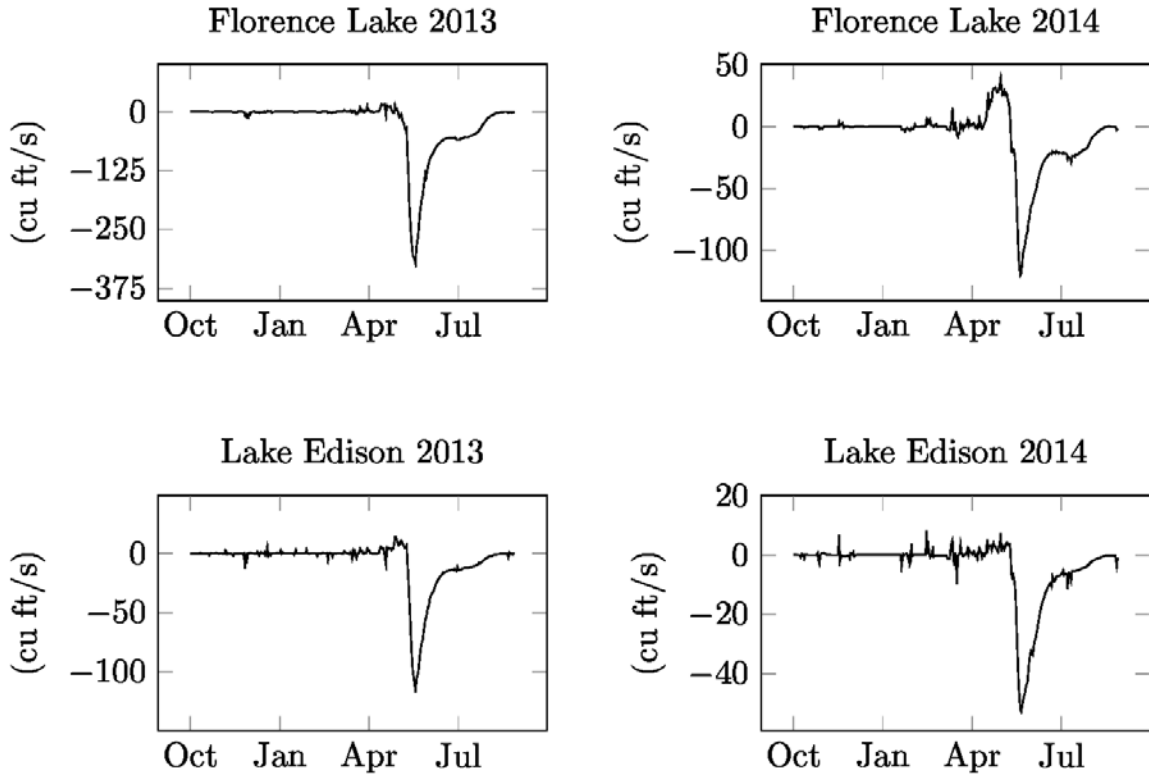
in Figure 43. The observed inflow and meteorological data for 2010-2012 are used as the training set while simulating inflow for water year 2013.

**Figure 42: Comparison of Actual Inflow, Simulated Inflow from Observed Meteorological**



Source: University of California, Riverside

**Figure 43: The Impact of Aerosols on Reservoir Inflow  $Inflow_{CTRL} - Inflow_{CLEAN}$  Variables**



Source: University of California, Riverside

It can be observed that for the same year, the impact of aerosols on inflow is consistent in direction and similar in magnitude in both lakes. After simulating inflow for both water years under CTRL and CLEAN conditions, annual and seasonal inflow with and without considering the impact of aerosols were calculated. The impact of aerosols on inflow into reservoirs was then calculated by Equation (2.10)

$$\frac{Inflow_{w/Aerosols} - Inflow_{w/o\ Aerosols}}{Inflow_{w/o\ Aerosols}} \times 100\% \quad (2.10)$$

The impact of aerosols on annual and seasonal inflow are tabulated in Table 15. For seasonal analysis, the researchers first define the four seasons- fall is defined as the period of 10/01-12/21, winter is defined as 12/22-03/20, spring is defined as 03/21-05/31, and summer is defined as 06/01-09/30.

In general, aerosols lead to slightly higher inflow in the late spring and significantly lower inflow during summer (11 to 26 percent reduction) as seen from Table 16. These results can be explained by the seasonal variation of the impact of aerosols on the meteorological variables. During spring, the presence of aerosols leads to higher temperature and snowmelt, which translate into a higher inflow. On the other hand, aerosols lead to lower precipitation which results in a small reduction in the inflow. The

aggregated effect of aerosols on inflow through temperature, snowmelt, and precipitation is slightly higher inflow in the spring. Lower prior season's SWE and lower current season's snowmelt together with lower precipitation result in lower inflow in summer. The presence of aerosols suppresses the precipitation, which leads to lower inflow for the Florence Lake during fall and winter. In the Lake Edison, inflow in fall and winter is simulated using precipitation and temperature. Aerosols lead to lower precipitation and higher temperature, which translate into lower inflow in fall and slightly higher inflow in winter. The overall effect of aerosols is a reduction in annual inflow by 4 to 14 percent for both lakes as shown in Table 16.

The impact of aerosols is more significant in water year 2013 than in water year 2014 for both lakes. This is because the impact of aerosols on the meteorological variables is more pronounced in water year 2013 as seen from the mean of the meteorological variables from CTRL and CLEAN simulations. The annual impact of aerosols is stronger in Florence Lake. This is because the fall and winter inflow are simulated using only precipitation for Florence Lake. For Lake Edison, the fall and winter inflow is simulated using both precipitation and temperature. The higher temperature effect from aerosols offsets some of the reduction in inflow in Lake Edison. Therefore, the annual impact of aerosols on inflow is lower in Lake Edison.

**Table 15: Annual Reservoir Inflow Under Different Aerosol Conditions.**

Lake	Year	Actual ( <i>acre ft</i> )	CTRL( <i>acre ft</i> )	CLEAN( <i>acre ft</i> )
Florence	2013	117390	113610	13163
	2014	99980	11974	12541
Edison	2013	58572	61004	66240
	2014	49339	55446	58247

Source: University of California, Riverside

**Table 16: Impact of Aerosols (%) on Annual and Seasonal Reservoir Inflow**

Lake	Year	Annual	Fall	Winter	Spring	Summer
Florence	2013	-14%	-11%	-5%	-.01%	-26%
	2014	-4%	-2%	-1%	2%	-11%
Edison	2013	-8%	-1%	0.2%	1%	-18%
	2014	-5%	-0.4%	0.3%	0.6%	-11%

Source: University of California, Riverside

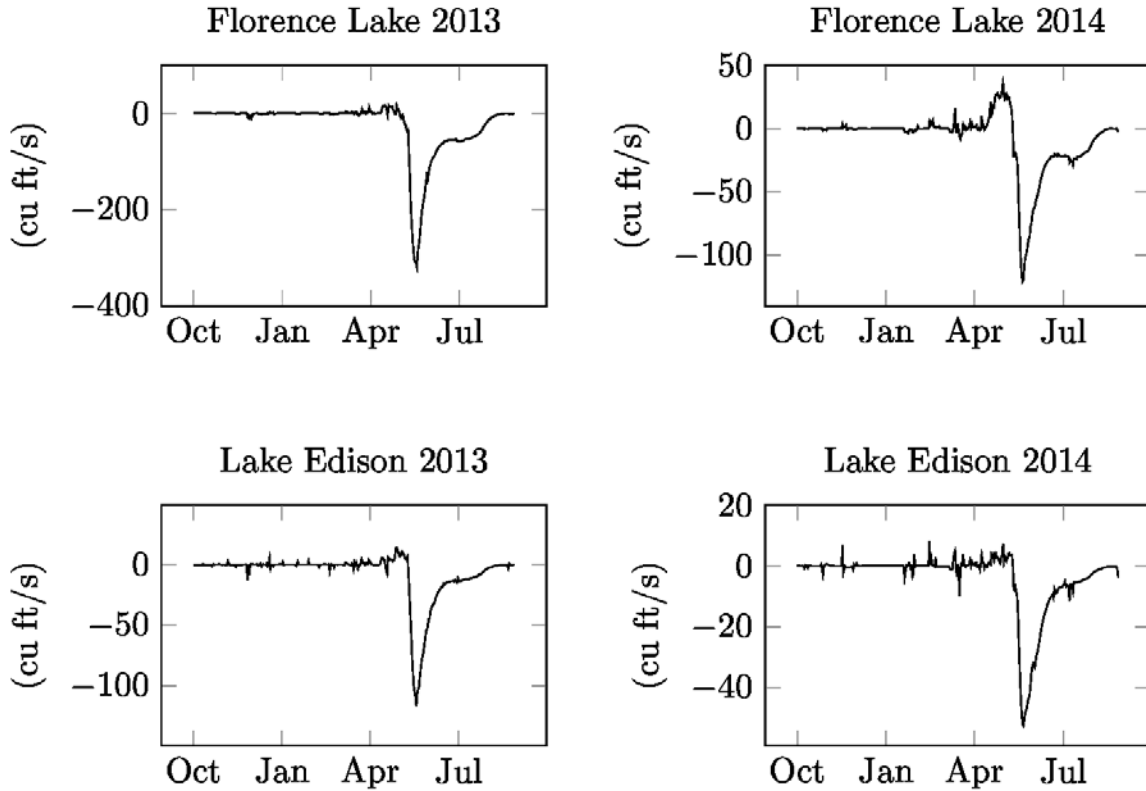
### 2.7.2.1 Quantifying Impact of Aerosols With Perturbed Inputs

Though the impact of aerosols on inflow is consistent in sign for all the seasons at both lakes for water years 2013 and 2014, it can be observed that the difference between CTRL and CLEAN inflow is small. The most significant impact occurs in the late spring and summer when the WRF-Chem simulations of SWE have a large error. Therefore, forecasts of inflow in water year 2013 and 2014 and the impact of aerosol on inflow were calculated with perturbed testing set inputs to gain more confidence in the impact of aerosol results. To account for the discrepancy between the observed meteorological variables and WRF-Chem CTRL simulation outputs, the difference between these two time series was calculated for all of the meteorological variables. A random error was introduced to the daily values of the meteorological variables of the WRF-Chem simulated testing set. To preserve the temporal correlation of the meteorological variables, a random variable following uniform distribution in the interval [0, 1] was multiplied with  $X_{obs} - X_{WRF-Chem\ CTRL}$  where  $X$  denotes meteorological variables. The resultant random error was added to the meteorological variables of the testing set to generate the perturbed inputs. Both CTRL and CLEAN simulations were perturbed by the same error. Input meteorological variables of the training set are not perturbed. The dynamic regression model was then simulated with the perturbed WRF-Chem CTRL and CLEAN testing sets for Florence Lake for both water years. 1,024 model runs were performed in the same fashion as Section 2.6.3.6. Out of the 1024 models, the model, which produced the median RMSE, was selected for analysis of results. The difference in inflow between the CTRL and CLEAN simulations was then calculated and plotted in Figure 44 for the selected model.

Table 17 presents a comparison of the impact of aerosols on annual and seasonal reservoir inflow for the reference and selected perturbed input model scenarios. It can be observed that, for all of the simulations, the sign and magnitude of the difference in inflow with the selected perturbed input model are similar to the reference model. Here, the reference model denotes the unperturbed input model.

Therefore, it can be safely argued that the difference between the inflows arise from the difference between meteorological variables with and without impact of aerosol.

**Figure 44: The Impact of Aerosols on Reservoir Inflow ( $Inflow_{CTRL} - Inflow_{CLEAN}$ ) for the Selected Perturbed Input Model with Median RMSE**



Source: University of California, Riverside

**Table 17: Comparison of Impact of Aerosols on Annual and Seasonal Reservoir Inflow for the Reference and Selected Perturbed Input Model with Median RMSE**

Lake	Year		Annual	Fall	Winter	Spring	Summer
Florence	2013	Reference	-14%	-11%	-6%	-.07%	-26%
		Perturbed	-13%	-10%	-5%	0.05%	-23%
	2014	Reference	-4%	-2%	-1%	2%	-11%
		Perturbed	-4%	-0.10%	-0.09%	2%	-10%
Edison	2013	Reference	-8%	-1%	0.2%	1%	-18%
		Perturbed	-8%	-1%	0.1%	1%	-17%
	2014	Reference	-5%	-0.4%	0.3%	0.6%	-11%
		Perturbed	-5%	-0.2%	0.4%	0.7%	-10%

Source: University of California, Riverside

## 2.8 Summary and Conclusion

The research team developed a comprehensive framework to quantify the impact of aerosols on reservoir inflow by synergistically combining the WRF-Chem model and a dynamic regression model. The dynamic regression model can also be leveraged to perform one-year ahead daily inflow forecast. The team conducted a case study using Florence Lake and Lake Thomas Alva Edison of the Big Creek Hydroelectric Project. The dynamic regression model was found to be adequate and performed well compared to the benchmark models. The researchers investigated the impact of aerosols on the inflow into these hydropower reservoirs over two water years. The simulation results show that the presence of aerosols significantly reduces the annual inflow into the hydropower reservoirs of the Big Creek Hydroelectric Project. Moreover, aerosols significantly reduce the amount of inflow in the summer when the marginal economic value of water is extremely high. The presence of aerosols also slightly increases the inflow in the spring when the run-off risk is high. Therefore, it can be concluded that, the presence of aerosol is detrimental to the optimal utilization of hydroelectric power systems. The change in inflow due to impact of aerosol in different seasons with different water and electricity demands can assist the reservoir operators in determining the optimal operation policy for the reservoirs. Further scarcity of reservoir inflow during dry seasons can motivate the San Joaquin River region water resources planners to focus their efforts on mitigation strategies. The findings from this research can provide another justification for stricter environmental regulations to reduce anthropogenic aerosol emissions.

Forecast of the inflow into the hydropower reservoirs obtained from this study can assist in optimizing the cascaded hydropower system. In the future, the researchers plan to integrate the year ahead inflow forecast of Florence Lake and Lake Edison into the long-term scheduling of the Big Creek Hydroelectric Project. The impact of aerosols on hydroelectric generation and economic value will be assessed. Future studies will also address the drawbacks of the study. The limited historical reservoir inflow data prevented the researchers' model from capturing long-term trends in reservoir inflow due to changes in the level of aerosols in the atmosphere. Reservoir inflow data from 2015 onwards will be available and they will be used to forecast reservoir inflow for water year 2017 onwards and quantify the impact of aerosols on reservoir inflow.

# CHAPTER 3:

## Impact of Aerosol on Hydropower Generation

---

### 3.1 Introduction

Hydropower is an important source of electricity generation accounting for one third of the renewable generation. In 2016, hydro-produced electricity accounted for 14.62 percent of California's total system power. Here, the amount of hydroelectricity generation varies each year and is largely dependent on snowmelt runoff and rainfall. Due to their head potential and snow storage, higher elevation basins in the Sierra Nevada Mountains count for almost 50 percent of the hydroelectricity produced in California (Aspen Environmental and M-Cubed 2005). Big Creek Hydroelectric System owned and operated by Southern California Edison is located in the upper San Joaquin River system in the high altitudes of the Sierra Nevada Mountains producing about 12 percent of the California's total hydroelectricity generation. It is a cascaded hydropower system with multiple artificial reservoirs, long tunnels, steel penstocks and powerhouses.

In a storage scheme hydropower plant, reservoir inflow has a strong relationship with the power generated and profit earned by the generation company (GENCO) as hydropower production is inherently reliant on reservoir storage or head for energy production. The reservoirs in the Big Creek Hydroelectric system are filled during the spring run-off in April mainly from melting snow. Though inflows into these reservoirs are snowmelt dominated, they are also influenced by other meteorological variables such as temperature and precipitation. Natural and anthropogenic aerosols have a great influence on temperature, snow water equivalent and precipitation and thus influences inflows into the reservoirs. In the simulation results of the previous chapter, it has been shown that aerosols have an impact on precipitation, snow water equivalent and snowmelt leading to a significant reduction of annual reservoir inflow by 4 to 14 percent in Lake Thomas A. Edison and Florence Lake of the Big Creek Hydroelectric system. Since hydropower generation is inherently dependent on reservoir inflow, aerosols ultimately influence hydropower production and profit earned by the generation company (GENCO).

The primary objective of this study is to calculate the impact of aerosols on the hydropower generation in the Big Creek Hydroelectric System and to subsequently calculate the impact of aerosols on total profit earned by Southern California Edison from the Big Creek Hydroelectric System. Inflow forecasts into Lake Thomas A. Edison, Florence Lake, Bear Diversion, Huntington Lake, Mammoth Lake, Redinger Lake and Shaver Lake of the Big Creek Hydroelectric System are calculated with and without considering the impact of aerosols for water year 2015. The inflows are then fed into

the long-term hydro Vista Decision Support System in a one-year time horizon to maximize the profit generated from the hydropower production in the hydroelectric system. Vista Decision Support System is a toolbox to assist in both planning and operations of the hydroelectric systems to maximize the value of water resources and power generation and market activity.

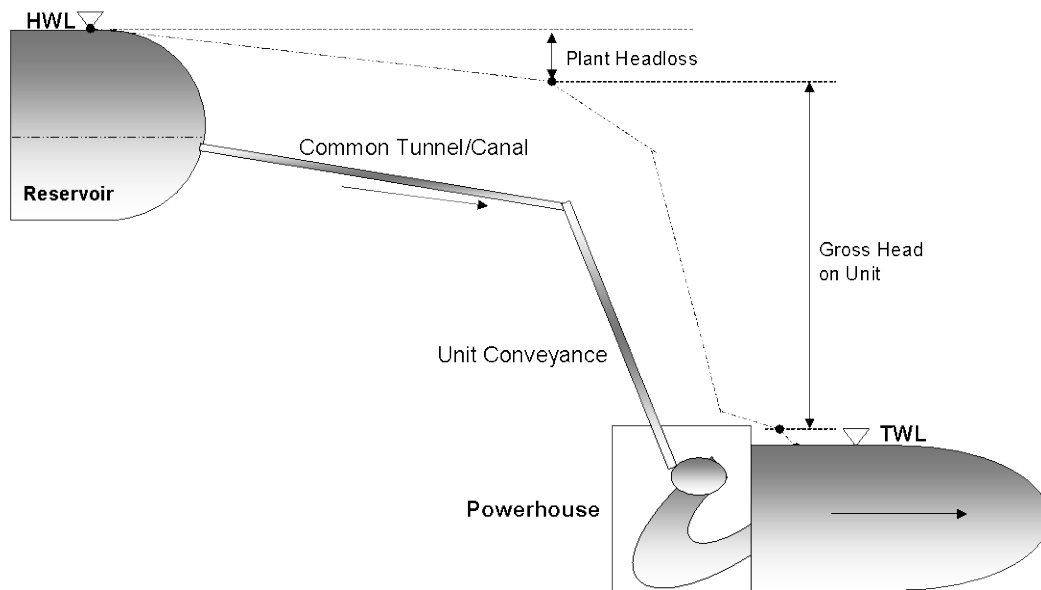
The unique contribution of this study is that the researchers have developed a comprehensive framework for evaluating the impact of aerosols on hydropower generation and subsequent profit earned that seamlessly integrates numerical weather forecasting model (WRF-Chem), statistical inflow forecast model, and the hydro Vista Decision Support System. The simulation results show that aerosols significantly reduce hydropower generation by 89356 MWH in water year 2015, which is a 5.61 percent reduction in the annual hydropower generation. The presence of aerosols subsequently causes a staggering \$2.8 million loss in revenue in a water year for Southern California Edison.

The remainder of this chapter is organized as follows. Section 3.2 describes hydropower plants, Section 3.3 discusses the Big Creek Hydroelectric Project in detail, Section 3.4 describes the Vista DSS, Section 3.5 presents the methods used in this study for integrating the inflow forecast results and the Vista DSS, Section 4.6 shows the impact of aerosols on hydropower generation and revenue earned from the Big Creek Hydroelectric System and finally, Section 3.7 concludes the chapter.

## **3.2 Hydropower Plant**

Hydropower plants capture the potential energy of falling water to generate electricity where a turbine converts the kinetic energy of falling water into mechanical energy and a generator converts the mechanical energy from the turbine into electrical energy. The potential difference is captured at a location by constructing dams on rivers. Typical components of a hydroelectric plant are a dam or barrage, a head-race water conveying system like a conduit called penstock or an open channel to transport water from the reservoir to the turbines, turbines coupled to generators and tailwater discharge conduit that conveys the water out of the turbine to the river. The potential energy difference is determined by the difference between the headwater and tailwater level subtracted by the head losses from entrance, trash rack, conduit friction, bend, contraction, split and exit losses. The most common turbines are Kaplan, Francis, and Pelton wheel designs. A hydropower plant is shown in Figure 45

**Figure 45: Hydropower Plant Representation**



Source: University of California, Riverside

### 3.3 Big Creek hydroelectric Project

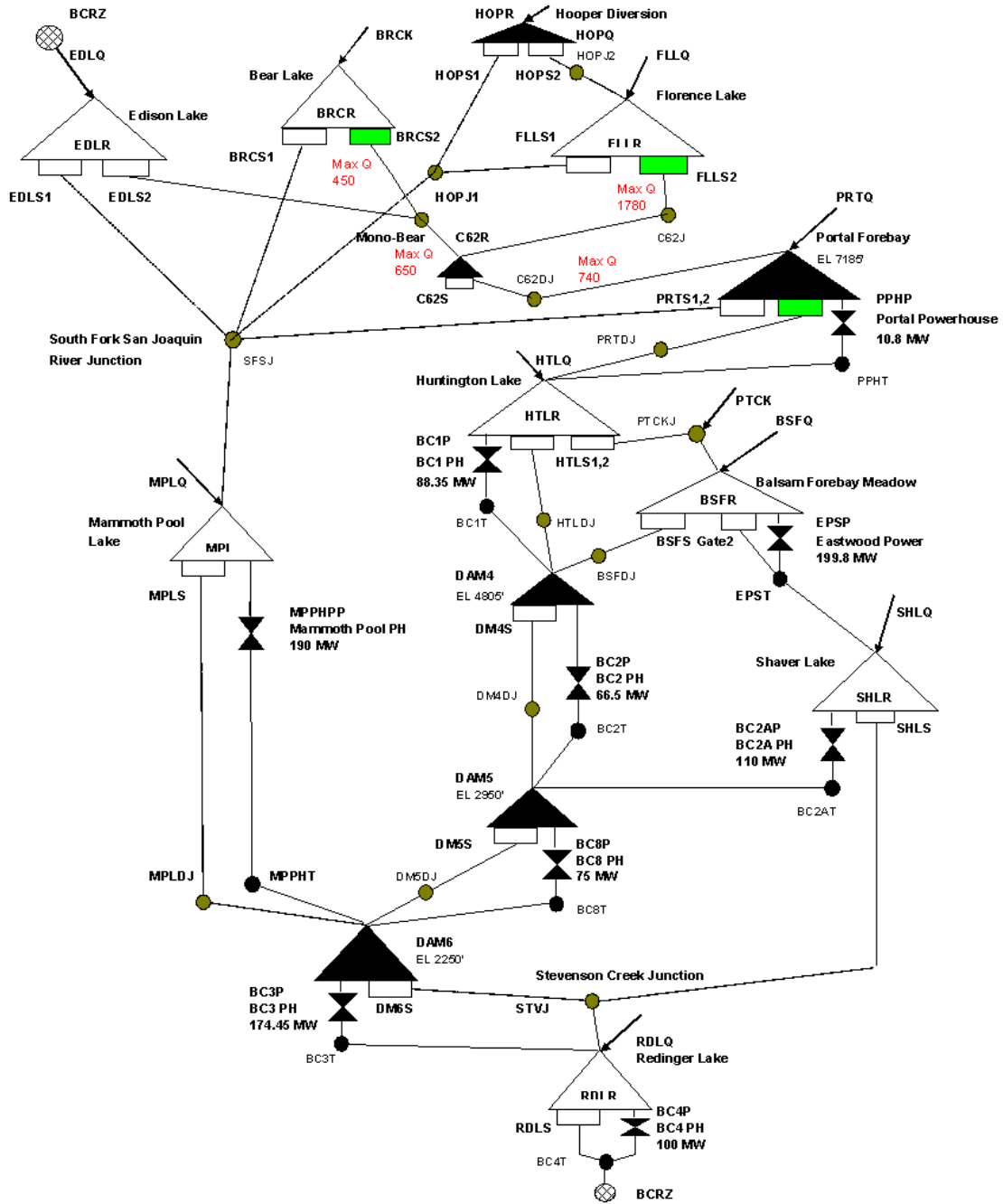
The Big Creek Hydroelectric Project is an extensive cascaded hydroelectric system that accounts for 12 percent of California's total hydroelectric generation. The project is located on the upper San Joaquin River system in the high altitudes of the Sierra Nevada Mountains of Central California.

The hydroelectric project is owned and operated by Southern California Edison (SCE), which has a total installed capacity of 1000 MW accounting for approximately 20 percent of SCE's total generation capacity. The hydroelectric system includes 27 dams, 23 generating units in nine powerhouses, miles of underground tunnels, and six major reservoirs with a combined storage capacity of 560,000 acre feet. Water from lakes in higher elevation are routed through the nine powerhouses and discharged to lakes in lower elevations that are connected through tunnels and penstocks. The water travels a combined vertical distance of 6,655 feet before being discharged through the last powerhouse into the San Joaquin River.

Florence Lake and Lake Thomas Alva Edison are the higher elevation reservoirs of the system having spillway elevation of 7327 and 7642 feet respectively. The dam at Florence Lake captures runoff from the South Fork San Joaquin River, diverting it through the Ward Tunnel towards the Portal Powerhouse, which is the first powerhouse in the system to receive water. Florence Lake has a storage capacity of 64,406 acre feet. Lake Thomas Alva Edison is formed by the Vermillion Valley Dam constructed across the Mono Creek, a tributary of the South Fork of the San Joaquin River. It has a 123,035 acre-foot storage capacity. It discharges some of its water to the Ward Tunnel and

thereby further regulates the water supply to the Portal Powerhouse. Portal Powerhouse has one 10,000 KW unit of the Francis type. Water running through Portal Powerhouse is discharged into the Huntington Lake where it is in turn diverted to Big Creek Powerhouse No. 1 constituting a drop of 2100 feet. This powerhouse has four double overhung impulse turbines having a total capacity of 81,000 KW. The water can also be diverted to the Eastwood Power Station and into Shaver Lake from Huntington Lake, constituting a drop of 1700 feet. Shaver Lake reservoir is the largest reservoir of the Big Creek hydroelectric System having an operating capacity of 135,283 acre-feet and a spillway elevation of 5,370 feet. The water drops another 1900 feet from big Creek Powerhouse No. 1 to Big Creek Powerhouse no 2. Adjacent Big Creek Powerhouse 2A receives water from Shaver Lake exclusively for the operation of two double overhung impulse turbines having a combined capacity of 96,000 KW. The combined operating capacity of these two plants in 162,000 KW. Water from these two powerhouses is discharged to a common afterbay and after that drops another 800 feet to Big Creek Powerhouse No. 8. This powerhouse consists of two vertical Francis-type reaction turbines having a total operating capacity of 58,000 KW. Mammoth Pool reservoir formed by a dam built across the San Joaquin river feeds water to the Mammoth Pool Powerhouse through an eighth-mile tunnel and penstocks. Water from the mammoth Pool Powerhouse and Big Creek Powerhouse no. 8 drops another 800 feet through Big Creek Powerhouse no. 3 after being discharged to a common afterbay. The water is then discharged to Redinger Lake, the smallest reservoir in the Big Creek Hydroelectric System from where the water drops a final 400 feet through Big Creek Powerhouse No.4 and is discharged to the San Joaquin River. A schematic of the project is provided in Figure 46.

Figure 46: Big Creek Hydroelectric Project Schematics



Source: University of California, Riverside

### 3.4 Hydro Vista Decision Support System

Hydropower's fast response characteristic makes it a suitable candidate to meet peak electricity demand, which commands a higher price per kilowatt-hour so its value can therefore be further enhanced by participating in multiple energy markets. To maximize benefit from hydropower generation, efficient scheduling of available energy resources as per load demand is an important task in modern power systems, which calls for optimal scheduling of hydropower reservoirs. Two important objectives in a hydropower system are to generate during periods when electricity demand is high and energy has high price and to minimize necessary spilling (water is released without producing hydropower). In California, peak energy demand occurs during summer and most spillages are carried out during the spring months, which is the runoff period indicating reservoir refilling period. Spillage can also occur in winter. Moreover, hydropower reservoirs often have multiple additional functions such as flood control, navigation, irrigation, water supply, recreation etc. that often pose potentially conflicting objectives.

These tasks are performed by Hydro Vista Decision Support System, which is a toolbox to assist in both planning and operations of the hydroelectric systems to maximize the value of water resources and power generation and market activity. It also helps determine long-term storage planning and management and assists in both short and long-term planning and scheduling of generation and real-time dispatch. The system's capacity to plan encompasses right from the inflows into the reservoirs to the ultimate goal of revenue generation from the power generation. However, the Vista DSS does not control system operations, rather human staffs control them. It also helps run analyses to investigate alternative operation policy, outage schedules, system upgrades or development.

At Big Creek Hydroelectric System, Vista DSS is used in day ahead market optimization, medium term water management and prompt month analysis of Hoover Contract. The Long-term optimization goals are to develop the best schedule of generation, water releases and transactions in default one-year time horizon while meeting various physical and operational constraints. The short term optimization goals are the same with time horizon of several hours to two week. The optimization is driven by inflow, load and transactions.

The hydraulic system of the hydroelectric system and the transmission system are represented in the Hydro Vista DSS for different scenarios consisting of different configuration cases and data cases. Facility data are used to describe the physical structures in a river system such as reservoir and hydro plants to represent the hydraulic system. Different scenarios are built using different configuration cases, facility case, outages cases, different water resource operational constraints cases, transmission operational constraint cases, LTGS hydrology sequences, different short-term inflow cases, load forecast cases, xchange cases and energy cases. There are nine integrated modules to perform these tasks, which includes two data management

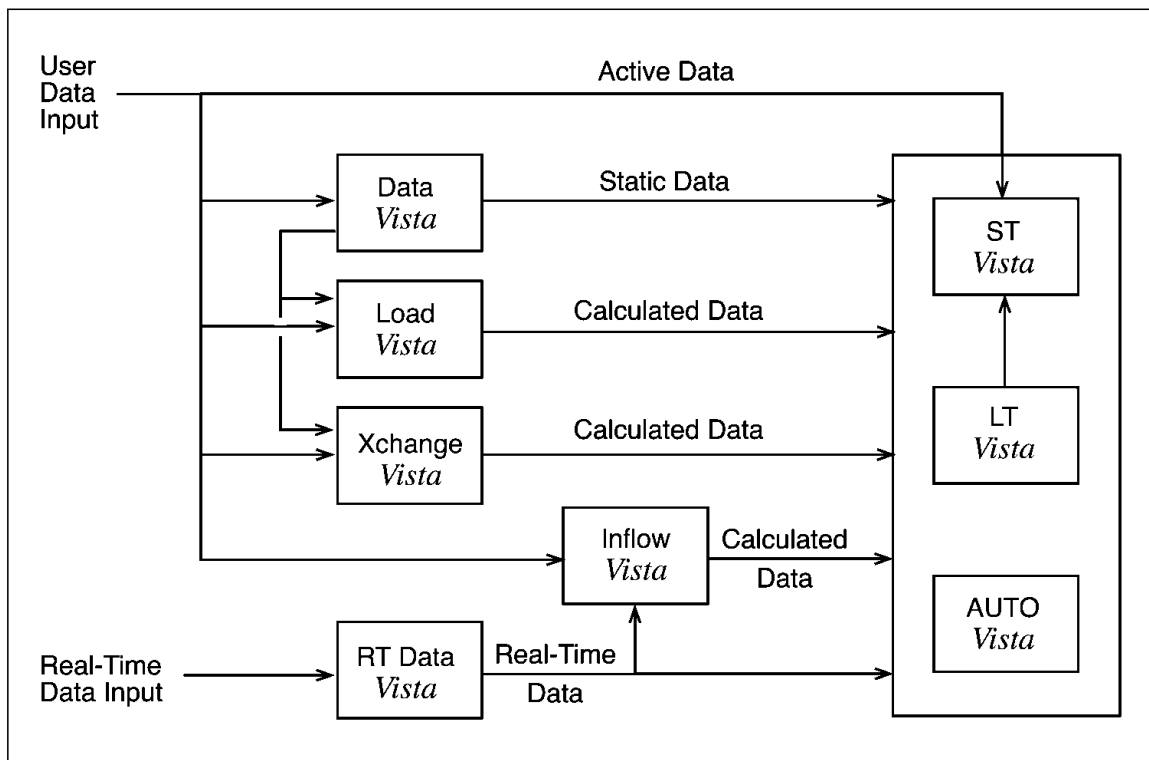
modules for set-up, and data input, three analysis and forecasting modules, two operations optimization modules for scheduling and planning, a study module and a report module.

### 3.4.1 Vista Modules

#### 3.4.1.1 Data Management Modules

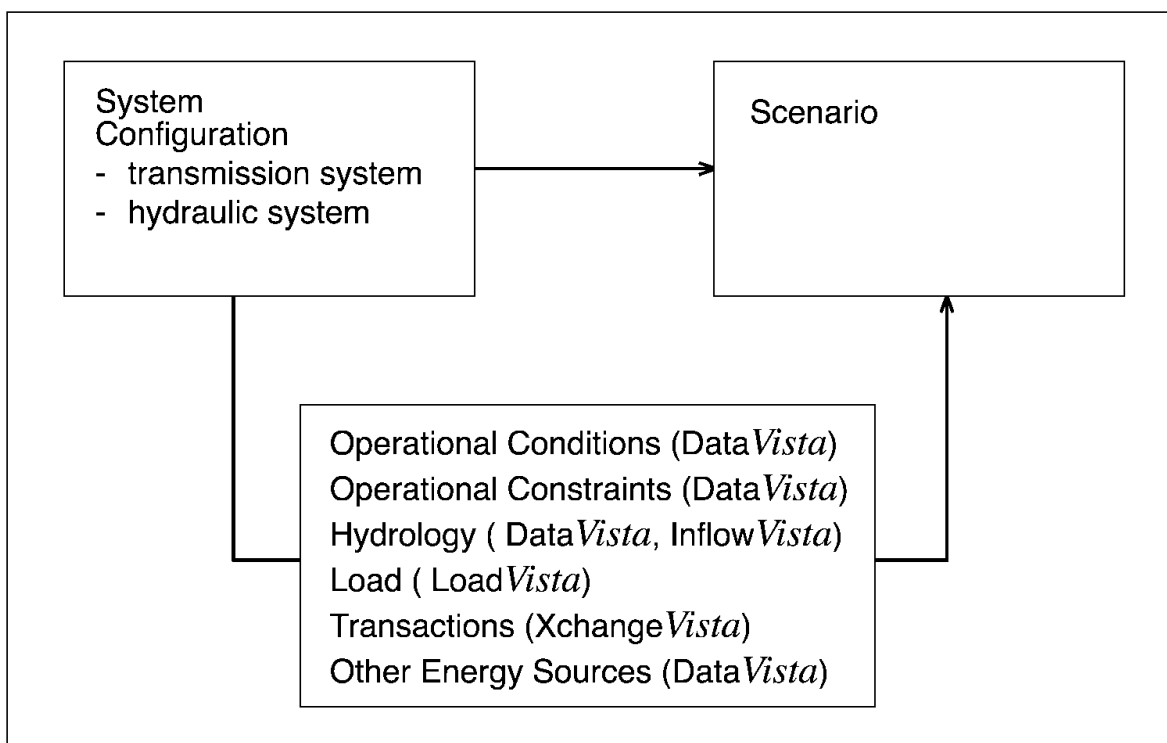
Facility and operational data are required in the Vista DSS. Vista DSS requires both static and dynamic data. Static data are defined as part of system setup. They include system description, plant/unit characteristics, transmission system configuration, Hydro license and constraints. On the other hand, dynamic data examples are unit generation and discharge, water levels, outage schedules, price forecasts, load forecasts and thermal production costs. The data management modules are Data Vista for handling and accessing static system data and RT Data Vista for accessing and analyzing real-time data respectively, Xchange Vista for defining transaction opportunities to purchase or sell energy. Vista services is used for downloading real-time data from SCADA, outages, price forecasts, load forecasts and dispatchable thermals. It is also used to calculate actual project inflows and inflow forecasts. Data are downloaded automatically at user-specified intervals. Vista Data Relationships are shown in Figure 47. Subsequently Vista Data Input is shown in Figure 48.

**Figure 47: Vista Data Relationships**



Source: University of California, Riverside

**Figure 48: Vista DSS Data Input**



Source: University of California, Riverside

#### 3.4.1.2 Analysis and Forecasting Modules

Analysis and forecasting modules include Inflow Vista for defining and deriving inflow forecasts and Load Vista to download and derive energy-demand forecasts. Inflow forecasts are needed to generate long-term inflow scenarios, short-term generation scheduling and flood management.

#### 3.4.1.3 Planning and Scheduling Modules

Operations optimization modules consist of LT Vista for medium to long-term water storage and energy-generation management that guides water operations, hydrothermal generation and energy transactions, ST Vista for short-term energy generation and transaction scheduling, and RT Vista for real-time energy dispatch. LT Vista has default time horizon of one year. It can also be user defined, from several weeks to several years. The optimization has a weekly time step or user defined variable daily blocks. ST Vista has a time horizon of several hours to two weeks. It has three analysis tools- optimization, simulation and simulation with constraints. Optimization considers all constraints and transaction and is driven by inflow, load and transactions. On the other hand, simulation does not consider constraints and transaction and is defined by inflow and user-defined generation and spill. Simulation with constraints considers constraints, but does not consider transactions. It is driven by inflow, user-defined generation and spill, and reservoir and tailwater elevations.

#### 3.4.1.4 Study and Report Module

AUTO Vista in study module analyzes detailed system operations for multiple hydrological scenarios where the periods of study can extend from one to many years. The results are evaluated statistically. Report Vista can generate reports related to operation and scheduling e.g. FERC compliance reports, CPUC compliance reports and internal standard reports like generation to data, water management and after the fact efficiency reports.

### 3.5 System Representation

Hydroelectric system representation is an integral part of the Vista DSS. The system representation is discussed in this section.

#### 3.5.1 Physical System Representation

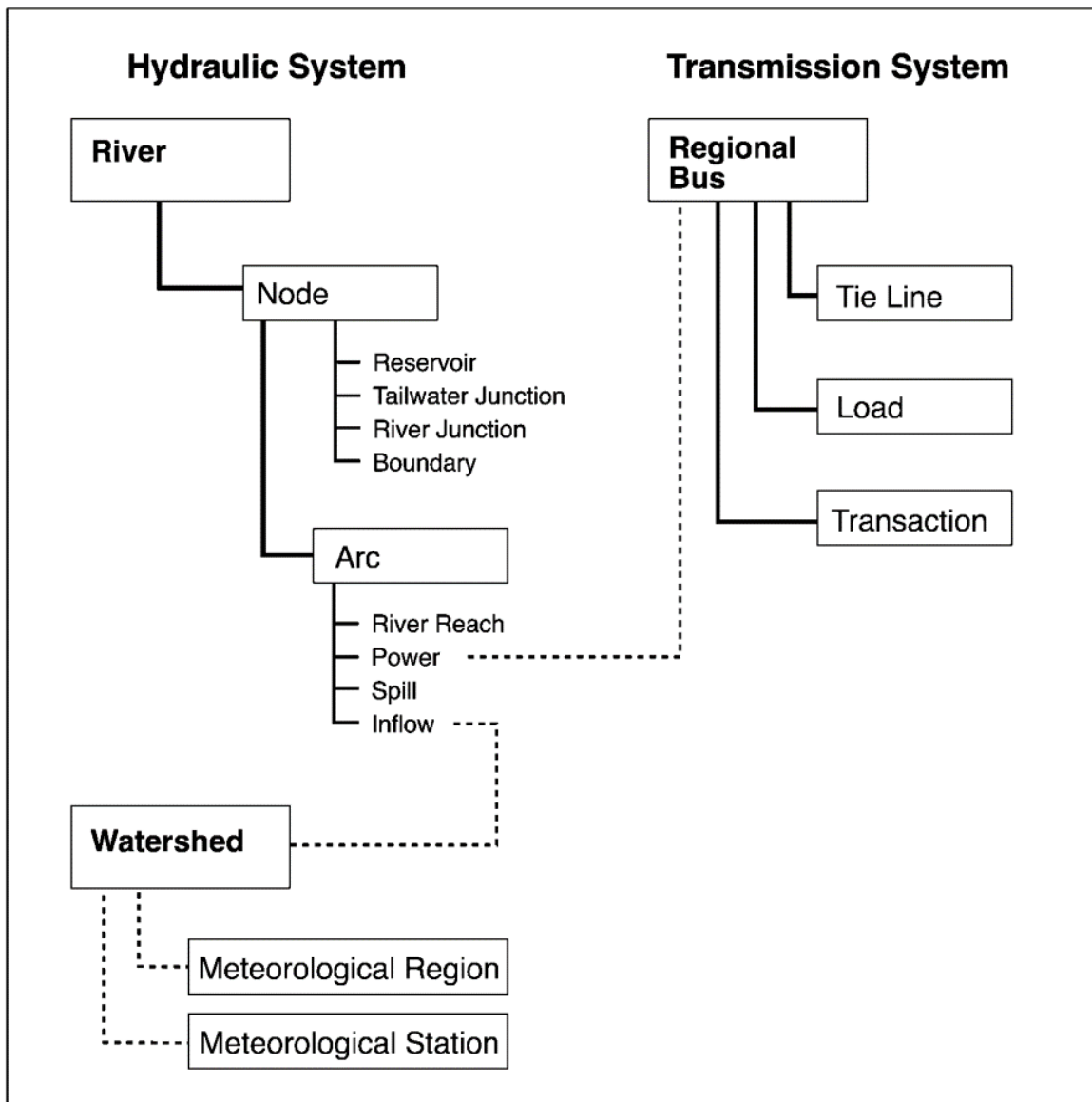
A hydropower system has hydraulic system components. For modeling purposes, a water resource system can be disaggregated into a number of hydraulically independent basins. A hydraulic system consists of River and Watersheds. Rivers can be single, multiple uncoupled and multiple coupled. Each river system can be represented by a schematic comprising nodes and arcs as shown in Figure 49.

Nodes are points of interest in the water resource system being modeled, such as reservoir, tailwater junction, river junction, source and sink and arcs. Reservoir and river junction nodes combine a number of inflow and outflow channels in the network. Reservoirs nodes have storage associated with them where as river junction nodes do not. Tailwater junction nodes are similar to river junction nodes with an additional important function to sum outflows from generation plant and spillways and yield a river water level that works as a tailwater level to compute generation plant head. Source node supplies water to an arc while a sink node demands water from an arc.

An arc is a directed line segment that joints an upstream node to a downstream node. The direction of flow is defined from the upstream node to the downstream node. There are four types of arcs- inflow, power, spillway and river reach. Inflow arcs represent inflow into the river system to be modeled and are typically a local inflow or tributary, power arcs represent one or more turbines and their associated flow, spillway arcs represent the total flow through one or more spillway structures that flow to a common node and river reach arcs indicate physical conveyances such as natural or manmade channels. Figure 50 illustrates the system schematic of a single river single reservoir.

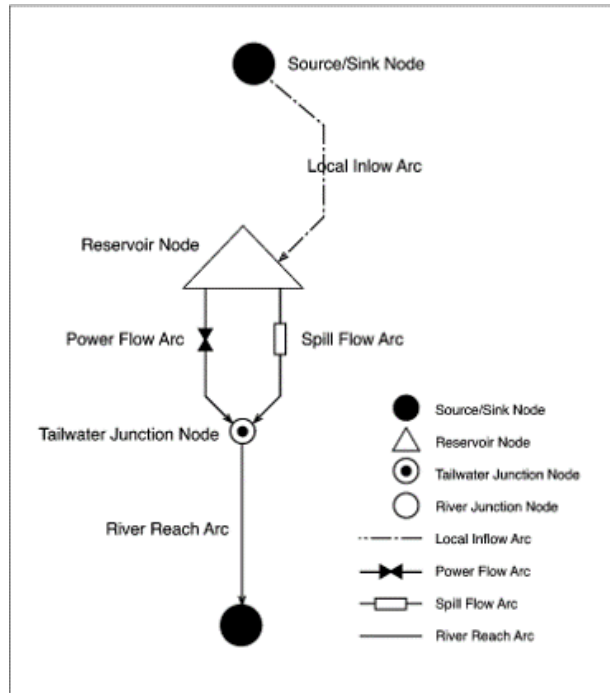
Facility data are used to describe the physical structures in a river system such as reservoir and hydro plants. They are represented mathematically along with estimated parameters. On the other hand, operational data are used to represent the conditions under which a river system operates including regulatory control.

Figure 49: System Representation of Hydro Vista DSS



Source: University of California, Riverside

**Figure 50: Schematic of a Single River Single Reservoir**



Source: University of California, Riverside

### 3.5.1.1 Reservoir Representation (Elevation Volume Relationship)

In Vista DSS, a storage reservoir is represented by its full supply level (FSL), dead storage level (DSL) and the coefficients of the polynomial defining the storage elevation-volume relation. The elevation-volume relationship is represented by the following equations in the Vista DSS:

$$S = C_0 + C_1 \times (EL + C_2)^{C_3} \quad (3.1)$$

when storage is a function of headpond elevation only

$$S = C_0 + C_1 \times (EL + C_2)^{C_3} + C_4 \times Q^{C_5} \quad (3.2)$$

when storage is a function of both the headpond elevation and the inflow to the headpond where

$S =$  headpond storage in cfs-hr or cms-hr

$EL =$  headpond elevation corresponding to  $S$  in ft or m

$Q =$  inflow to the headpond in cfs or cms

$C_0, C_1, C_2, C_3, C_4, C_5 =$  equation coefficients

To derive the elevation volume relationship, elevation and corresponding volume for a series of points spanning the maximum possible operating range of the headpond or reservoir is required. The elevation-volume data should cover the operating range of the

reservoir, up to the dam crest elevation at a minimum. The given data is used to find the optimized coefficients such that the sum of weighted residual errors is minimized over the entire data range. The weights are useful in assigning higher weights to data points that fall in the operating range of the reservoir (between full supply level and dead storage level) and zero weights to outliers. The operating constraints that should be added in the solver in determining this relationship are that the intercept  $C_1$  should always be below the dead storage level (DSL) and the value of  $C_0$  should be 0 unless attempting to fit the DSS equations of negative storage values.

### 3.5.1.2 Channel Representation

In the Vista DSS, river reach arcs are used to model flow travel time and attenuation, which takes place when there is a significant distance between plants or reservoirs in a river. The Muskingum-Cunge channel flow routing method, which is closely related to the Musungkim routing method, is employed here. Musungkim routing method assumes that a storage in a single river reach is related to its inflows and outflows. To give both temporal and spatial resolution, the total reach length of the river reach is broken into a number of subreaches and outflow from each is treated as the inflow into the next. The travel time through each subreach is assumed equal to the Vista computation time step. Number of subreaches is assumed equal to the ratio of the lag between the inflow and outflow hydrograph peaks to DSS Vista time step rounded to the nearest integral number. The routing equation is as follows:

$$Q_t^o = C_1 \times Q_t^i + C_2 \times Q_t^i + C_3 \times Q_{t-1}^o \quad (3.3)$$

where  $Q_t^o$  is outflow during time step  $t$  in  $ft^3/s$  or  $m^3/s$ ,  $Q_t^i$  is inflow during time step  $t$  in  $ft^3/s$  or  $m^3/s$ , and  $C_1, C_2, C_3$  are routing coefficients.

The routing coefficients are determined by fitting the routing equation to the observed field data so that the sum of weighted residual errors is minimized, and the Muskingum coefficients sum to unity.

### 3.5.1.3 Stage-Discharge Relationship

Data for a number of flow gauges can be configured and used in deriving local inflow and for updating inflow forecast models. Channel water levels data are collected from the flow gauges, which must be converted into discharge by a stage-discharge rating curve. The rating curves are modeled using a piecewise approximation, i.e. each polynomial applies to a specific range and the ranges are defined by breakpoints. The equation is as follows:

$$Q = 10^{C_1 \times \log(EL - C_3) + C_2} \quad (3.4)$$

Where  $Q$  is the total river discharge in  $ft^3/s$  or  $m^3/s$ ,  $EL$  is the stage or water level in ft or m and  $C_1, C_2, C_3$  are stage-discharge coefficients.

To estimate stage-discharge coefficients, both stage and corresponding discharge observations for a series of points spanning as many different discharges and stages as

possible are required. The relationship is modeled by fitting Equation 3.4 to observed field data to find the coefficients such that the sum of weighted residual errors is minimized.

#### 3.5.1.4 Spillway Representation

Spillway refers to discharge structures controlling releases from a reservoir to a river or tailwater junction point. In the Vista DSS, spillway discharge is modeled as a function of reservoir elevation and spillway opening. It is modeled by fitting the Vista DSS discharge equations to spillway rating data obtained from field measurements. The Vista DSS has several types of discharge control structures having various discharge equations- spill gates, spill gates-U.S. Army Corps Formulation, overflow weirs, stoplog structures, orifice gates, butterfly valves, uncontrolled canal, uncontrolled tunnel, and flashboards.

Elevation and corresponding discharge observations for a series of spillway openings spanning the maximum possible operating range of the headpond or reservoir up to the dam crest elevation or at a minimum operating range of the reservoir, sill elevations for each structure, width of each structure or bay or area if applicable, maximum number of stop logs and maximum opening, FSL and DSL are required to derive spillway discharge equations. Moreover, operating procedures for each structure are required because of the computational overhead associated with each discharge equation definition in the Vista DSS. Grouping (considering structure operating in the same way as a single structure) is done whenever possible to model the spillway discharge.

Discharge through spill gates (both spill gates and spillway gates-U.S. Army Corps Formulations) are modeled by two equations depending on whether the gate is in or out of the water. If the gate is out of water or slightly submerged (less than 1/5 of the depth above sill), free overflow conditions exist and the weir equations apply; otherwise, the structure functions as an orifice and orifice flow condition exists. The equation for the flow over an overflow structure (weir overflow) is of the form:

$$Q = C_f \times L_e \times (WL - E_{sill})^{E_f} \quad (3.5)$$

Where  $C_f$  is a function of WL and  $E_f$  is a coefficient,  $L_e$  is the effective width,  $WL$  is the water level, and  $E_{sill}$  is the elevation of the sill.

$$C_f = c_f + c_{f1} \times (WL - E_{sill}) + c_{f2} \times (WL - E_{sill})^2 \quad (3.6)$$

Equation 3.5 is used to model free overflow condition of spillway gates, spillway gates - U.S. Army Corps Formulations and flow over weir. Additionally, same set of equations are used for stoplog structures with  $(WL - E_{sill} - \log H)$  replacing  $(WL - E_{sill})$  term where  $\log H$  is the height of the structure on the sill, e.g. stop logs with their own set of coefficients.

For orifice flow conditions of spillway gates when the gate is submerged, the following equation is used

$$Q = C_o \times L_e \times Open \times (WL - E_{sill})^{E_o} \quad (3.7)$$

where  $C_o$  is a function of opening height and  $E_o$  is a coefficient.

$$C_o = c_o + c_{o1} \times Open + c_{o2} \times Open^2 + c_{o3} \times Open^3 \quad (3.8)$$

Equations for describing gated flow condition of spillway gates- U.S. Army Corps (formulations when the gate is submerged) is of the form

$$Q = C_G \left[ \frac{(H_2^{\frac{3}{2}} - H_1^{\frac{3}{2}})}{H_2^{\frac{3}{2}}} \right]^{E_G} \times Q_F \quad (3.9)$$

where  $C_G$  and  $E_G$  are coefficients, H is the head over the spillway crest, i.e.  $H - E_{sill}$ ,  $H_2$  is the  $WL - E_{gateseat}$ ,  $H_1 = H_2 - gate\ opening$  and  $Q_F$  is calculated using Equation 3.5.

The equation for describing the flow through an orifice is of the form:

$$Q = Open \times C \times (WL_{u/s} - WL_{d/s})^E \quad (3.10)$$

where C and E are structure dependent coefficients,  $WL_{u/s}$  and  $WL_{d/s}$  are the upstream and downstream water levels and “Open” is the fraction of the orifice area that is open (0.0 to 1.0). C is determined by a similar equation as Equation 3.8.

The discharge relation for describing the flow through butterfly valves have the same form as Equation 3.10 as with “Open” representing the effective opening (area open). Equations for describing the flow through uncontrolled canal and uncontrolled canal has the same form as Equation 3.10 with their own set of coefficients and “Open” term replaced by  $L_E$  and *Area* respectively. For flashboards, flow is modeled using the weir flow equations when the dam or flashboard sections are overtopped. Flashboard operations are modeled by specifying the date that boards are put into place and the date they are removed or fail and using two sets of coefficients- coefficients for broad crested weirs when flashboards are removed/fail and coefficients for sharp-crested weirs when flashboards are in place to describe the flow-water elevation relations.

Coefficients for the spillway discharge equations are obtained by fitting the Vista DSS elevation discharge equation to the Vista DSS elevation-discharge equation to the spillway rating data obtained from field measurements such that the sum of weighted residual errors is minimized. As usual, higher weights are assigned to the data points that fall in the operating range between FSL and DSL and zero weight is assigned to outliers.

### 3.5.1.5 Hydro Plant Representation (Power Polynomial)

For modeling hydro power plant, power generation from a single generating unit is defined by a power polynomial. The theoretical relationship that the unit power polynomials are based on is

$$p = C \times \eta_p \times Q \times h_n \quad (3.11)$$

where

$C =$  coefficient  $9.812 \times 10^{-3}$  in metric or  $8.460 \times 10^{-3}$  in imperial

$P =$  generated power in MW

$\eta_p =$  overall generating efficient (turbine and generator) (between 0 and 1)

$Q =$  turbine discharge in  $ft^3/s$  or  $m^3/s$

$h_n =$  net head in ft or m

Power polynomial for each unit is a third order equation that represents unit power generations as a function of the head and the discharge along with all the headlosses (entrance, trash rack, conduit friction, bend, contraction, split and exit losses) acting on that unit. DSS distinguishes between plant related headlosses and unit related headlosses to handle situations like when a single common power tunnel or power canal splits to supply water to two or more units so that the total headloss associated with a given unit would be the sum of the plant-related headloss and the unit-related headlosses specific to that unit. The power polynomial is given below:

$$P = a + b \times Q + c \times Q^2 + d \times Q^3 \quad (3.12)$$

where

$P =$  power produced by one unit in MW

$Q =$  discharge flowing through one unit in  $ft^3/s$  or  $m^3/s$

$a, b, c, d =$  functions of unit gross head and are given by following relationships

$$a = a_1 + a_2 \times h + a_3 \times h^2$$

$$b = b_1 + b_2 \times h + b_3 \times h^2$$

$$c = c_1 + c_2 \times h + c_3 \times h^2$$

$$d = d_1 + d_2 \times h + d_3 \times h^2$$

where  $a_n, b_n, c_n, d_n =$  power polynomial coefficients

$h =$  unit gross head defined as the headpond elevation minus the tailwater elevation (plant gross head) minus the plant related losses

$$\text{Plant related headloss} = C_p Q_p^2$$

where  $C_p$  is the plant headloss coefficient and  $Q_p$  is the discharge through the plant and equals the sum of the unit flows.

To derive the unit power polynomial coefficients, sets of corresponding unit discharge, efficiency, and power magnitudes for at least three different net heads, one of which should be the unit's design head are recommended. 'a' term in equation is set to be 0 to

ensure proper behavior of the power polynomial functions over the full range of discharge magnitudes. Estimation of the power polynomial coefficients may be formulated as a multiple linear regression problem with twelve independent variables given by above equations. The solution should satisfy the conditions that the second derivation of efficiency with respect to discharge should be less than 0 and the derivative of power with respect to discharge should be greater than or equal to 0 over a unit's discharge range. Otherwise, the problem may be formulated as a nonlinear optimization problem with the above constraints where the optimization objective is to minimize weighted sum of square residuals. Since the optimization approach requires good starting values and coefficients can be quite small, the multiple regression method is recommended to be tried first.

### 3.5.1.6 Tailwater Representation

Tailwater elevation is used to compute generation plant head and discharge through low-level sluiceways in Vista DSS. To model tailwater elevation, elevation and corresponding discharge observations are needed for a series of points spanning many different discharges and elevations along with the long term average tailwater elevation. It is crucial to identify whether the downstream water level influences the tailwater elevation. When the tailwater elevation is not influenced by the downstream water level, it is a function of total river flow downstream of the plant and is expressed by Equation 3.13. However, when the downstream level influences the tailwater elevation, the tailwater relationship is a function of both discharge and downstream water level and is expressed by Equation 3.14 and 3.15.

$$TWL_0 = a + (b \times Q^c) \quad (3.13)$$

$$TWL_1 = TWL_0 + \max(0, f(WL_{d/s})) \quad (3.14)$$

$$f(WL_{d/s}) = d + e \times WL_{d/s} + (f + g \times WL_{d/s}) \times Ln(Q_0 + Q) \quad (3.15)$$

where TWL is the tail water elevation, Q is the total river discharge,  $WL_{d/s}$  is the downstream water level and  $a, b, c, d, e, f, g, Q_0$  are tailwater elevation coefficients. In the event that the downstream headwater is the tailwater level, equation apply with the coefficients e and  $Q_0$  equal to 1 and all other coefficients equal to 0.

Finally, the tailwater elevation is modeled by fitting the Vista DSS tailwater elevation equations to the observed field data in absence of which a hydraulic model may be used to simulate the required data or the long-term average tailwater can be assumed. The coefficients are found so that the sum of the weighted residual errors is minimized, and the values are close to the theoretical values.

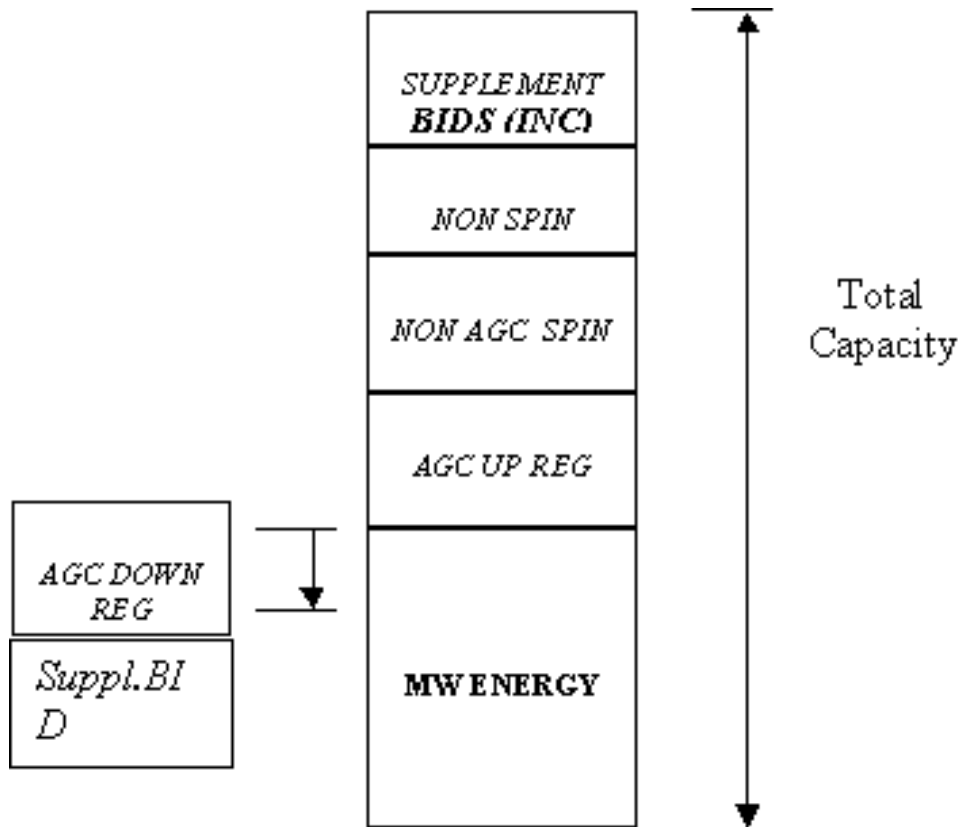
### 3.5.2 Load and Transaction opportunities

Transactions are defined as the economic signal used in the optimization, which are purchases and sales opportunities in the area. Sales are considered as positive and purchases are considered as negative. There are five types of products for transaction-

energy and ancillary services like non-spinning reserve, spinning reserve (non AGC), regulation up and regulation down services as shown in Figure 51. In addition to obtaining payment for energy, generators are paid for the frequency regulation and operating reserves.

Frequency regulation is a tool employed by the power grid operators when the system frequency gets too high or low. Offering frequency regulation to the grid operators means that the generator is willing to increase (regulation up) or decrease outputs (regulation down) by some amount.

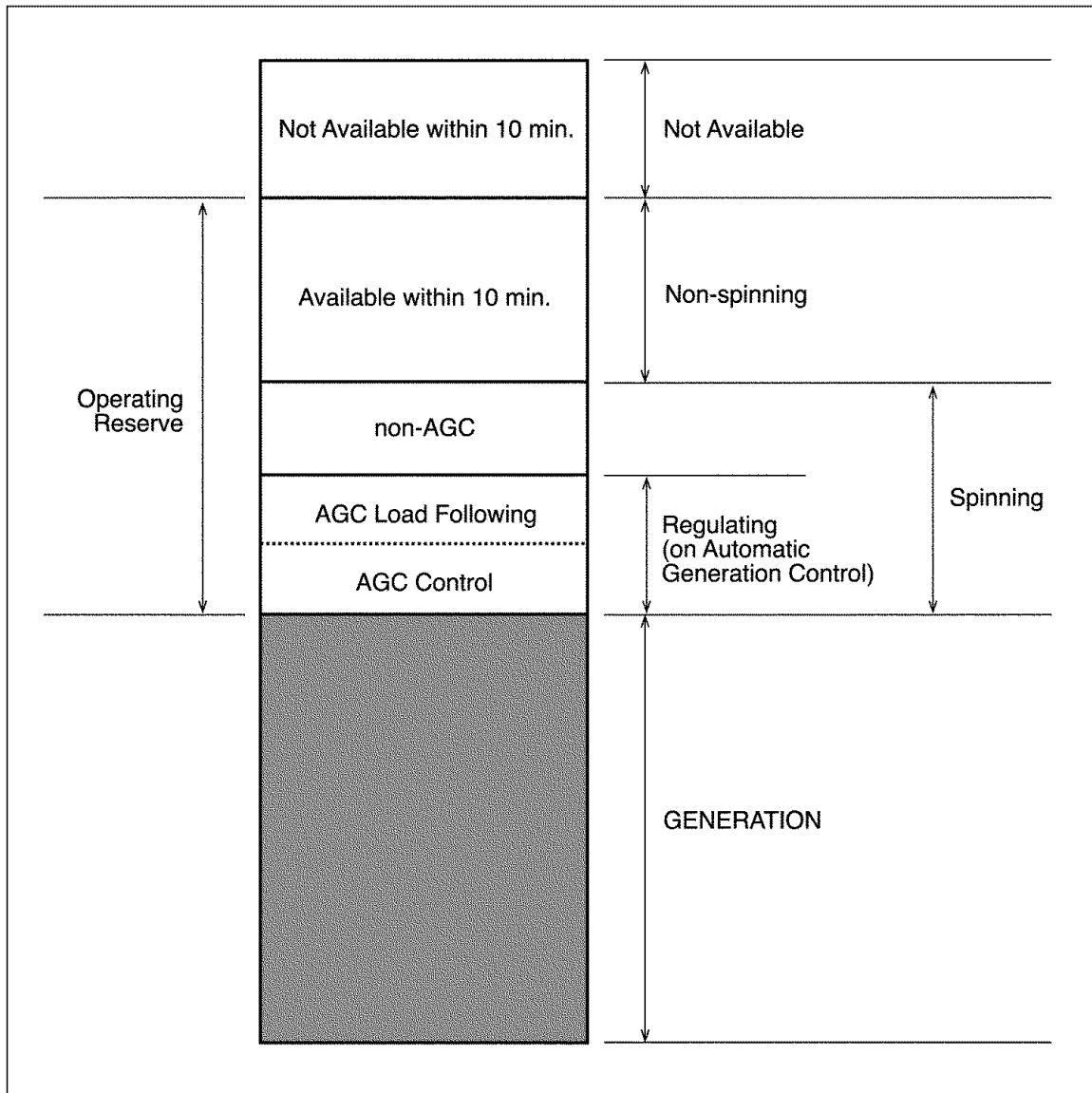
**Figure 51: Products for Transaction in the Electricity Market**



Source: University of California, Riverside

Operating reserves are additional generating requirements from the hydroelectric plants modeled in the system. It is the total of all spinning and non-spinning reserve that is available within 10 minutes. Spinning reserve is the extra generating capacity that are already connected to the power system. Non-spinning reserve is the extra generating capacity that is not currently connected to the system but can be brought online after a short delay. The operating reserve categories are shown in Figure 52.

**Figure 52: Reserve Categories**



Source: University of California, Riverside

### 3.5.3 Constraints

There are three types of constraints in the Vista DSS- physical constraints, operational conditions and operational constraints. Examples of constraints are seasonal reservoir limits, minimum flow requirements, ramping limits of reservoir or downstream of project, fishery elevation or discharge, keeping reservoir as full as possible during boating season etc. It is difficult to translate the constraints into mathematical equations.

### 3.5.3.1 Physical Constraints

Physical constraints represent physical operating limits e.g. limitations of units/tunnels, minimum/maximum turbine limits etc. They are mandatory, and the constraints must always be respected. Physical limits are captured by facility data definition.

### 3.5.3.2 Operational Conditions

Operational conditions represent actual operating model of the system e.g. outages, out of service status of generating or pumping units or spillway structures etc. Operational conditions are optional. They are applied for a user-specific period and must always be met for outages.

### 3.5.3.3 Operational Constraints

Operational constraints for the Vista DSS include reservoir elevation, discharge, scheduled releases, flood rule and time average i.e. flow volume over a specific period. Operating constraints are optional except for minimum and maximum target reservoir levels. To define a constraint, data describing constraint type, start date, end date and constraint cost are required except for the flood rule constraint. Constraint costs are user defined “relaxation cost” for each constraint such that the optimizer is allowed to relax any constraint, but at its “relation cost”. This allows users to prioritize constraints in the event that they have to be violated.

### 3.5.3.4 Reservoir Elevation Constraints

Reservoir elevation constraints are defined on a weekly basis. They include

1. minimum target elevation- minimum reservoir elevation
2. maximum target elevation- maximum reservoir elevation
3. stable- reservoir elevation to be maintained
4. stable or rising- reservoir elevation to be maintained or exceeded
5. ramping- maximum daily reservoir elevation rate of change

The minimum and maximum target elevation constraints define the operational range of the reservoir and are always required in the Vista DSS.

### 3.5.3.5 Discharge Constraints

Discharge constraints are applied to individual arcs, e.g. spill arcs or power arcs or both spill and power arcs. They include

1. minimum- minimum allowable discharge
2. minimum or inflow- lower of either minimum discharge constraint or local inflow
3. maximum- maximum allowable discharge
4. maximum or inflow- higher of either maximum discharge constraint of local inflow
5. ramping- maximum hourly rate of change of discharge

### 3.5.3.6 Scheduled Releases

Scheduled releases describe minimum discharge constraint for short-term releases for specific purposes like recreation or water quality. Scheduled releases are kept separate from other discharge constraints for their large number and high frequency.

### 3.5.3.7 Flood Rule Constraints

During high inflows into the reservoir, flood rule constraints allow for a water level reduction. They are specified in terms of a table of reservoir inflow versus reservoir elevation.

### 3.5.3.8 Time Averaged Constraints

These constraints allow the user to specify a minimum flow volume that must be equaled or exceeded over a specified “n hour” interval. Each constraint is valid between given start and end dates given in the format: MM-DD-YYYY: HHMM

## 3.5.4 Long-term Vista Optimization of Hydropower Generation

To estimate the impact of aerosols on hydropower generation in a hydro year, we use Vista DSS to optimize the generation schedule of the cascaded hydropower system. The goal is to maximize the hydropower system's revenue from providing energy, spinning reserve, frequency regulation up, and frequency regulation down services subject to physical, operational, and contractual constraints. The decision variables include the generation units' status and the amount of generation from each powerhouse. The optimization algorithm assumes that the cascaded hydroelectric system is a price taker in the electricity market. The inputs to the optimization include the inflows to various reservoirs and prices for energy and ancillary services. The hydropower plant operation optimization problem is formulated as follows.

The hydropower plant operation optimization problem is formulated as follows:

$$\text{Max} \sum_{n=1}^N \sum_{t=1}^T \{U_{nt} \times (P_{nt} f_t + c_t^{res} P_{nt}^{res} + c_t^{reg,up} P_{nt}^{reg,up} + c_t^{reg,down} P_{nt}^{reg,down}) - F(U_{nt}, P_{nt}, P_{nt}^{res}, P_{nt}^{reg,up}, P_{nt}^{reg,down})\} \quad (3.16)$$

subject to

$$P_n^{min} \leq P_{nt} \leq P_n^{max}, \quad n = 1, \dots, N, \quad t = 1, \dots, T$$

and other physical and operational constraints

where

$U_{nt}$  = up/down status of generating unit  $n$  at hour  $t$  (0: unit down, 1: unit up)

$P_{nt}$  = power generation of unit  $n$  at hour  $t$

$f_t$  = forecasted energy price for hour  $t$  in \$/MWh

$c_t^{res}$  = forecasted price for spinning reserve service for hour  $t$  in \$/MWh

$P_{nt}^{res}$  = spinning reserve capacity scheduled for unit  $n$  at hour  $t$

$c_t^{reg,up}$  = forecasted price for frequency regulation up service for hour  $t$  in \$/MWh

$p_{nt}^{reg,up}$  = frequency regulation up capacity scheduled for unit  $n$  at hour  $t$

$c_t^{reg,down}$  = forecasted price for frequency regulation down service for hour  $t$  in \$/MWh

$p_{nt}^{reg,down}$  = frequency regulation down capacity scheduled for unit  $n$  at period  $t$

$F$  = operation and maintenance cost of the cascaded hydroelectric system

$p_n^{min}$  = minimum rated capacity of unit  $n$

$p_n^{max}$  = maximum rated capacity of unit  $n$

$N$  = Number of generation units

$T$  = Number of hours in a water year

### 3.6 Method

To calculate the impact of aerosols on hydropower generation, Vista DSS is used to optimize the schedule of generation for one hydro year time horizon to maximize revenue generation while the input for the inflows into the reservoirs are calculated with and without considering the impact of aerosols on reservoir inflows. Inflow forecasts into the Big Creek Hydroelectric system with and without aerosol are computed for water year 2015.

Historic inflows for Lake Thomas A. Edison and Florence Lake are available from water year 2010 to 2014. A dynamic regression model is used to calculate the forecast of inflows in water year 2015. The meteorological data are collected and average over three weather stations of Kaiser Point (KSP), Volcanic Knob (VLC) and Upper Burnt Corral Coral (UBC) located within a  $0.4 \times 0.4^\circ$  grid box with center at ( $37.32^\circ W, -118.97^\circ E$ ). WRF-Chem CTRL and CLEAN simulations of the meteorological variables are available for the water year 2015 at the grid box location. Dynamic regression model is run using the meteorological variables from the WRF-Chem CTRL and CLEAN simulations to forecast inflows into these two reservoirs with and without considering the impact of aerosols.

WRF-Chem CTRL and CLEAN simulations of the meteorological variables at  $0.4 \times 0.4^\circ$  grid boxes with center at the location of Huntington Lake ( $37.14^\circ N, -119.10^\circ W$ ), Shaver Lake ( $37.12^\circ N, -119.29^\circ W$ ), Mammoth pool ( $37.35^\circ N, -119.30^\circ W$ ) and Redinger Lake ( $37.14^\circ N, -119.43^\circ W$ ) are available to calculate inflow into these lakes with and without considering the impact of aerosols. As the historic inflow data for Huntington, Shaver, Redinger and Mammoth lake were not available before water year 2015, it is assumed that the inflow forecasts into these lakes with and without considering the impact of aerosols are the same as the inflows into whichever of the Florence Lake or Lake Edison the said lake is located closest to subjected to the WRF-Chem CTRL and CLEAN simulations corresponding to the grid box with center at the location of the lake scaled by the actual inflows. Moreover, it is assumed that the Bear inflows are about 90 percent

of the Lake Edison inflows as it is correlated to Lake Edison inflows and to some extent, Florence Lake. Further assumptions are listed below:

1. It is assumed that we are coming off a dry year into another dry year. Therefore, there is no recreational requirement for Huntington Lake, hence loosening the constraint.
2. Miniscule side flows into Dam 5, Dam 6 and Pittman are assumed with no difference in the “with aerosol” and “without aerosol” scenario as these inflows are very low in dry years and cannot be stored as they don’t directly reach a big reservoir.

Inflow forecasts into the lakes are fed into the long-term hydro Vista DSS, which produces the optimum generation schedule for a one-year time horizon for the water year 2015 to maximize the value of energy from the hydroelectricity generation while meeting the physical and operational constraints. The optimization is run to maximize profit earned from the value of energy and ancillary services such as. regulation up, regulation down services and spinning reserve. The optimization has a weekly time step. In solving the long-term optimization problem, the problem is formulated as a Mixed Integer Linear programming problem by approximating non-linear relationships as linear relationships.

## **3.7 Result and Analysis**

### **3.7.1 Impact of Aerosols on Big Creek Reservoir Inflows**

The research team quantified the impact of aerosols on reservoir inflow for water year 2015. The team ran a Dynamic regression model using the meteorological variables from WRF-Chem CTRL and CLEAN simulations as input to the testing data set. Therefore, the researchers obtained two inflow forecasts both with and without considering the impact of aerosols for each lake in the Big Creek Hydroelectric System. They calculated the impact of aerosols on reservoir inflow by Equation 3.9. The overall effect of aerosols is a reduction in annual inflow by 1.3 to 10 percent for all of the lakes, as shown in Table 18 and Table 19.

In all of the lakes, aerosols led to lower inflow in all of the seasons due to reduced SWE, precipitation, and snowmelt. Significantly lower annual inflow is observed in Lake Edison and Florence due to impact of aerosols. However, the reduction in inflow is not so significant in the other reservoirs. Similarly, significantly lower inflow in summer is observed in Lake Edison and Florence Lake due to impact of aerosols, which is not seen in the case of other reservoirs. In all of the lakes, the impact of aerosols is small during spring. Lake Edison has a smaller impact in fall and winter, while others had bigger impacts during these seasons. It was assumed that the inflow forecasts of the lakes other than Edison and Florence follow the inflow forecast of Florence Lake subjected to the WRF-Chem simulations of meteorological variables corresponding to their own locations.

**Table 18: Annual Reservoir Inflow under Different Aerosol Conditions**

Lake	Actual	With Aerosol	Without Aerosol
Edison	36044	47662	50332
Florence	74241	85335	92786
Huntington	28485	34755	35803
Mammoth	17492	22272	22572
Redinger	63205	46884	47910
Shaver	83838	80959	82446

Source: University of California, Riverside

**Table 19: Impact of Aerosols (%) on Annual and Seasonal Reservoir Inflow**

Lake	Annual	Fall	Winter	Spring	Summer
Edison	-5	-1	-0.5	1	-15
Florence	-10	-8	-12	-0.5	-23
Huntington	-3	-6	-8	-1	-7
Mammoth	-1	-5	-11	-0.8	-1
Redinger	-2	-6	-10	-1	.0069
Shaver	-2	-8	-5	-1	-1

Source: University of California, Riverside

### 3.7.2 Impact of Aerosols on Hydropower and Revenue Generation

The researchers calculated the impact of aerosols on hydropower generation and revenue in water year 2015 by feeding the inflow forecasts of all of the lakes of the Big Creek Hydroelectric System both with and without considering the impact of aerosols into the Vista DSS. The team ran LT Vista for a one water year time horizon with a goal of optimizing the schedule of generation to maximize the energy value, i.e. the profit earned by the GENCO. The revenue comes from participating in the markets for energy and ancillary services (for example frequency regulation, operative reserves)

The simulation results show that aerosols reduce hydropower generation by 89,356 MWh with an annual loss of revenue of approximately \$2.8 million. The impact of aerosols on hydropower generation and revenue are calculated to be 5.61 percent and 3.88 percent, respectively. These results are shown in Table 20.

**Table 20: Impact of Aerosols on Total Hydropower Generation and Revenue in Water Year 2015**

	CTRL (with aerosol)	CLEAN (without aerosol)	Difference	Percentage Difference (%)
Revenue	\$70,954,360	\$73,818,350	\$2,863,990	3.88
MWH	1,502,330	1,591,686	89,356	5.61

Source: University of California, Riverside

The loss of hydropower generation and subsequent loss of revenue can be explained by the lower annual inflow into the hydropower reservoirs due to impact of aerosols, which results into lower head, thus lowering hydropower generation. Aerosols reduce annual inflow into the reservoirs of the Big Creek Hydroelectric System by 1 to 10 percent. However, in a cascaded hydropower system, influence of inflows into the higher elevation reservoirs on hydropower generation is higher. The reduction in annual inflow into the higher elevation reservoirs Lake Edison and Florence Lake varies from 5 to 10 percent and thus explains the 5.561 percent loss in hydropower generation. The significant loss of revenue earned from hydroelectricity generation due to presence of aerosols can provide justification for stricter environmental regulations to reduce anthropogenic aerosol emissions.

The impact of aerosols on revenue earned from selling energy, spinning reserve, regulation up, and regulation down services are shown in Table 21. It is observed that the impact of aerosols is not significant in case of revenue earned from spinning reserve and regulation up services. However, the reduction in revenue is significant in case of revenue earned from selling energy and regulation down service.

**Table 21: Impact of Aerosols on Hydropower Generation Revenue Based on Revenue Type in Water Year 2015**

Products	CTRL (with aerosol)	CLEAN (without aerosol)	Difference
Energy revenue	\$47,886,920	\$50,292,810	\$2,405,890
Spinning reserve revenue	\$6,717,860	\$6,719,640	\$1780
Regulation up	\$9,774,540	\$9,784,180	\$9640
Regulation down	\$6,575,040	\$7,021,720	\$446,680

Source: University of California, Riverside

### **3.8 Conclusion**

The researchers calculated the impact of aerosols on hydropower generation and revenue by feeding the inflow forecasts of all of the lakes of the Big Creek Hydroelectric System both with and without considering the impact of aerosols into the Vista Decision Support System. The team ran LT Vista for a one water year time horizon with a goal of optimizing the schedule of generation to maximize the profit earned by the GENCO while meeting physical and operational constraints. From the simulations results, the team found that aerosols significantly reduce hydropower generation by 89,356 MWh in water year 2015, which represents a 5.61 percent reduction in the annual hydropower generation. This can be explained by the fact that aerosols reduce inflows into the reservoirs of Big Creek hydroelectric system by 1 to 10 percent and the reduction in inflow in the more influential higher elevation reservoirs is 5 to 10 percent. Thus, a reduction in the plant generation head results in a reduction in power generation. The presence of aerosols causes a staggering \$2.8 million loss in revenue in a water year for Southern California Edison. This significant loss of aerosols provides another justification for stricter environmental regulations to reduce anthropogenic aerosol emissions.

## REFERENCES

- Last Name, First Name. Year. Text, information or both, such as title of book or article, web address. Entity or organization.
- Ackerman, A. S., Kirkpatrick, M. P., Stevens, D. E. & Toon, O. B., 2004. The impact of humidity above stratiform clouds on indirect aerosol climate forcing. *Nature*, Volume 432, pp. 1014-1017.
- Albrecht, B. A., 1989. Aerosols, cloud microphysics, and fractional cloudiness. *Science*, Volume 245, pp. 1227-1231.
- Andreae, M. O., Jones, C. D. & Cox, P. M., 2005. Strong present-day aerosol cooling implies a hot future. *Nature*, Volume 435, p. 1187.
- Barnard, J. C. et al., 2010. Technical Note: Evaluation of the WRF-Chem "Aerosol Chemical to Aerosol Optical Properties" Module using data from the MILAGRO campaign. *Atmos. Chem. Phys.*, 8, Volume 10, pp. 7325-7340.
- Barnett, T. P., Adam, J. C. & Lettenmaier, D. P., 2005. Potential impacts of a warming climate on water availability in snow-dominated regions. *Nature*, Volume 438, pp. 303-309.
- Barnett, T. P., Adam, J. C. & Lettenmaier, D. P., 2005. Potential impacts of a warming climate on water availability in snow-dominated regions. *Nature*, 11, Volume 438, pp. 303-309.
- Baroni, G. & Tarantola, S., 2014. A general probabilistic framework for uncertainty and global sensitivity analysis of deterministic models: a hydrological case study. *Environmental Modelling & Software*, 1, Volume 51, pp. 26-34.
- Box, G. E. P., Jenkins, G. M., Reinsel, G. C. & Ljung, G. M., 2015. *Time Series Analysis: Forecasting and Control*. s.l.:John Wiley & Sons.
- Brandt, R. E., Warren, S. G. & Clarke, A. D., 2011. A controlled snowmaking experiment testing the relation between black carbon content and reduction of snow albedo. *Journal of Geophysical Research: Atmospheres*, Volume 116.
- Brekke, L. D. et al., 2004. Climate Change Impacts Uncertainty for Water Resources in the San Joaquin River Basin, California. *J. Am. Water Resour. Assoc.*, 2, Volume 40, pp. 149-164.
- Cayan, D. R., Riddle, L. G. & Aguado, E., 1993. The influence of precipitation and temperature on seasonal streamflow in California. *Water Resour. Res.*, 4, Volume 29, pp. 1127-1140.
- Chapman, E. G. et al., 2009. Coupling aerosol-cloud-radiative processes in the WRF-Chem model: Investigating the radiative impact of elevated point sources. *Atmos. Chem. Phys.*, 2, Volume 9, pp. 945-964.
- Charlson, R. J. et al., 1991. Perturbation of the northern hemisphere radiative balance by backscattering from anthropogenic sulfate aerosols\*. *Tellus A*, 8, Volume 43, pp. 152-163.

- Charlson, R. J. & Schwartz, S. E., 1992. Climate forcing by anthropogenic aerosols. *Science*, Volume 255, p. 423.
- Charlson, R. J. et al., 1992. Climate Forcing by Anthropogenic Aerosols. *Science*, 1, Volume 255, pp. 423-430.
- Chu-Agor, M. L. et al., 2011. Exploring vulnerability of coastal habitats to sea level rise through global sensitivity and uncertainty analyses. *Environmental Modelling & Software*, 5, Volume 26, pp. 593-604.
- Chylek, P., Ramaswamy, V. & Srivastava, V., 1983. Albedo of soot-contaminated snow. *Journal of Geophysical Research: Oceans*, Volume 88, pp. 10837-10843.
- Ciannelli, L., Chan, K.-S., Bailey, K. M. & Stenseth, N. C., 2004. Nonadditive effects of the environment on the survival of a large marine fish population. *Ecology*, 12, Volume 85, pp. 3418-3427.
- Clarke, A. D. & Noone, K. J., 1985. Soot in the Arctic snowpack: A cause for perturbations in radiative transfer. *Atmospheric Environment (1967)*, Volume 19, pp. 2045-2053.
- Coulibaly, P., Anctil, F. & Bobée, B., 2000. Daily reservoir inflow forecasting using artificial neural networks with stopped training approach. *J. Hydrol.*, 5, Volume 230, pp. 244-257.
- Davidson, J. W., Savic, D. A. & Walters, G. A., 2003. Symbolic and numerical regression: experiments and applications. *Inform. Sci.*, 3, Volume 150, pp. 95-117.
- Dee, D. P. et al., 2011. The ERA-Interim reanalysis: configuration and performance of the data assimilation system. *Q. J. Roy. Meteorol. Soc.*, 4, Volume 137, pp. 553-597.
- Department of Water Resources, C., 2017. *Reservoir inflow at Florence Lake and Lake Thomas A. Edison in California, meteorological variables at weather stations KSP, VLC, UBC, TMR and HTT for water year 2010-14 and WRF-Chem Simulations of meteorological variables for two aerosol scenarios at Big Creek Hydroelectric Project for water year 2013 and 2014*. s.l.:s.n.
- Doherty, S. J. et al., 2010. Light-absorbing impurities in Arctic snow. *Atmospheric Chemistry and Physics*, Volume 10, pp. 11647-11680.
- Emmons, L. K. et al., 2010. Description and evaluation of the Model for Ozone and Related chemical Tracers, version 4 (MOZART-4). *Geosci. Model Dev.*, 1, Volume 3, pp. 43-67.
- Environmental Sciences Division, O. R. N. L., 2013. *Global Fire Emissions Database, Version 2 (GFEDv2.1)*. s.l.:ORNL Distributed Active Archive Center.
- Fan, J. et al., 2014. Aerosol impacts on California winter clouds and precipitation during CalWater 2011: local pollution versus long-range transported dust. *Atmos. Chem. Phys.*, 1, Volume 14, pp. 81-101.
- Fast, J. D. et al., 2014. Modeling regional aerosol and aerosol precursor variability over California and its sensitivity to emissions and long-range transport during the 2010 CalNex and CARES campaigns. *Atmos. Chem. Phys.*, 9, Volume 14, pp. 10013-10060.

- Fast, J. D. et al., 2012. Transport and mixing patterns over Central California during the carbonaceous aerosol and radiative effects study (CARES). *Atmos. Chem. Phys.*, 2, Volume 12, pp. 1759-1783.
- Flanner, M. G., Zender, C. S., Randerson, J. T. & Rasch, P. J., 2007. Present-day climate forcing and response from black carbon in snow. *Journal of Geophysical Research: Atmospheres*, Volume 112.
- Galeati, G., 1990. A comparison of parametric and non-parametric methods for runoff forecasting. *Hydrol. Sci. J.*, 2, Volume 35, pp. 79-94.
- Givati, A. & Rosenfeld, D., 2004. Quantifying Precipitation Suppression Due to Air Pollution. *J. Appl. Meteorol.*, 7, Volume 43, pp. 1038-1056.
- Givati, A. & Rosenfeld, D., 2005. Separation between Cloud-Seeding and Air-Pollution Effects. *J. Appl. Meteorol.*, 9, Volume 44, pp. 1298-1314.
- Givati, A. & Rosenfeld, D., 2007. Possible impacts of anthropogenic aerosols on water resources of the Jordan River and the Sea of Galilee. *Water Resour. Res.*, 10, Volume 43, p. W10419.
- Gleick, P. H. & Chalecki, E. L., 1999. The Impacts of Climatic Changes for Water Resources of the Colorado and Sacramento--San Joaquin River Basins<sup>1</sup>. *J. Am. Water Resour. Assoc.*, 12, Volume 35, pp. 1429-1441.
- Gorman, J. W. & Toman, R. J., 1966. Selection of variables for fitting equations to data. *Technometrics*, Volume 8, pp. 27-51.
- Gragne, A. S., Sharma, A., Mehrotra, R. & Alfredsen, K., 2015. Improving real-time inflow forecasting into hydropower reservoirs through a complementary modelling framework. *Hydrol. Earth Syst. Sci.*, 8, Volume 19, pp. 3695-3714.
- Grell, G. A. et al., 2005. Fully coupled "online" chemistry within the WRF model. *Atmos. Environ.*, 12, Volume 39, pp. 6957-6975.
- Grenfell, T. C., Light, B. & Sturm, M., 2002. Spatial distribution and radiative effects of soot in the snow and sea ice during the SHEBA experiment. *Journal of Geophysical Research: Oceans*, Volume 107.
- Hadley, O. L. & Kirchstetter, T. W., 2012. Black-carbon reduction of snow albedo. *Nature Climate Change*, Volume 2, pp. 437-440.
- Hansen, J. & Nazarenko, L., 2004. Soot climate forcing via snow and ice albedos. *Proceedings of the National Academy of Sciences of the United States of America*, Volume 101, pp. 423-428.
- Hansen, J., Sato, M. & Ruedy, R., 1997. Radiative forcing and climate response. *Journal of Geophysical Research: Atmospheres*, Volume 102, pp. 6831-6864.
- Harper, E. B., Stella, J. C. & Fremier, A. K., 2011. Global sensitivity analysis for complex ecological models: A case study of riparian cottonwood population dynamics. *Ecological Applications: A Publication of the Ecological Society of America*, 6, Volume 21, pp. 1225-1240.

- Haywood, J. & Boucher, O., 2000. Estimates of the direct and indirect radiative forcing due to tropospheric aerosols: A review. *Reviews of geophysics*, Volume 38, pp. 513-543.
- Jacobson, M. Z., 2001. Strong radiative heating due to the mixing state of black carbon in atmospheric aerosols. *Nature*, Volume 409, pp. 695-697.
- Jacobson, M. Z., 2004. Climate response of fossil fuel and biofuel soot, accounting for soot's feedback to snow and sea ice albedo and emissivity. *Journal of Geophysical Research: Atmospheres*, Volume 109.
- Jain, S. K., Das, A. & Srivastava, D. K., 1999. Application of ANN for reservoir inflow prediction and operation. *J. Water Resour. Plann. Man.*, Volume 125, pp. 263-271.
- Johnson, B. T., Shine, K. P. & Forster, P. M., 2004. The semi-direct aerosol effect: Impact of absorbing aerosols on marine stratocumulus. *Quarterly Journal of the Royal Meteorological Society*, Volume 130, pp. 1407-1422.
- Jones, A., Roberts, D. L. & Slingo, A., 1994. A climate model study of indirect radiative forcing. *Nature*, Volume 370, pp. 450-453.
- Kaufman, Y. J. et al., 2005. The effect of smoke, dust, and pollution aerosol on shallow cloud development over the Atlantic Ocean. *Proceedings of the National Academy of Sciences of the United States of America*, Volume 102, pp. 11207-11212.
- Kaufman, Y. J., Tanre, D. & Boucher, O., 2002. A satellite view of aerosols in the climate system. *Nature*, Volume 419, pp. 215-223.
- Kiehl, J. T. & Briegleb, B. P., 1993. The relative roles of sulfate aerosols and greenhouse gases in climate forcing. *Science*, Volume 260, pp. 311-314.
- Kilinc, I. & Cigizoglu, K., 2003. Reservoir management using artificial neural networks. *Proc. 14th. Reg. Director. DSI (State Hydraulic Works)*.
- Knowles, N. & Cayan, D. R., 2002. Potential effects of global warming on the Sacramento/San Joaquin watershed and the San Francisco estuary. *Geophys. Res. Lett.*, 9, Volume 29, p. 1891.
- Lall, U. & Bosworth, K., 1994. Multivariate Kernel Estimation of Functions of Space and Time Hydrologic Data. In: K. W. Hipel, A. I. McLeod, U. S. Panu & V. P. Singh, eds. *Stochastic and Statistical Methods in Hydrology and Environmental Engineering*. s.l.:Springer Netherlands, pp. 301-315.
- Lau, W. K. M., Kim, M.-K., Kim, K.-M. & Lee, W.-S., 2010. Enhanced surface warming and accelerated snow melt in the Himalayas and Tibetan Plateau induced by absorbing aerosols. *Environmental Research Letters*, Volume 5, p. 025204.
- Lee-Taylor, J. & Madronich, S., 2002. Calculation of actinic fluxes with a coupled atmosphere-snow radiative transfer model. *Journal of Geophysical Research: Atmospheres*, Volume 107.
- Lettenmaier, D. P. & Gan, T. Y., 1990. Hydrologic sensitivities of the Sacramento-San Joaquin River Basin, California, to global warming. *Water Resour. Res.*, 1, Volume 26, pp. 69-86.

- Lohmann, U., 2005. Impact of Aerosols on the Hydrological Cycle. *Water and the Environment*, Volume 12, p. 104.
- Madsen, H., Richaud, B. & Pedersen, C. B., 2009. A real-time inflow forecasting and reservoir optimization system for optimizing hydropower production. *Waterpower XVI*.
- Makler-Pick, V. et al., 2011. Sensitivity analysis for complex ecological models - A new approach. *Environmental Modelling & Software*, 2, Volume 26, pp. 124-134.
- Makridakis, S., Wheelwright, S. C. & Hyndman, R. J., 2008. *Forecasting methods and applications*. s.l.:John Wiley & Sons.
- Marks, A. A. & King, M. D., 2013. The effects of additional black carbon on the albedo of Arctic sea ice: variation with sea ice type and snow cover. *The Cryosphere*, Volume 7, p. 1193.
- Marks, A. A. & King, M. D., 2014. The effect of snow/sea ice type on the response of albedo and light penetration depth (e-folding depth) to increasing black carbon. *The Cryosphere*, Volume 8, p. 1625.
- Ming, J. et al., 2009. Black Carbon (BC) in the snow of glaciers in west China and its potential effects on albedos. *Atmospheric Research*, Volume 92, pp. 114-123.
- Moeni, H., Bonakdari, H., Fatemi, S. E. & Zaji, A. H., 2017. Assessment of Stochastic Models and a Hybrid Artificial Neural Network-Genetic Algorithm Method in Forecasting Monthly Reservoir Inflow. *INAE Lett.*, 4, Volume 2, pp. 13-23.
- Mohammadi, K., Eslami, H. R. & Dardashti, S. D., 2005. Comparison of Regression, ARIMA and ANN Models for reservoir Inflow Forecasting using Snowmelt Equivalent (A Case Study of Karaj). *J. Agric. Sci. Technol*, 1, Volume 7, pp. 17-30.
- Pankratz, A., 2012. *Forecasting with Dynamic Regression Models*. s.l.:John Wiley & Sons.
- Papamichail, D. M. & Georgiou, P. E., 2001. Seasonal ARIMA Inflow Models for Reservoir Sizing. *J. Am. Water Resour. Assoc.*, 8, Volume 37, pp. 877-885.
- Penner, J. E. et al., 2006. Model intercomparison of indirect aerosol effects. *Atmospheric Chemistry and Physics*, Volume 6, pp. 3391-3405.
- Pianosi, F. et al., 2016. Sensitivity analysis of environmental models: A systematic review with practical workflow. *Environmental Modelling & Software*, 5, Volume 79, pp. 214-232.
- Qian, Y., Gustafson, W. I., Leung, L. R. & Ghan, S. J., 2009. Effects of soot-induced snow albedo change on snowpack and hydrological cycle in western United States based on Weather Research and Forecasting chemistry and regional climate simulations. *J. Geophys. Res.-Atmos.*, 2, Volume 114, p. D03108.
- Qian, Y., Gustafson, W. I., Leung, L. R. & Ghan, S. J., 2009. Effects of soot-induced snow albedo change on snowpack and hydrological cycle in western United States based on Weather Research and Forecasting chemistry and regional climate simulations. *Journal of Geophysical Research: Atmospheres*, Volume 114.

- Quaas, J., Boucher, O., Bellouin, N. & Kinne, S., 2008. Satellite-based estimate of the direct and indirect aerosol climate forcing. *Journal of Geophysical Research: Atmospheres*, Volume 113.
- Ramanathan, V. et al., 2001. Indian Ocean Experiment: An integrated analysis of the climate forcing and effects of the great Indo-Asian haze. *J. Geophys. Res.-Atmos.*, 11, Volume 106, pp. 28371-28398.
- Reay, H. J., France, J. L. & King, M. D., 2012. Decreased albedo, e-folding depth and photolytic OH radical and NO<sub>2</sub> production with increasing black carbon content in Arctic snow. *Journal of Geophysical Research: Atmospheres*, Volume 117.
- Rosenfeld, D., 2000. Suppression of rain and snow by urban and industrial air pollution. *Science*, Volume 287, pp. 1793-1796.
- Rosolem, R. et al., 2012. A fully multiple-criteria implementation of the Sobol method for parameter sensitivity analysis. *Journal of Geophysical Research: Atmospheres*, 4, Volume 117, p. D07103.
- Saltelli, A. et al., 2010. Variance based sensitivity analysis of model output. Design and estimator for the total sensitivity index. *Computer Physics Communications*, 2, Volume 181, pp. 259-270.
- Saltelli, A., Annoni, P. & D'Hombres, B., 2010. How to avoid a perfunctory sensitivity analysis. *Procedia - Social and Behavioral Sciences*, 1, Volume 2, pp. 7592-7594.
- Saltelli, A., Tarantola, S. & Chan, K. P.-S., 1999. A quantitative model-independent method for global sensitivity analysis of model output. *Technometrics*, 2, Volume 41, pp. 39-56.
- Schwartz, S. E., 1996. The whitehouse effect- Shortwave radiative forcing of climate by anthropogenic aerosols: an overview. *J. Aerosol Sci.*, 4, Volume 27, pp. 359-382.
- Serreze, M. C. et al., 1999. Characteristics of the western United States snowpack from snowpack telemetry(SNOTEL) data. *Water Resour. Res.*, Volume 35, pp. 2145-2160.
- Shaw, W. J. et al., 2008. An evaluation of the wind erosion module in DUSTRAN. *Atmos. Environ.*, 3, Volume 42, pp. 1907-1921.
- Stewart, I. T., Cayan, D. R. & Dettinger, M. D., 2004. Changes in Snowmelt Runoff Timing in western North America under a 'Business as Usual' Climate Change Scenario. *Clim. Change*, 1, Volume 62, pp. 217-232.
- Tomassini, L. et al., 2007. Robust bayesian uncertainty analysis of climate system properties using markov chain monte carlo methods. *Journal of Climate*, 4, Volume 20, pp. 1239-1254.
- Twomey, S., 1974. Pollution and the planetary albedo. *Atmospheric Environment (1967)*, Volume 8, pp. 1251-1256.
- Twomey, S., 1991. Aerosols, clouds and radiation. *Atmospheric Environment. Part A. General Topics*, Volume 25, pp. 2435-2442.

- Uusitalo, L., Lehtikainen, A., Helle, I. & Myrberg, K., 2015. An overview of methods to evaluate uncertainty of deterministic models in decision support. *Environmental Modelling & Software*, 1, Volume 63, pp. 24-31.
- Valipour, M., 2015. Long-term runoff study using SARIMA and ARIMA models in the United States. *Meteorol. Appl.*, Volume 22, pp. 592-598.
- Valipour, M., Banihabib, M. E. & Behbahani, S. M. R., 2013. Comparison of the ARMA, ARIMA, and the autoregressive artificial neural network models in forecasting the monthly inflow of Dez dam reservoir. *J. Hydrol.*, 1, Volume 476, pp. 433-441.
- VanRheenen, N. T., Wood, A. W., Palmer, R. N. & Lettenmaier, D. P., 2004. Potential Implications of PCM Climate Change Scenarios for Sacramento--San Joaquin River Basin Hydrology and Water Resources. *Clim. Change*, 1, Volume 62, pp. 257-281.
- Warren, S. G., 1984. Impurities in snow: Effects on albedo and snowmelt. *Annals of Glaciology*, Volume 5, pp. 177-179.
- Warren, S. G. & Clarke, A. D., 1990. Soot in the atmosphere and snow surface of Antarctica. *J. Geophys. Res.*, Volume 95, pp. 1-1816.
- Wiscombe, W. J. & Warren, S. G., 1980. A model for the spectral albedo of snow. I: Pure snow. *Journal of the Atmospheric Sciences*, Volume 37, pp. 2712-2733.
- Wu, L. et al., 2017b. Impacts of aerosols on seasonal precipitation and snowpack in California based on convective-resolving WRF-Chem simulations.. *Atmos. Chem. Phys.*, Volume 2017, pp. 1-54.
- Wu, L., Su, H. & Jiang, J. H., 2011. Regional simulations of deep convection and biomass burning over South America: 1. Model evaluations using multiple satellite data sets. *J. Geophys. Res.-Atmos.*, 9, Volume 116, p. D17208.
- Wu, L., Su, H. & Jiang, J. H., 2011. Regional simulations of deep convection and biomass burning over South America: 2. Biomass burning aerosol effects on clouds and precipitation. *J. Geophys. Res.-Atmos.*, 9, Volume 116, p. D17209.
- Wu, L., Su, H. & Jiang, J. H., 2013. Regional simulation of aerosol impacts on precipitation during the East Asian summer monsoon. *J. Geophys. Res.-Atmos.*, 6, Volume 118, pp. 6454-6467.
- Wu, L. et al., 2017a. WRF-Chem simulation of aerosol seasonal variability in the San Joaquin Valley. *Atmos. Chem. Phys. Discuss.*, 11, Volume 17, pp. 7291-7309.
- Xu, B. et al., 2009. Black soot and the survival of Tibetan glaciers. *Proceedings of the National Academy of Sciences*, Volume 106, pp. 22114-22118.
- Xu, Z. X. & Li, J. Y., 2002. Short-term inflow forecasting using an artificial neural network model. *Hydrol. Process.*, 8, Volume 16, pp. 2423-2439.
- Ye, H. et al., 2012. Black carbon in seasonal snow across northern Xinjiang in northwestern China. *Environmental Research Letters*, Volume 7, p. 044002.
- Zhao, C. et al., 2013. Uncertainty in modeling dust mass balance and radiative forcing from size parameterization. *Atmos. Chem. Phys.*, 11, Volume 13, pp. 10733-10753.

Zhao, C. et al., 2014. Simulating black carbon and dust and their radiative forcing in seasonal snow: a case study over North China with field campaign measurements. *Atmos. Chem. Phys.*, 10, Volume 14, pp. 11475-11491.

Zhao, C. et al., 2010. The spatial distribution of mineral dust and its shortwave radiative forcing over North Africa: modeling sensitivities to dust emissions and aerosol size treatments. *Atmos. Chem. Phys.*, 9, Volume 10, pp. 8821-8838.